Analysis And Development Of An Innovative E-bike System

by

Tarun Bajaj

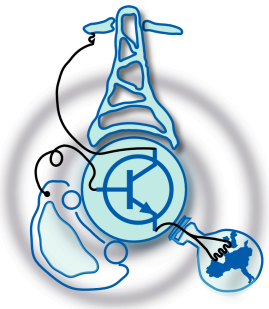

Submitted to the Department of Electrical Engineering, Electronics, Computers and Systems
in partial fulfillment of the requirements for the degree of
Erasmus Mundus Master Course in Sustainable Transportation and Electrical Power Systems
at the
UNIVERSIDAD DE OVIEDO
Aug 2019

Author .....

Certified by .....
Dr. Pablo García Fernández
Associate Professor
Thesis Supervisor

Certified by .....
Andrea Valenza
R&D Manager, F.I.V. E Bianchi S.p.A.
Thesis Supervisor

Analysis And Development Of An Innovative E-bike System

by

Tarun Bajaj

Submitted to the Department of Electrical Engineering, Electronics, Computers and Systems
on Aug 31, 2019, in partial fulfillment of the
requirements for the degree of
Erasmus Mundus Master Course in Sustainable Transportation and Electrical Power Systems

Abstract

E-bikes constitute a sizeable market share and this is only expected to increase. e-MTBs constitute a major share of e-bikes. But, as their numbers continue to increase, it is important to keep in mind their safety. Using the inherent advantages of electric motors, we assess the their use not just in providing additional performance but aiding in safety.

Benchmarking of e-bike drive-trains is carried out to understand the existing options available on the market. Performance analysis of two hub motors, internally geared and direct drive hub motors are carried out. Various factors such as efficiency, cost, weight and size are considered to choose the best fit. The various functionalities are tested on a prototype along with interface of additional peripherals and sensors.

Due to the benefits of fast dynamics of electrical machines and use of dual hub motors, feasibility of a traction control and ABS system is performed to enhance safety of the rider. These aims are simulated in MATLAB/ Simulink and partly implemented to verify their performance.

Thesis Supervisor: Dr. Pablo García Fernández
Title: Associate Professor

Thesis Supervisor: Andrea Valenza
Title: R&D Manager, F.I.V. E Bianchi S.p.A.

Acknowledgments

I would like to thank the consortium of EMJMD STEPS for giving me the opportunity of this master's course in such a diverse environment. Mr Andrea Valenza for believing in me to work independently on the project and providing will the needed resources in a timely manner. Riccardo Giuliani and Fabio Ferri in helping with solutions to numerous issues and giving me insights into the bicycle industry. Alessandro Antoniali, who helped me in the selection and procurement of numerous components and was always welcoming to solve doubts. The various members in the factory, including Guido Gatti and Mattia for their invaluable support in the putting the bike together on time. I am pleased to have meet Daniele Cantu who helped me during my time of need and in better understanding of the history of Italy. I am thankful to the entire organization of F.I.V. E Bianchi S.p.A for being welcoming.

I would like my extend my gratitude to Susana Menendez and Dr. Pablo Arboleya for their assistance throughout the duration of my thesis and the course. The faculty of the master's program and prior who have imparted me with the knowledge and skills to carry out my work on the topic. Dr. Pablo Garcia who guided on technicalities of the concept and for being the inspiration to pursue the topic.

I would like to extend my regards to everyone who have supported me and contributed in their way.

Contents

List of Figures

List of Tables

Chapter 1

Introduction

Our transportation system has gradually evolved from using horse-carts to internally combustion engines vehicles to the future of electrified transportation. With the widespread use of cars, better road infrastructure had to be developed. The internal combustion engine greatly accelerated the acceptance of road transportation and a number of special purpose vehicles like trucks and later buses for public transportation were introduced. As technology improved, new modes like airplanes become available for masses. Today we are at a similar position but with electrified transport which has the potential to be a universal source of power for transportation. This change like before would result in a number of changes to our preferences. Thus, various governments are working towards a suitable policy framework. One such is conducted by the EU as the 'Clean, Urban transport' program. It selects and works towards the important problems to be addressed. Table 1 in [8] shown the topics of importance. Unsurprisingly, emissions is the most important, resulting in the commission choosing to work towards promoting alternative modes of transportation in table 2 from [8] for general and commercial purposes.

Bicycles are a fundamental means of transportation. Present day bikes have principally remained the same for a century since Bianchi introduced the first bicycle with same sized wheels and pneumatic tyres indicating the inherent advantages of such a design. However, with the improvements in battery technologies and focus on sustainability, e-bikes constitute an important part of the market [9]. They have

gradually gained more market acceptance because of the advantages of electric motors as they provide flexibility to be used in various types of bike styles like road, cargo and MTBs. However, MTBs constitute a major part of the e-bike market due to the performance offered by the motor [9].

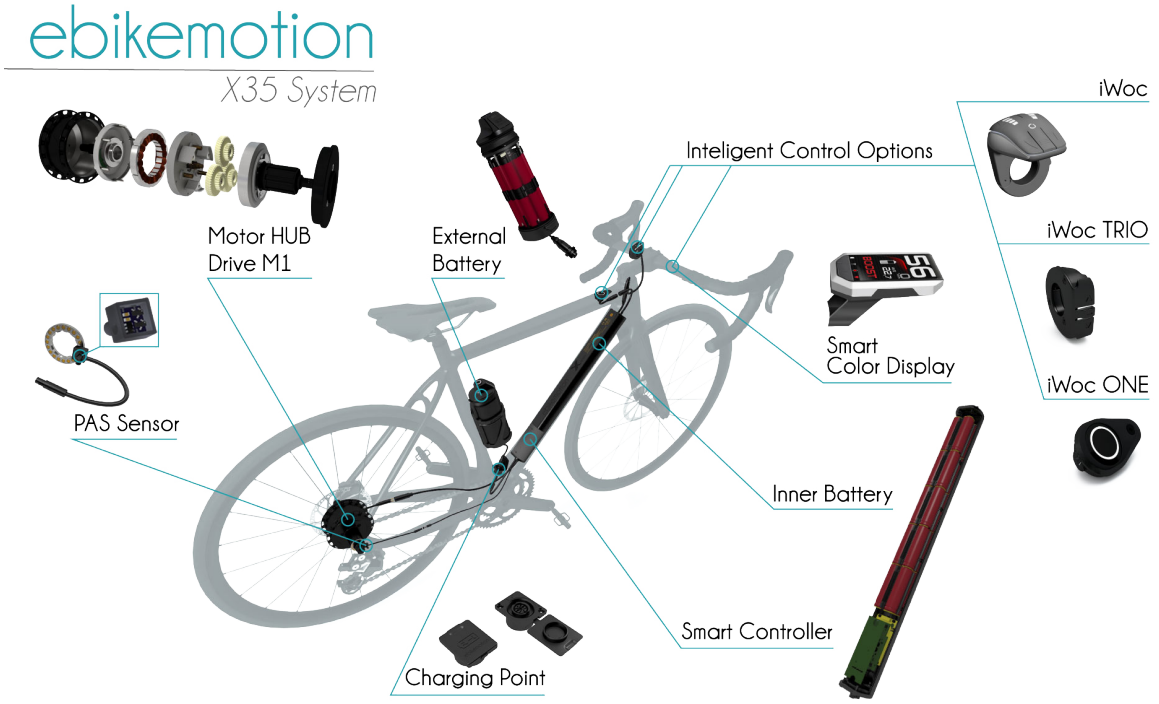

Figure 1-1: Components of an e-bike with hub motor, courtesy- e-bike motion

More than 60% of our urban journeys are less than 10 Km and with people becoming more serious on environmental issues, we see gradual rise in usage of more sustainable transportation modes like bikes to an extent where 25% of urban distance in Netherlands is covered on e-bikes[10]. Numerous studies [10], [11] have shown the tangible advantages bikes provide. The health benefits of cycling are well accepted but the contribution of e-bikes on the environmental and financial impacts are significant. [10] states that in the condition that a high shift scenario (bicycle usage in cities throughout the world becomes same as the current usage in high cycling regions like Denmark, Netherlands), the emissions due to transport can reduce by 50% in the year 2050. It will also result in a saving of USD$1 trillion. Thus, we see various governments working on encouraging more people to take up cycling. Cities like New York, London, Oslo, Copenhagen and many others have planned to ban

motor vehicles completely leaving space for pedestrians and cyclists.

Typical components of an e-bike are shown in Figure 1-1, Figure 1-2. The three major components are the motor, batteries and an HMI unit, but a number of additional sensors like the cadence, wheel speed sensor are used to control the amount of assist. These components are detailed in Chapter 2.

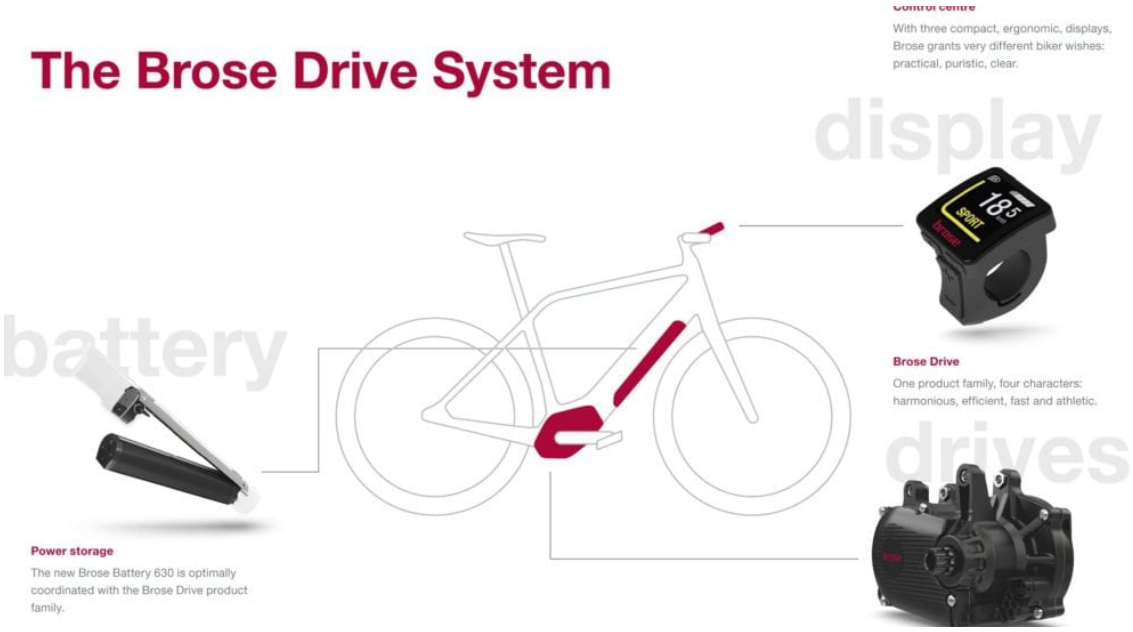

Figure 1-2: Components of an e-bike with mid-drive motor, courtesy- Brose

1.1 Motivation

As e-bikes share space with pedestrians, it is necessary for them to adhere to certain rules that ensure safety of people around them governed by [12] in the Europe. The pedelec class (assist upto 25 kmph) form the majority of e-bikes sold as they can be used without any restrictions like a regular bike. The class of bike in consideration in an s-pedlec (speed pedelec) (L1e-B class of vehicles) that is capable of assist upto 45 kmph. These bikes have the capability of substituting upto 90% of the urban journeys. This class of e-bikes are not standard across Europe and each country can frame rules by themselves. Though EU limits the power to 4000 W, we limit the e-bike to 500W of power to keep it within relevant categories in a number of countries

such as the UK.

With these greater numbers and diversification of used cases, safety of cyclist has already taken a hit [13]. Thus, is vital to consider safety of riders while designing future e-bike systems. A bike's inherent design can provide only partial protection to riders in case of fatal events. Personal protection like helmets are helpful but can also motivate cyclists to be reckless. Prevention of such fatalities are the best way to increase safety. Modern motor control techniques can enable very fast dynamic response of these motors which can be 5-10 higher than those of mechanical systems. This opens up new avenues in the fields of safety as the system can be made to react much faster than the rider which can help in preventing accidents.

1.2 Research Objectives

S-pedelecs differ from pedelecs only in their maximum assistance speed upto 45 Kmph compared to 25 kmph of pedelecs. If the bike employs hub motors, they should be capable to spin at higher speeds. However, S-pedelecs typically employ mid-drive motors which can use the same motors as pedelecs and use the gears of the bike for operating at higher speeds. Studies have shown that safety risk increases with increase in bike speed [14]. Figure 1-3 from [1] shows alarming increase in risks as speeds increase over 25 Kmph. However, S-pedelecs on the market currently do not offer any substantial safety features over pedelecs.

The aim of the work is to decide the optimal electrical sub-system components and architecture for an S-pedelec e-bike system. The specific requirements are -

- Dual hub motors are best traction under all road conditions.
- Regenerative braking capability to hold speed during downhill.
- Evaluation of TC and ABS system for enhanced safety.
- Good bike dynamics for recreational purpose.

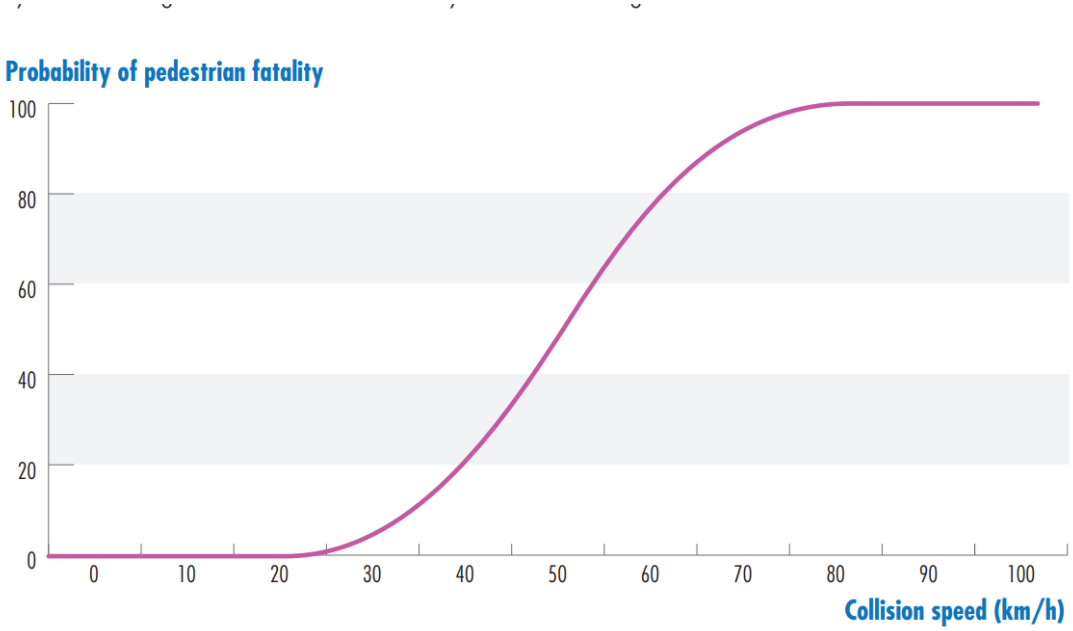

Figure 1-3: Probabilistic relationship between bike speed and fatality from [1]

Modern e-bikes have a huge number of components that are required for performance, safety and connectivity. A great deal of efforts has been put into the connectivity solutions of e-bikes as majority of demographics own smart-phones that provide a good platform to inform the rider. These include technologies like Bluetooth, Wi-Fi, GPS, etc. However, discussion of these will be omitted in the thesis and emphasis on the relevant systems will be explored.

1.3 Thesis Organization

Chapter 1 of the thesis gives us the motivation behind the project and sets certain aim to be achieved. Chapter 2 compares and explores the various technologies at our disposal to get an understanding of their differences. Different cell chemistry are studied, the different types of motors and their control employed is discussed. Various existing products used by Bianchi in their current range are dis-assembled and studied. The general overview of the system is presented. Chapter 3 introduces the modeling of a bike and the parameters that effect the dynamic performance. Both Longitudinal and lateral dynamics are studied resulting in equations that form

the basis of modeling and control in subsequent Chapters. Chapter 4 details about the simulations performed in SIMULINK to assess the performance of motor control algorithm. Safety systems using ABS and Traction control are tested under different conditions. Effect of variations in their parameters are assessed. Chapter 6 briefly describes the implementation steps involved and the other auxiliary components. The steps are sequenced as it were in practice, starting for motor control to tests performed on the prototype. Some details of the prototype and the results obtained under various tests are presented.

Chapter 2

Current Technology And Design Considerations

We examine the various architecture and options existing on the market for e-bikes. A brief account of them will be presented along and references for more details will be linked where applicable.

2.1 E-bike Architecture

As the e-bike market has evolved to cater to different needs, a number of variations in the distribution of electrical systems are available in the market with their own traits.

2.1.1 Mid-drive

Mid drive systems have the motors replacing the traditional bottom bracket of a bike as shown in Figure 2-1. The chain is connected to both the motor shaft and the crank. As a result, the torque from the motors, like from the rider can be multiplied using the gears depending on the terrain and speed. Since the motors can spin at a fixed ratio relative to the crank, they can be sized according to rider cadence and used for bikes of different speed. Mid-drives are the best performing type as they use

the already available transmission system However, due to the chain drive they loose their dynamics performance. Mid-drives have lower unsprung mass which helps in better suspension dynamics for a full suspended MTB.

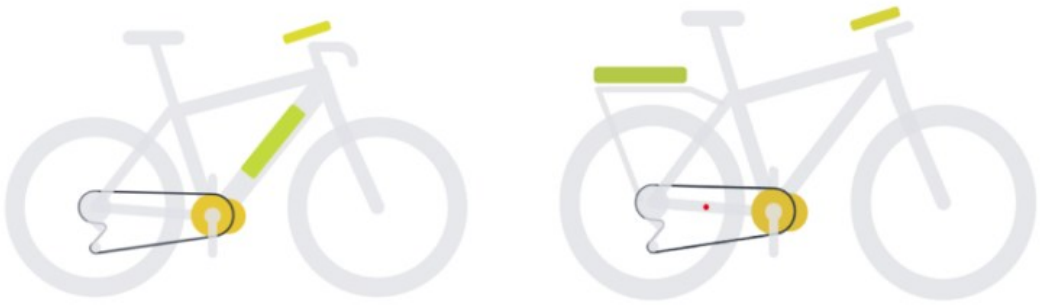

Figure 2-1: Mid-drive motor configurations, courtesy-Bafang

2.1.2 Front-drive

Front drive systems have the motors attached to the front wheels shown in Figure 2-2. They are by far the simplest system to install which require virtually no modification and are preferred by hobbits. The are relatively low powered and light weight and typically used for urban commuting.

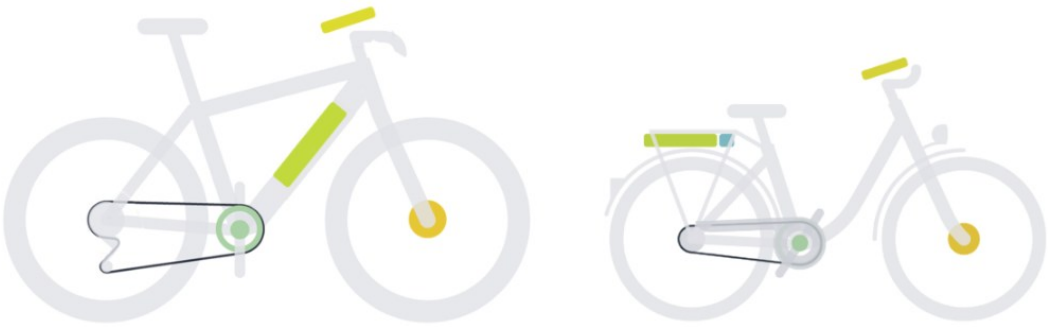

Figure 2-2: Front-drive motor configurations, courtesy-Bafang

2.1.3 Rear-drive

Rear drive systems have the motors attached to the rear wheels shown in Figure 2-3. They are a good compromise between the front-drive and mid-drive variants. As the majority of the weight of the bike is on the rear, they can provide greater acceleration with relatively low modifications to the frame. Both front and rear motors form a small fraction of MTBs.

Figure 2-3: Rear-drive motor configurations, courtesy-Bafang

2.2 Electrical sub-systems

The electrical system forms the basis of an e-bike. The major electrical sub-systems of an e-bike are detailed below.

2.2.1 Battery

The battery provides the electrical power required for the assist. Although, there are a number of batteries available namely lead acid, Ni-MH; Li-ion battery are the standard and used in all e-bikes due to their superior energy density and depreciating costs. The Table 2.1 provides a list of the commonly used Li-ion types.

These chemistries are available in both cylindrical and prismatic cells. Cylindrical cells are commonly employed as they have higher stability abit with higher costs. A variant of Li-ion cells is the Lithium polymer cells. They have a polymer membrane instead of a separator. This sightly reduces the specific energy and increases power

Table 2.1: Li-ion chemistry

Properties	**LMO**	**NMC**	**LFP**
Nominal capacity (Ah)	20	24	25
Discharge out of voltage (V)	2.7	2.7	2.5
Charge out of voltage (V)	4.2	4.2	3.8
Max discharge current rate (C)	2	2	3
Energy density (Wh/Kg)	150-200	150-220	90-120
Cycle life(1C)	2,000	2,000	3,000

density. They are used in a number of EVs. However, due to the relative relaxed performance requirements, they have not found their use in e-bikes. Out of the chemsitries listed above, the LMO (Lithium Manganese Oxide) and NMC (Lithium Nickel Manganese Cobalt) have similar performance however, NMC is the most widely used as it has higher specific energy and greater stability over longer operating life. LFP (Lithium Ferrous Phosphate) stands out as it sacrifices specific energy for higher C rates. There are regulation that are required to be met for safety of batteries [15] but does not limit the capacity. The regulations do not restrict the amount of power that can be used to recharge to battery. This is limited by the max C-rate of the pack.

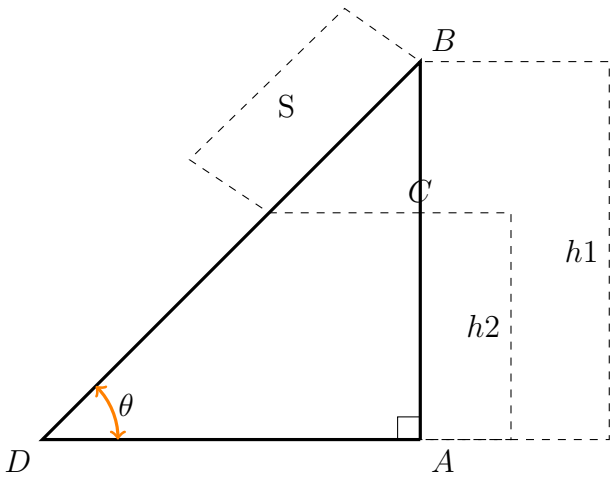

Figure 2-4: Downhill representation

Downhill holding speed

An important consideration for battery cell selection and sizing is consideration

of regen braking to limit the speed of the bike during descents. The regen power determines the holding speed and gradient during descents.

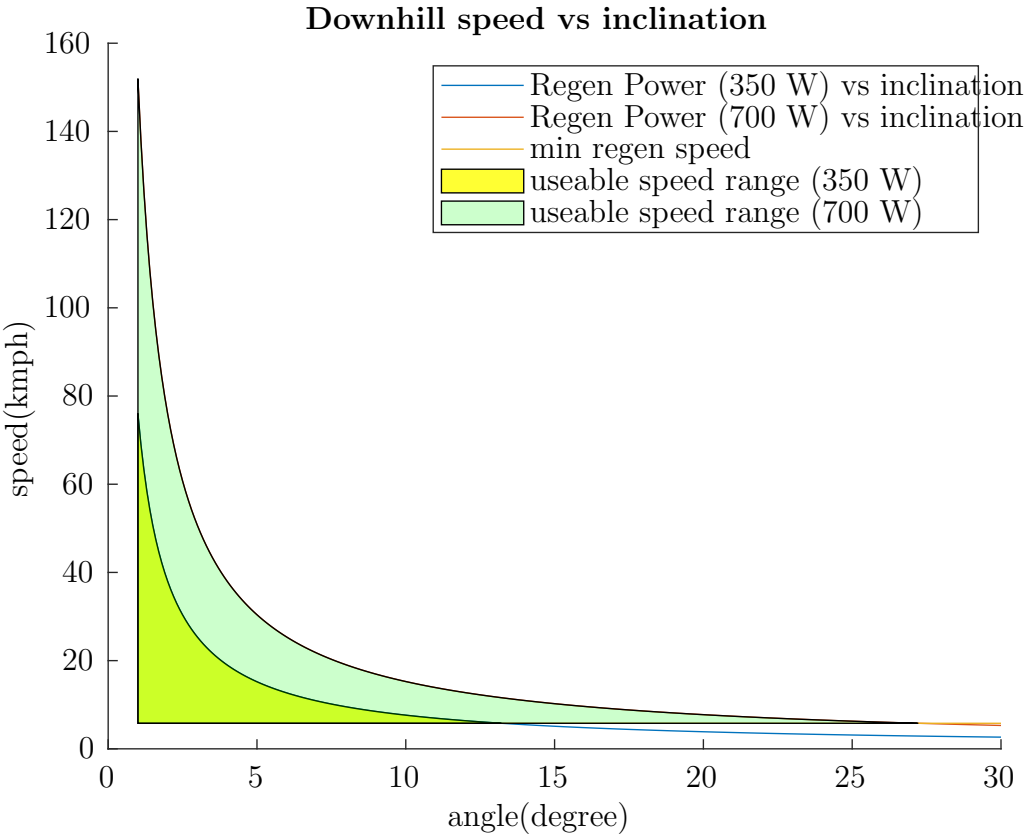

Figure 2-5: Regen Power vs decent angle

The speed can be held constant if the kinetic energy is constant and the difference in potential energy along the direction of travel is used to charge the battery. Consider the bike starting at a height of h1 and descending to h2 in time t by covering a distance S, where θ is the inclination angle as shown in Figure 2-4. The relationship between the regen power (P) and velocity (v) is given by (2.1).

$$P = \frac{W}{t} = \frac{m \cdot g \cdot (h1 - h2)}{t} = \frac{m \cdot g \cdot S \cdot sin(\theta)}{t} = m \cdot g \cdot v \cdot sin(\theta) \tag{2.1}$$

The comparison of battery packs with different C-rate of 0.5 and 1 C is considered. For a typical battery pack of 700 Whr, the differences in the max holding speed vs

inclination is shown in Figure 2-5. We see that higher re-gen power enables us to hold higher speeds for the same descent angle.

A matter of concern is the effect of regen on the longevity of the battery pack. The degradation mechanism in Li-ion batteries is triggered by cell temperature. High charge and discharge rates demands higher currents producing heat that reduces the battery life-span [16]. It is believed that constant charge-discharge cycles accelerates the reduction in battery capacity. However, this is contradicted according to studies [17] and other research which state temperature due to sustained charging/ discharging has a greater role to play on the degradation and quick burst of current can help maintain SOC reducing the duration of continuous charge helping with battery life-span. In any case, it is critical to know the limitations of power demand over time in order to select the suitable cells. Thus, the BMS should be designed to consider battery pack temperature to ensure long operating life. This phenomenon is to be verified with the chosen cells.

2.2.2 Motor

PM motors are the most widely employed type for e-bikes as they have good efficiency and energy density. There are two type of motors based on their windings (concentrated and distributed), one which produces a trapezoidal back-emf and the other with a sinusoidal back-emf due to the differences in stator windings as shown in Figure 2-6. There is some dispute as to what constitutes a BLDC motor, for the thesis, we consider the former as BLDC motor and latter as a PMSM (Permanent magnet synchronous motor) though commercial terms are interchangeable. Electric motors can be represent by Equation 2.2.

$$V_a = i_a \cdot R_a + L_a \cdot \frac{di_a}{dt} + e(\omega) \tag{2.2}$$

where,

V_a is the voltage at the motor terminals,

R_a is the resistance of stator windings,

L_a is the equivalent stator inductance,

i_a is the stator current,

e(ω) is the back-emf induced as a function of rotor speed. This indicates that the as the motor speed increases, the back-emf (e) increases which requires higher terminal voltage.

We classify motor based on their location in the bike.

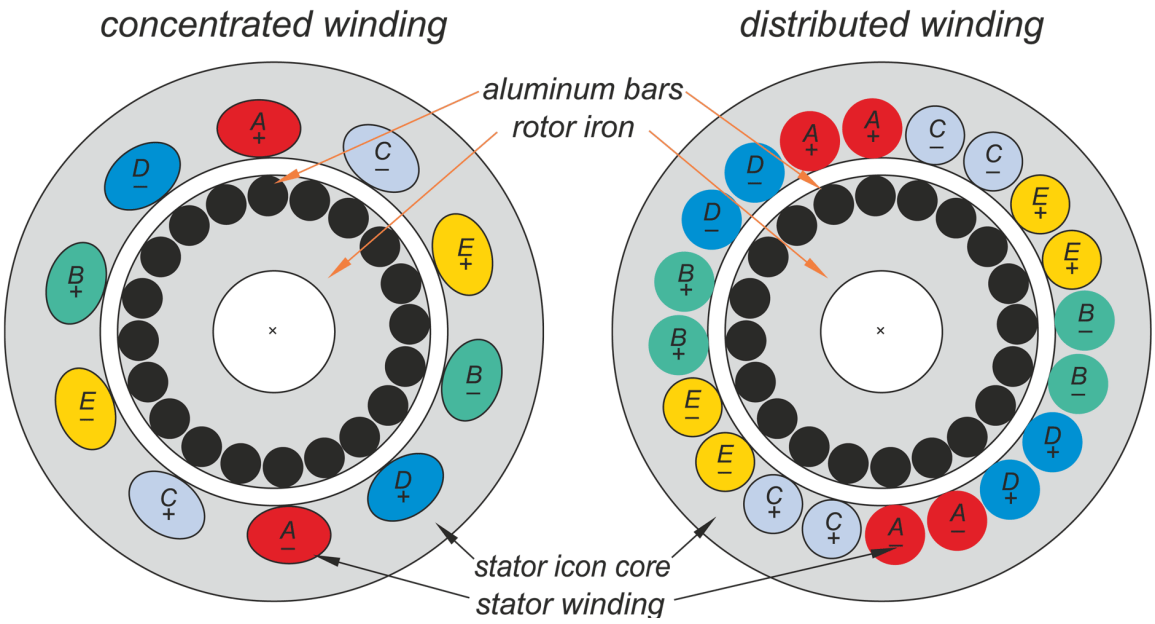

Figure 2-6: Concentrated vs distributed windings from [2]

1. Mid-drive

   Mid drive motors are connected to the crank via a speed reduction gear. This enables motors that can produce crank torque upto 120 Nm. Certain motors can produce as much as 180 Nm at the crank. This coupled with the fact that the system has access to all the gears of the bike makes it more efficient at all speed ranges. Mid-drive motors are generally IPM as they can leverage the fact they can be operated at lower torques at higher speeds in the Field weakening region. Two mid-drive motors from the Bianchi e-bike range were disassembled. The motors are not identified by their brand and instead referred by numerals.

   (a) Mid Motor-1

   This is a 250W motor with peak power of 500W with a weight of 2.8 kg. It

is the lightest and most powerful motor used by Bianchi. A reason for this is the relatively high speed operation of the motor. The gear ratio between the crank and the rotor (α) is about 44 resulting at a rotor speed of 4400 rpm at a crank speed of 100 rpm. This is twice as high as the Mid-motor2. The motor and its dis-assembly is presented in Figure 2-7 and Figure 2-8

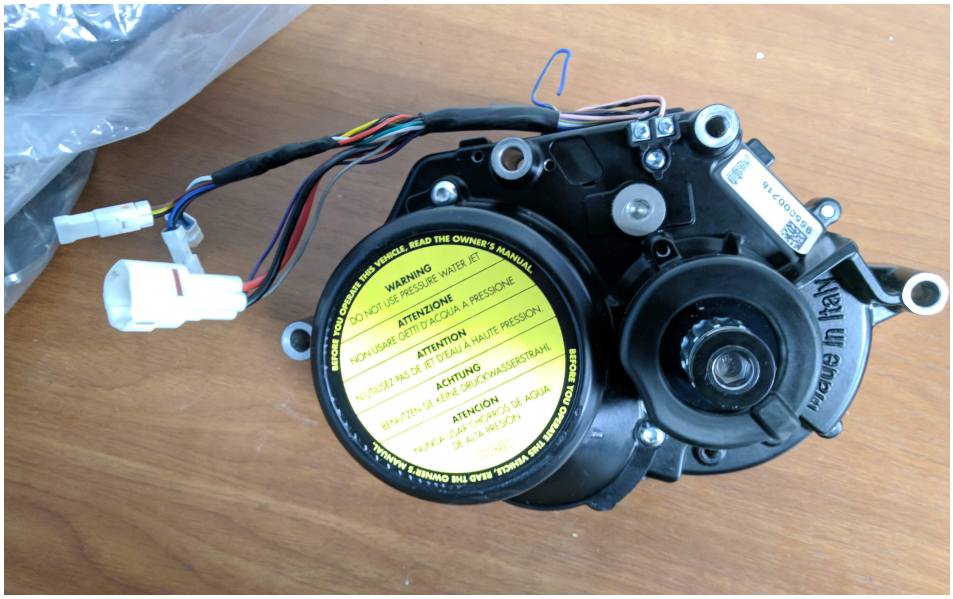

Figure 2-7: Mid motor-1

The motor has all the electronics with the sensors (torque, cadence) embedded inside the case while the speed of the bike is measured with a magnet placed on the spokes of the rear wheel.

(b) Mid Motor-2

The mid motor-2 is 250W rated and has an α of around 24, the motor weighs 4 Kg and has a similar range of sensors as the mid motor-1. The internals of the motor is shown in Figure 2-9

To achieve the best performance of the motor, vector control is adopted in all mid-drive motors which requires accurate position estimation of the rotor. Since traditional position measurement using optical disk, resolvers take up more space, a magneto-resistive sensor is used. The resistance of the sensor changes with the orientation of the magnetic field which is

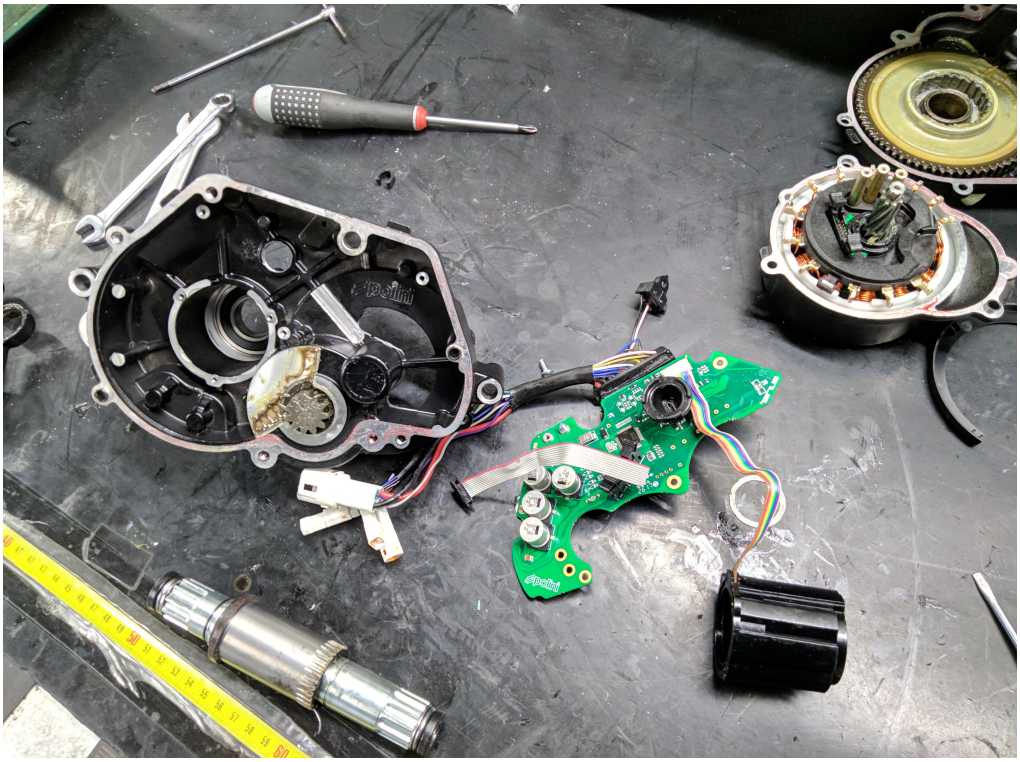

Figure 2-8: Disassembly of Mid motor-1

placed in a wheatstones bridge to eliminate thermal drift. The application note of the KMZ60 used in the mid motor-2 system gives further details [18].

Torque sensor

Torque sensor is an important device for e-bikes as they cannot legally contain an actuation mechanism like a throttle to regulate the electrical assist. The assist depends on the torque applied by the rider. A number of principles and variations of torque sensors exist. Early torque sensors were places on the rear drop-out which employed strain gauges. As manufactures began designing frames for e-bikes, the torque sensor has been integrated in the crank. Presently, inverse magnetostriction is the most commonly used principle for the torque sensing as it can be integrated into tight spaces and its measurement is simpler than strain-gauges. It can measure torque applied on the left and right cranks separately [19] [20]. A commonly used torque sensor in many OEM solution is

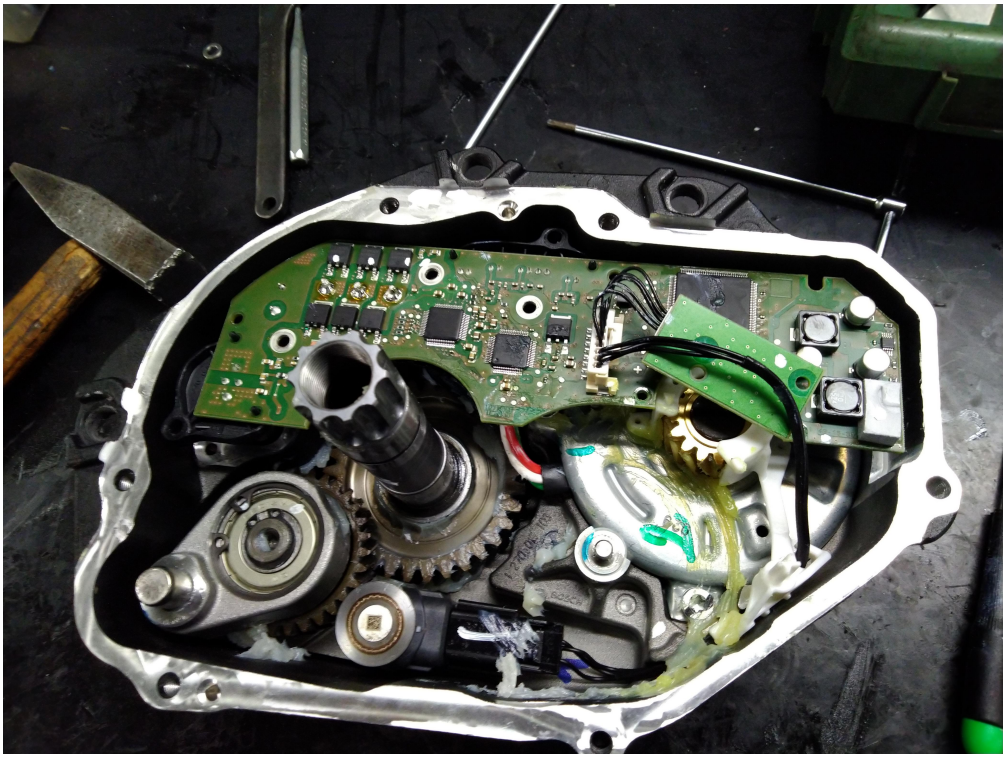

Figure 2-9: Mid Motor-2

[21], in addition to torque, they typically employ a hall sensor to measure the cadence.

2. Hub-motor

   There are several variants in hub-motors but we classify them as-

   (a) Direct drive

   These motors have an inner stator with the windings which replaces the standard hub of the wheel and outer rotor with PM magnets which connects to the rims via spokes. They have high pole pairs (upto 48) and operate at low speeds 30 rpm which requires higher torques to be developed. This results in a larger, heavier motor for the same power. They do not have a free-wheel clutch which enables regen but also causes cogging torque to effect the performance. Direct drive motors can produce upto 50 Nm of wheel torque but can be overloaded for longer periods of time due to the thermal inertia of the stator. Bianchi currently do not employ

direct drive motors. A generic direct drive motor is shown in Figure 2-10.

Figure 2-10: Direct drive hub motor

(b) Internally gear hub-motor

These types of motor employ a reduction gear within the hub which enables the motor to spin faster relative to wheel resulting in a smaller and lighter motor compared to the direct-drive ones. These motors can either have an inner-stator outer-rotor, see Figure 2-11a or an inner-rotor outer-stator arrangement. The former is the most common solution.

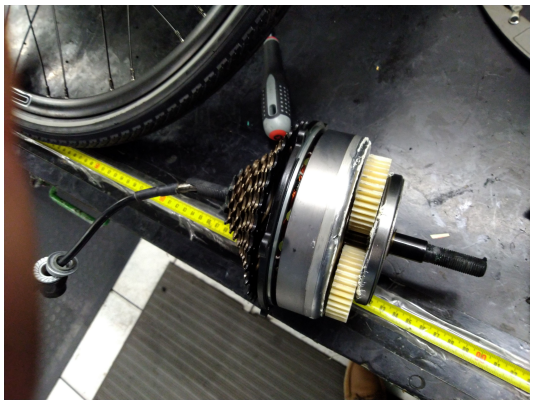

(a) internally geared hub motor-1

(b) internally geared hub-1

Figure 2-11: internally geared hub-1 dis-assembly

The gear reduction is done using a planetary gear system. The ratio depends on the application, with a typical ratio of 1:11 for city bikes and 1:5 for treking and MTBs. A toothed hub as shown in Figure 2-11b. High gear

ratio increases losses. The presence of these gears results in messing looses and typically accommodates a uni-directional clutch which freewheels and prevents regen and cogging torque.

internally geared hub-2

The internally geared hub-2 smart hub is an interesting motor as it is an internally geared hub motor with integrated batteries and the capability of regen braking. It is a 250 W motor with a 160 Whr battery weighing 3 Kg. The motor was disassembled and examined. The motor is shown in Figure 2-12. It consists of the cells on the outer periphery which encircles the motor. There are two distinct electronic boards, the circular one for the motor control and the rectangular one for the BMS and the connectivity features. The input stage of the three-phase inverter has a set of MOSFETs connected back to back in series. This configuration helps to disconnect the battery from the motor windings at speeds that the back-emf of the motor is higher than the battery voltage(35 Kmph, varies based on the SOC).

2.2.3 Electrical Architecture

As with the wide range of components to select from, there are a number of Power electronic architectures to choose from. We compare two of these. Our use of hub motors for an s-pedelec system requires the DC link voltage to be high enough to reach speeds of 45 Kmph as seen from (2.2). The maximum nominal battery voltage for e-bike is governed to 48 V [15]. But typically, e-bikes use 36V battery packs and as majority of e-bikes are pedelecs, the motors are designed to reach speeds of ≈30-35 Kmph. Since, the decision to use off-the shelf motors was made, we had two options to achieve the higher speeds of the motor required.

Boost converter

The solutions consists of a boost converter in series with the battery pack to increase

Figure 2-12: internally geared hub motor-2

the DC link voltage to the desired value as shown in Figure 2-13. This is employed in electric cars to achieve high DC voltages for the motor and maintain the DC link voltage at low SOCs when the battery voltage reduces which helps in achieving higher speeds even at low SOC.

Direct connection to inverter

A 48 V nominal battery is used and the boost converter is eliminated as seen in Figure 2-14. Depending on the cells selected, the discharge out voltage can be as low as 42 V. This prevents the motors to reach higher speeds but might be a desirable feature to limit the bike speeds when SOC is low. Using a higher battery voltage reduces the current for the same amount of power which reduces heat dissipation in

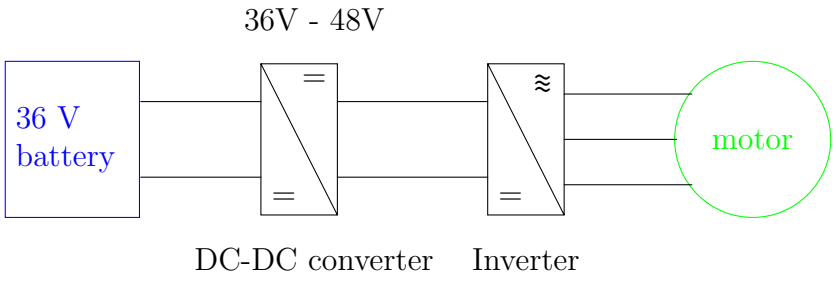

Figure 2-13: Power topology with Boost converter

the battery pack. This also results in faster charging rates. Thus, for the application, a 48 V battery is preferred over the use of DC-DC converter.

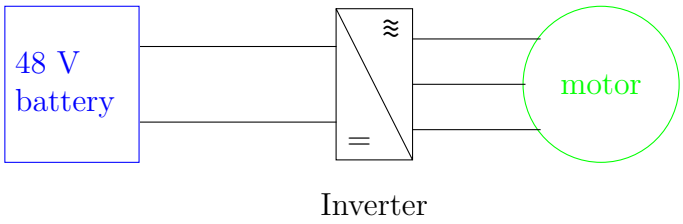

Figure 2-14: Power topology without Boost converter

2.3 Control

A typical control structure of the e-bike is shown in Figure 2-15. All the processing in the micro-controller is depicted in black while sensors in blue and the motor in green. The primary input to the control comes from the torque sensor that provides both rider torque and cadence data. This gives the rider power. The assist mode and the bike speed, measured as the wheel speed is used to determine the torque from the motor based on the torque map. This required torque is split between the front and the rear and the corresponding currents are demanded from the motor. The motor controller produces the PWM signals to drive the motors and the motor currents are feedback.

According to Figure 2-15, the thesis researches on the controls methods embedded in the block 'Torque split' as indicated in Figure 2-16 The various functions are highlighted in List 2.3.

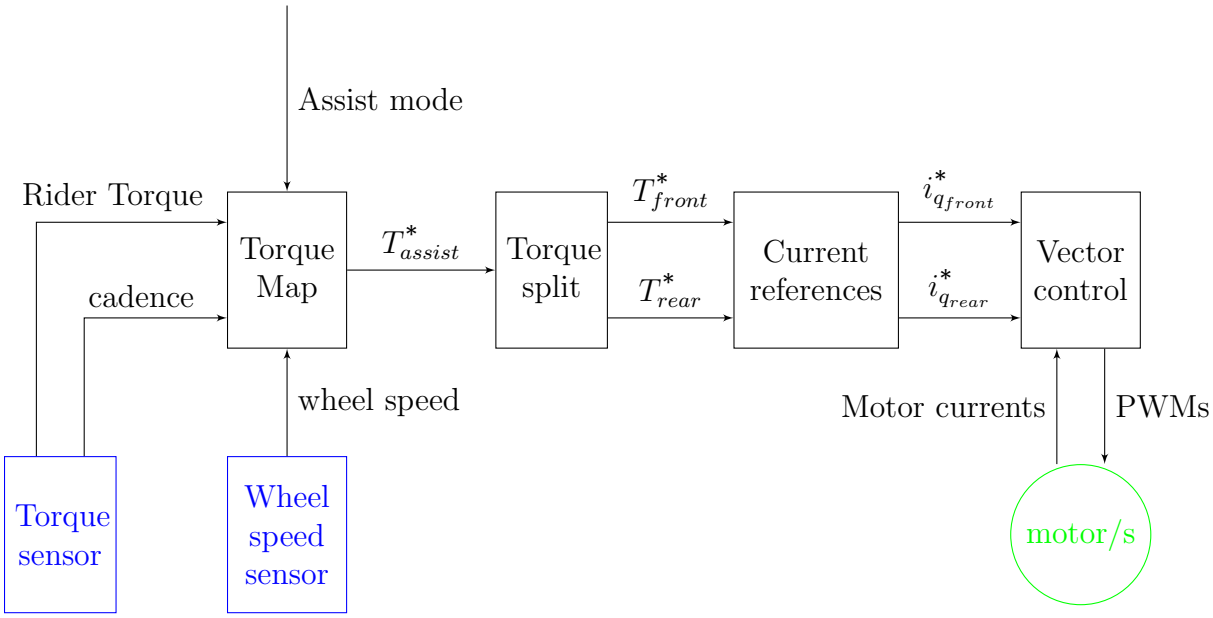

Figure 2-15: General structure of e-bike control

- TCS - Determines the torque references for each wheel such that wheels do not slip as explained in Section 2.5.
- ABS - explores the methods to achieve ABS functionalities using the hub motors at each wheel as explained in Section 2.4.
- weight transfer - as the weight of the bike shifts between the front and rear wheels, the torque split between the two is varied based on inclination, roll angle as shown in Figure 6-2.

2.3.1 Torque assist map

The torque assist provided depends of the speed of the bike so as to not exceed the average power. This assist map can be changed depending on the type of road surface, assist mode, etc. It can be different for a commuter bike, performance bike or an MTB. The most simplest and widely used map is one which provides maximum torque at zero speed and gradually reduces to zero torque at 45 Kmph. Considering a 29 inch wheel, the selected map is shown in Figure 2-17b and Figure 2-17a. The

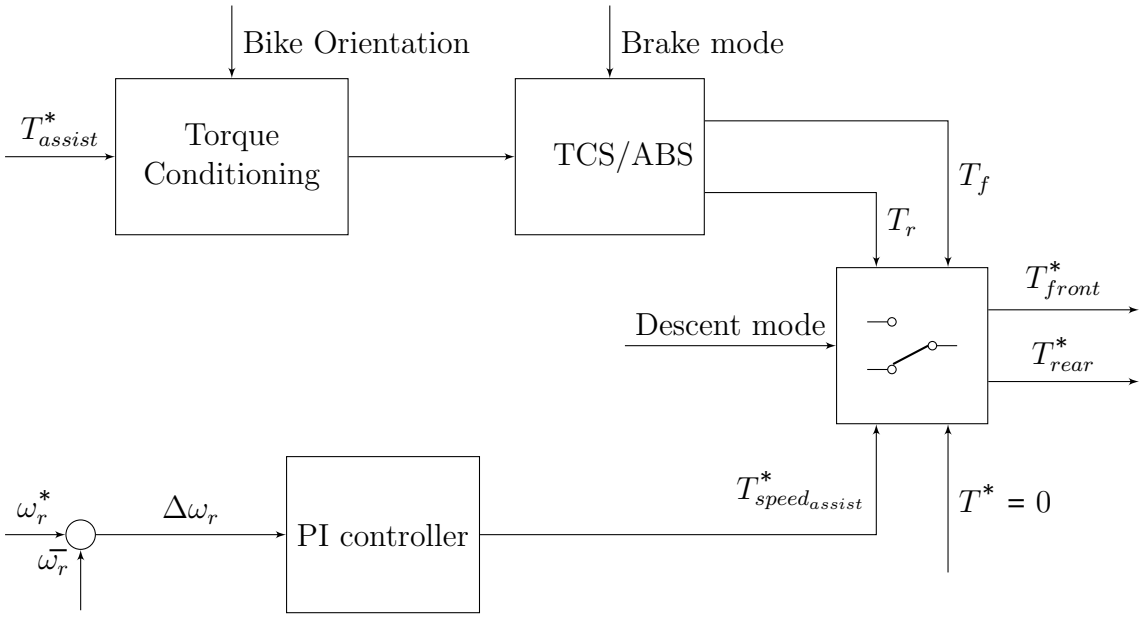

Figure 2-16: Torque split in e-bike control

amount of torque assist is proportional to the torque applied by the rider on the crank which is measured by a torque sensor.

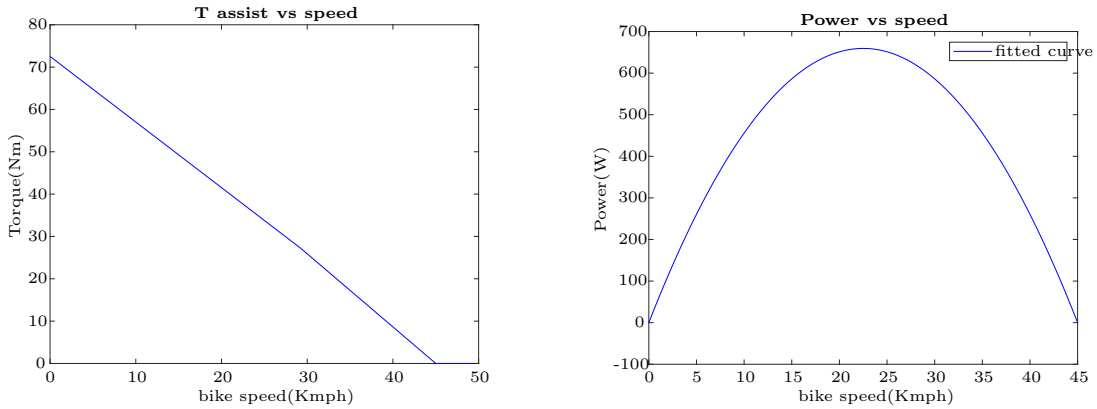

(a) Max Torque assist vs bike speed

(b) Power vs bike speed

Figure 2-17: Power and torque demand based on the linear torque mapping

2.3.2 Motor control

Mid-drive motor drive

Vector control provides the most efficient and flexible way of controlling the motor. However, they require a good measurement of the rotor position as mentioned and

hence are used in all mid-drive motors where measurement is easier. Vector control aid in efficient control of motors using MTPA and field weakening. Though sensorless algorithms exists, they are typically not employed for vector control and reserved for scalar control (Block commutation).

Hub-motor drive

Hub motors have physical constraints that make the inclusion of an accurate position sensor very challenging. They typically employ three-hall sensors displaced by 120° that changes its state relative to the PM position on the rotor.

BLDC motor A BLDC can ideally operate with constant torque if the phase currents are rectangular but is not the case as the motor inductance prevent sudden changes in current making it trapezoidal. This causes torque pulsation. The simplest method employed is the block commutation operates the motor in six steps based on the position. the amount torque can be controlled by employing a PWM on one/ both of the switch pair which controls the current. The operation is detailed in [22].

PMSM PMSM have almost entirely replaced BLDC motors as they have lower torque ripple and their control has become very economical with advancement in electronics. Most commercial drives employ a simple sinusoidal PWM control. It works by generating reference currents for the three phases and regulating the voltage required for these currents using a PI and employing PWM [23]. This method does not require the knowledge of machine parameters and is simple compared to vector control. They can also be operated at higher speeds in the field weakening region by introducing addition lag of the phase voltage w.r.t to the phase current [24]. It requires good knowledge of rotor position, hall sensors have poor resolution. There are many ways to predict the rotor position but the simplest and the most used method is by interpolating the consecutive positions with the knowledge of the speed. This methods works well as rotor speed changes slowly between two constitutive position readings except in the case of internally geared motor during loss of tyre contact with the road when hitting pot-holes, etc [25].

Vector control is the high performance algorithm and requires good machine parameter knowledge. There are a number of commercially available controllers available, one such can be found [26]. Sensorless FOC controllers are also available but they form only a small portion of the market. Though high performance controllers have on-line parameter estimation, no such commercial controller for e bike was encountered. Vector control can give us very good dynamics response (100-200 Hz) while mechanical systems have a dynamic response of 5-50 Hz. This difference in dynamics is very useful for ABS/ TCS.

2.4 ABS

ABS stands for 'Anti-locked braking system'. It prevents the lock-up of wheels during heavy braking aiding in adhesion of tyres to the road surface and preventing sliding of bike which can hurt the rider. ABS is an a well-know technology and has been used on motorbikes since the 1990s. In EU, ABS are mandatory for all motorbikes sold. However, ABS for E-bikes are not common even with well know benefits. The most well know ABS system for E-bikes come from Bosch which works only with hydraulic disk brakes as it uses a actuator to release or apply brake pressure. This systems works only for the front wheels and uses two wheel speeds sensors on both wheels, the difference in both wheels is used to detect slip and corrective action is taken. A similar system is offered by Blue-brake. This principle can be employed with the motors providing additional torque to overcome wheel-lock as discussed in 4.3.

2.5 TCS

Traction control system (TCS) aims to achieve the same as ABS but by preventing excessive sliding of the wheels under heavy accelerations or loose surfaces. However, unlike ABS, a TCS need to be much more precise as this constraint can limit the performance. This requires good understanding of bike dynamics which is focused

in Chapter 3 and how the properties of electric motors can help. Traditional TCS systems were rule based and did not offer great performance. Modern systems are more precise. TCS is available for motorbikes. However, no such system for E-bikes exists in the market. A brief idea of the existing safety systems are presented in [27].

2.6 Summary

We have seen how the different architectures of E-bikes on the market and the pros and cons of each. Though not the typical solution, the current application demands the need for hub motors to fulfill the requirements. The proposed architecture of the E-bike is shown in Figure 2-18. It consists of hub motors on both wheels with a battery on the downtube that as it helps with a more balanced weight distribution. The batteries suitable for the application were considered. LFP cells is the ideal choice from an electrical point of view as it enables wider downhill limiting speeds. However, the effect of higher weight needs to be justified. The different types of motor are discussed, the most suitable hub motor will be explored in the later chapters. It is chosen to use vector control for controlling the motors as accurate torque control of ABS/ TC are required. Finally, existing safety technologies for ABS/ TC for E-bikes are explored which indicates a shortage and hence an opportunity for improvement. The architecture is simple but there are only few commercial e-bikes with dual motors like Ariel rider D-class. However, no bike incorporates the safety systems discussed.

Figure 2-18: Proposed motor configurations

Chapter 3

Bike and Tyre Dynamics

Understanding of general bike dynamics and factors that influence it are required as the application is intended for recreational use; and safety systems require accurate modeling of the e-bike for the best performance. Though Bike geometry can greatly influence the dynamics, the thesis assumes a fixed geometry, while and the effects of other components are studied.

3.1 System Dynamics

The proposed e-bike consists of three different power sources at different locations on the bike as indicated in Figure 2-18. These have different characteristics and dynamics. [28] gives a good understanding of modeling procedure for an e-bike. This is extended to our model and the equations are given in (3.1-3.4).

$$T_r = J_{\omega_r}\dot{\omega_r} + B_r\omega_r - T_{L_r} \tag{3.1}$$

$$T_f = J_{\omega_f}\dot{\omega_f} + B_f\omega_f - T_{L_f} \tag{3.2}$$

$$T_c = J_{\omega_c}\dot{\omega_c} + B_c\omega_c - T_{L_c} \tag{3.3}$$

$$\text{when pedeling, } T_R = T_r + \eta \cdot T_c \tag{3.4}$$

where,

$T_{r,f,c}$ are the torque developed by the rear, front wheels and crank respectively,
$\omega_{r,f,c}$ is the rotational speed,
$B_{r,f,c}$ are the frictional co-efficients,
T_{L_r,L_f,L_c} are the load torques on the individual system that arise due to motion,
T_R is the total torque on the rear wheels due to the motor and the rider,
η is the gear ratio between the crank and the rear wheels which can be changed using gears

The combined equivalent dynamic equation of the crank and rear motor is given in (3.5)

$$T_R = J_{\omega_r}\dot{\omega}_r + B_r\omega_r + \eta[J_{\omega_c}\dot{\omega}_c + B_f\omega_c] - T_{LR} \tag{3.5}$$

3.2 Vehicle Dynamics

Longitudinal dynamics assess the motion of the bike in a straight line and lateral dynamics while the bike is turning. In the thesis, they are treated in isolation as their analysis becomes simpler by doing so. Coupled dynamics can practically be considered using multibody dynamics software.

3.2.1 Longitudinal Dynamics

Longitudinal dynamics give a good idea of the performance of the bike. They are relatively simple to model and can be accurately represented using basic mathematical equations.

The basic equations of motions are (3.6-3.11).

$$T_f - T_{L_f} = J_{\omega f}\dot{\omega}_f + B\omega_f \tag{3.6}$$

$$T_r - T_{L_r} = J_{\omega r}\dot{\omega}_r + B\omega_r \tag{3.7}$$

$$T_{L_f} = rF_{d_f} \tag{3.8}$$

$$T_{L_r} = rF_{d_r} \tag{3.9}$$

$$F_d = F_{d_f} + F_{d_r} \tag{3.10}$$

$$F_d - F_{dr} = m\dot{v} \tag{3.11}$$

where, F_{dr} is the total resistance force due to aerodynamics, rolling resistance and frictional losses.

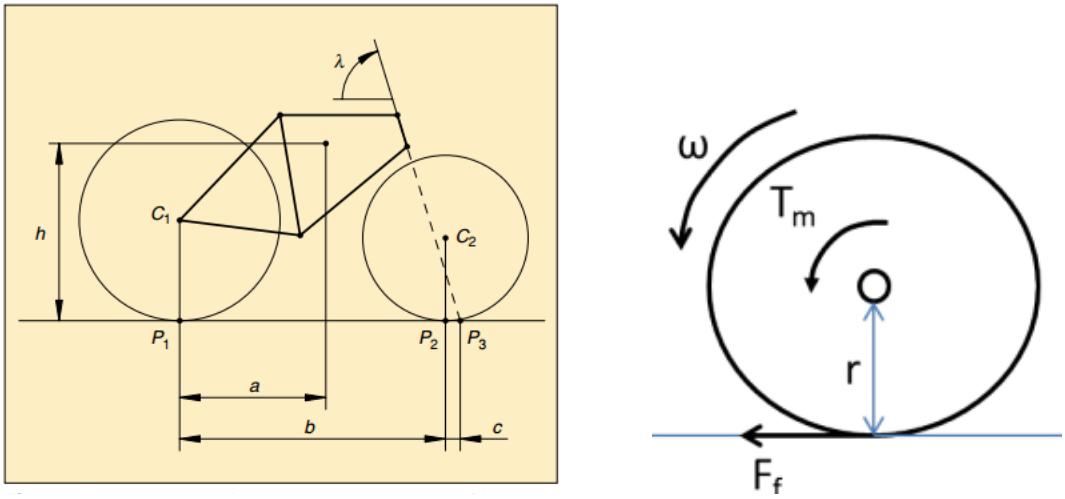

(a) Bike Model from [4] (b) Wheel force model

Figure 3-1: General bike and wheel model

With a basic model given in Figure 3-1 and Figure 3-2, Dynamic load transfer during accelerations are given by (3.12a,b).

$$F_{zf} = Mg[\frac{a}{b} - \frac{\dot{V}h}{gb}] = M_f \cdot g \tag{3.12a}$$

$$F_{zr} = Mg[\frac{b-a}{b} - \frac{\dot{V}h}{gb}] = M_r \cdot g \tag{3.12b}$$

where,

$F_{zf,zr}$ are the normal load on the front and rear wheels,

a and b are distance of the rear and front wheels for the center of mass,

V is the bike velocity,

h is the height of COG from the ground,

M is the mass of the bike.

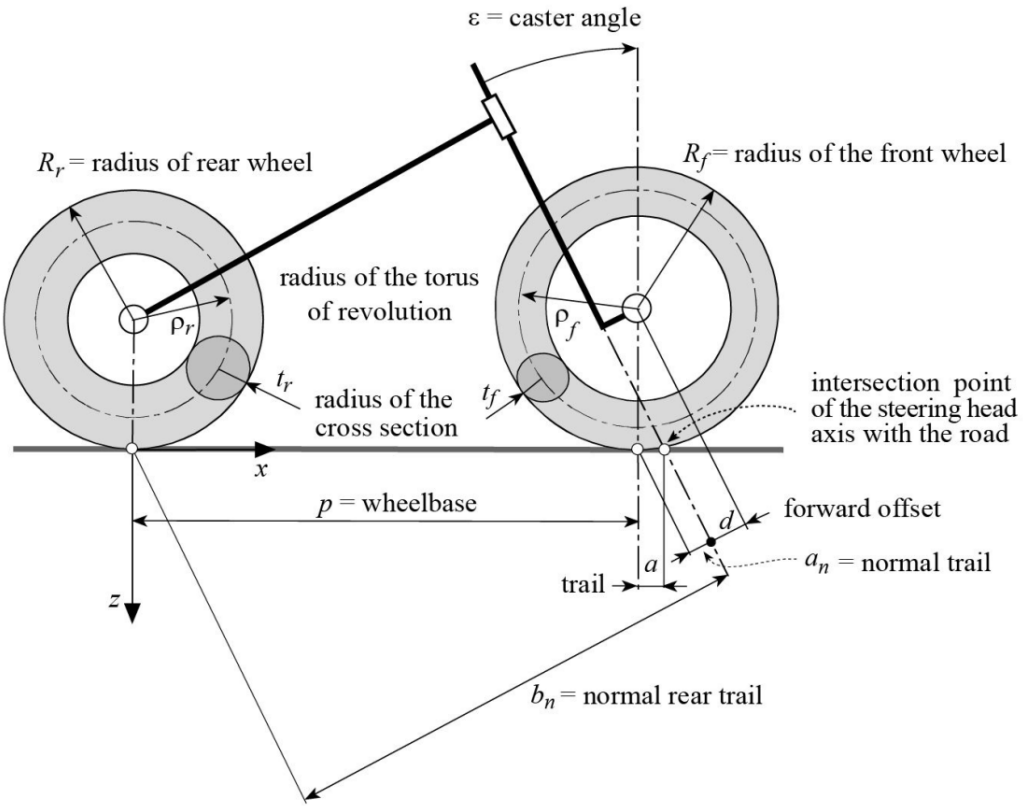

Figure 3-2: Bicycle geometry from [3]

3.2.2 Lateral Dynamics

Lateral dynamics are very important for a bike as they are the major cause of fatalities for riders. However, lateral dynamics are more complicated than longitudinal dynamics due to the increased number of variables involved. Thus, we consider concepts of lateral dynamics that are effected by selecting different components.

Steering Dynamics

Low Speed Dynamics

At low speeds, the steering is predominantly governed by the front fork angle (δ) Figure 3-1a. We analyze the effect of wheel inertia on the steering of a bike. The effect of rotation of the wheel components will be considered later. For the sake of simplicity, the motors are assumed to be cylinders of constant density. The inertia of such a system perpendicular to the axis of rotation is given by $J_{steer} = \frac{1}{12}m(3r^2 + h^2)$. Since all bike have the wheels with front projection (d from Figure 3-2, taken as 0.04m) as it helps with stability [3]. From the Parallel axis theorem (3.13).

$$J_{steer} = \frac{1}{12}m(3r^2 + h^2) + m \cdot d^2 \tag{3.13}$$

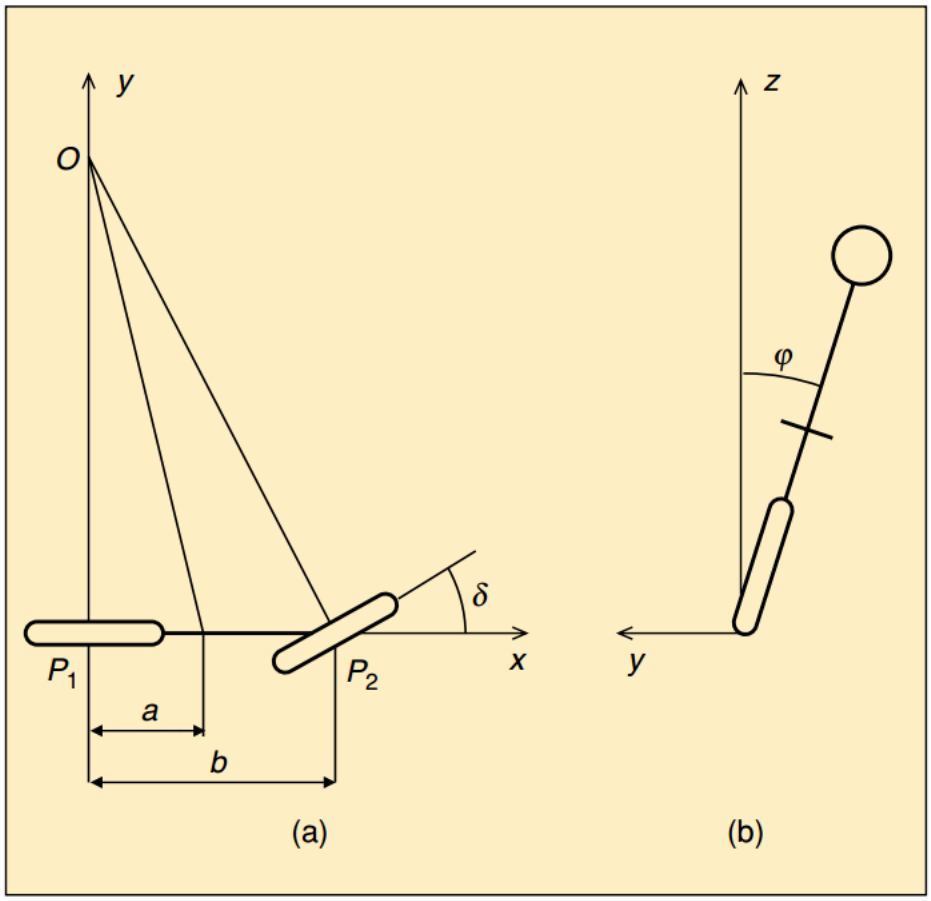

Figure 3-3: Top view and rear view of bike from [4]

From [4], we model the front fork dynamics,

High Speed dynamics

As the bike moves, the wheels rotate. The rotating components of the wheels act as a gyroscope when axis of motion is different from the axis of rotation, i.e, during steering. The phenomenon is explained in section 8.2 of [3]. This gyroscopic effect prevents the change in direction of the wheel and produces a moment against the direction of inclination, opposing the change in direction given by (3.14).

$$M_g = J_{wf} \cdot \omega_f \cdot \dot{\delta} \cdot cos\ \epsilon \tag{3.14}$$

Effect Of Yaw We consider the bike under yaw. This happens when the rider changes turning radius of the bike. Considering the radius of turn much greater than wheel radius and equal inertia of front and rear wheels, the moment during yaw motion is given by (3.15).

$$M_g = J_w \cdot \omega \cdot \Omega \cdot cos\varphi \tag{3.15}$$

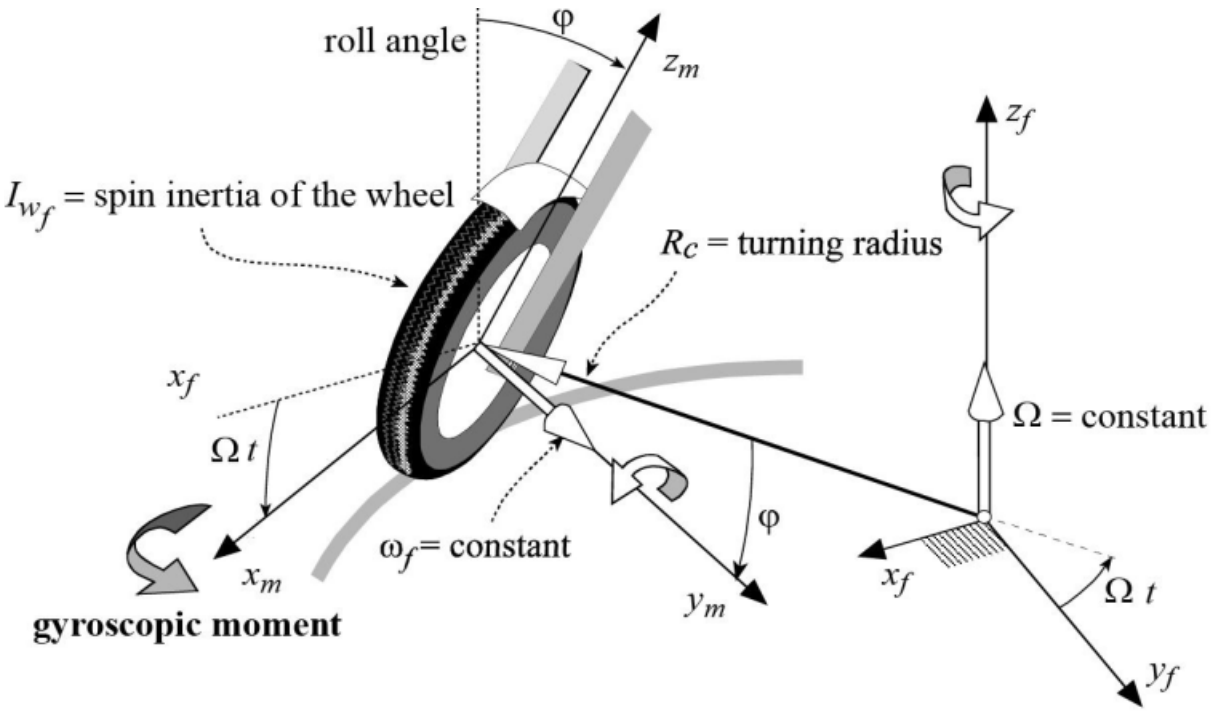

Figure 3-4: Yaw condition of bike [4]

For the bike to be in equilibrium, the centrifugal forces should balance the weight

of the bike. Roll angle is given by $\varphi = \tan^{-1}(\frac{R_c \cdot \Omega^2}{g})$. However, due to this righting moment (M_g), the rider has to lean further to counteract the effect due to the gyroscope as shown in Figure 3-5. This additional moment (M) required is given by (3.16).

$$M = -\sqrt{(m \cdot g)^2 + (m \cdot R_c \cdot \Omega^2)^2} \tag{3.16}$$

Alternatively, the rider can also instead keep his position but increase the roll angle($\Delta\varphi$) given by (3.17).

$$\Delta\varphi = arcsin(\frac{d}{h}) = arcsin\frac{J_w \cdot \omega \cdot \Omega \cdot cos(\Delta\varphi \cdot + \varphi)}{h \cdot \sqrt{(m \cdot g)^2 + (m \cdot R_c \cdot \Omega^2)^2}} \approx \frac{J_w \cdot \omega \cdot \Omega \cdot cos(\Delta\varphi)}{h \cdot \sqrt{(m \cdot g)^2 + (m \cdot R_c \cdot \Omega^2)^2}} \tag{3.17}$$

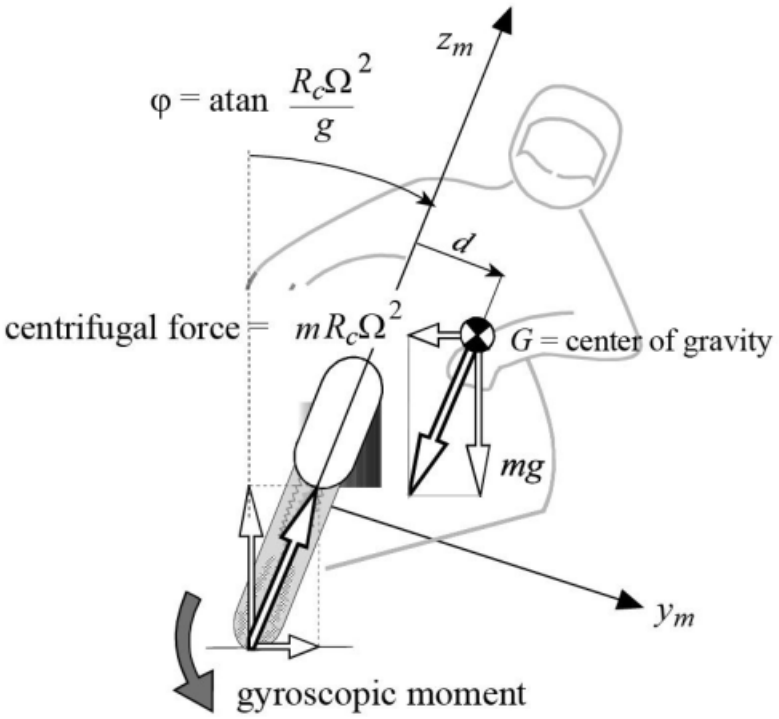

Figure 3-5: Bike during roll [4]

Effect Of Roll When the bike is under pure rolling motion, the tilting of the bike produces a moment about the steering axis given by (3.18).

$$M_g = -J_w \cdot \omega \cdot \dot{\varphi} \cdot cos\ \epsilon \tag{3.18}$$

This moment aids in the roll of the bike helping the rider to enter and exit rolls faster. This effect, unlike the other gyroscopic effects is beneficial to the maneuverability.

3.3 Tyre Dynamics

Tyre are the points of contact of interaction of the vehicle with the road. The adhesion of the tyres with the road surface is highly non-linear and depends on a number of variables like tyre pressure, construction, caster angle, slip, etc. As we consider a bike with fixed geometry, the interaction between tyre-road is vital to judge safety of bikes which depends on the slip.

3.3.1 Longitudinal Slip

Longitudinal slip is given by (3.19).

$$s_x = \frac{V_w - V}{max(|V_w, V|)} \tag{3.19}$$

The co-efficient of friction (μ_x) is modeled using a the magic formula which relates s_x to μ_x using the co-efficients (B, C, D) using the Burckhardt's model (3.20).

$$\mu_x = B(1 - e^{Cs_x}) - Ds_x \tag{3.20}$$

The relationship is represented in Figure 3-6

The equation for tractive force is given in (3.21).

$$F_x = \mu_x(s_x) \cdot N \tag{3.21}$$

3.3.2 Lateral Slip

Lateral slip is generated when lateral forces are applied to the body during turning by steering or leaning relative to the road surface. Lateral force (F_y) is given by Pacejka

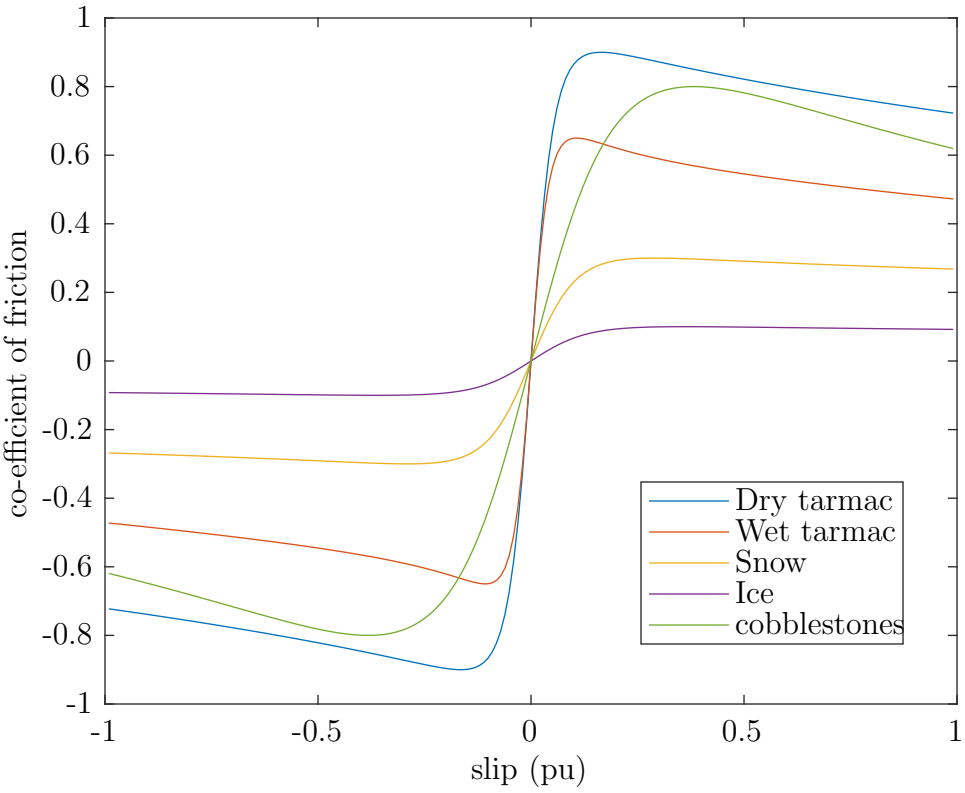

Figure 3-6: μ_x for varying road surfaces

formula (3.22), chapter 11 [29].

$$F_y = D_s N[sinC_\lambda \tan^{-1}[B_\lambda - E_\lambda(B_\lambda - \tan^{-1} B_\lambda\lambda)]+sinC_\varphi \tan^{-1}[B_\varphi\varphi - E_\varphi(B_\lambda\varphi - \tan^{-1} B_\lambda\varphi)]] \tag{3.22}$$

s = μ_y is the peak of the lateral force coefficient, D_λ C_λ $B_\lambda = k_\lambda$ is the cornering stiffness coefficient and $D_\varphi C_\varphi$ $B_\varphi = k_\varphi$ is the camber stiffness coefficient depending of tyre construction. These parameters constitute the tyre compliance.

During simultaneous lateral and longitudinal motion as is the case generally, the resultant forces lie on the friction ellipse (as $\mu_y \ll \mu_x$) as shown in Figure 3-7b indicating the resultant force is reduced under action of lateral forces. Thus, knowing the lean angle of the body is helpful in determine the lateral forces which can be done using an Inertial measurement unit (IMU).

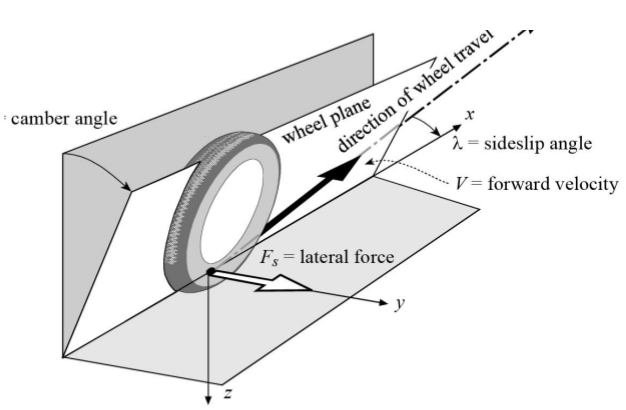

(a) side slip of tyres from [3]

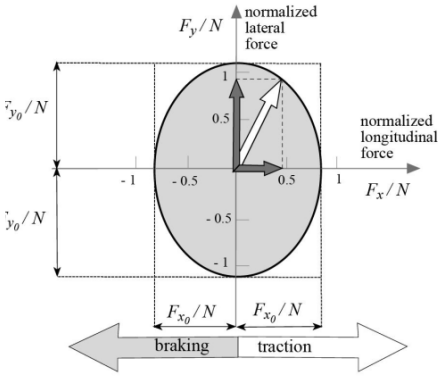

(b) Friction ellipse due to longitudinal and lateral forces

Figure 3-7: Phenomenon of lateral dynamics from [3]

The resultant tractive force given by (3.23).

$$F = \mu(s_x, \varphi) \cdot N \tag{3.23}$$

3.4 Summary

A brief discussion of the dynamic equations for modeling of the e-bike is presented. A simple bike geometry is introduced. A general understanding of longitudinal and lateral dynamics is provided. The effect of physical parameters of inertia on the motion is provided. Introduction to tyre behavior under different conditions and its effect on adhesion is indicated. The magic formula is introduced and formulated for various road surfaces that will be used in the proceeding chapters for analysis. The power-train dynamic equations are presented and the differences in it when pedaling is shown which is a factor of consideration during control.

Chapter 4

Simulation

Simulations of the various systems are performed in SIMULINK to understand the factors that will help use select the best component and design the control of the e-bike in general.

4.1 E-bike Model

The longitudinal dynamic model of the E-bike is developed as shown in Figure 4-2. The rider is modeled as a torque input to the cranks that connect to the rear wheels via a chain drive which accommodates a freewheel. All associated components of the motors, tyres and the physical characteristics of the e-bike are modeled as indicated in Table 4.1.

The parameters related to aerodynamics are taken from [30].

Torque split As there is difference in weights on the front and the rear wheels, it is better to split the torque in the same ratio. Here, a fixed ratio is chosen. Special consideration should be taken for torque demand during regen as the maximum regen power is governed by the rate at which we can charge the battery. Though, in reality, this would depend on the temperature, we model, the max recharge rate as a function of Sate of charge (SOC). It reduces gradually from maximum at 60% to minimum at 99%.

Parameters	Value
Prated (W)	400
wheel size (inch)	29
V_{nom} (V)	48
Battery I_{rated} (Ah)	14.5
Max battery discharge rate (C)	1
Max Charge rate (C)	0.5
Wheel base (m)	1.7
Frontal area (m)	0.5
Drag co-efficient C_d	0.8
cg from front wheels (a) (m)	1.02
cg from front wheels (b) (m)	0.68
Bike + rider mass (exclusive of motors) (Kg)	110
J_wheel $(Kg \cdot m^2)$	0.06

Table 4.1: E bike parameters used for longitudinal dynamic simulations

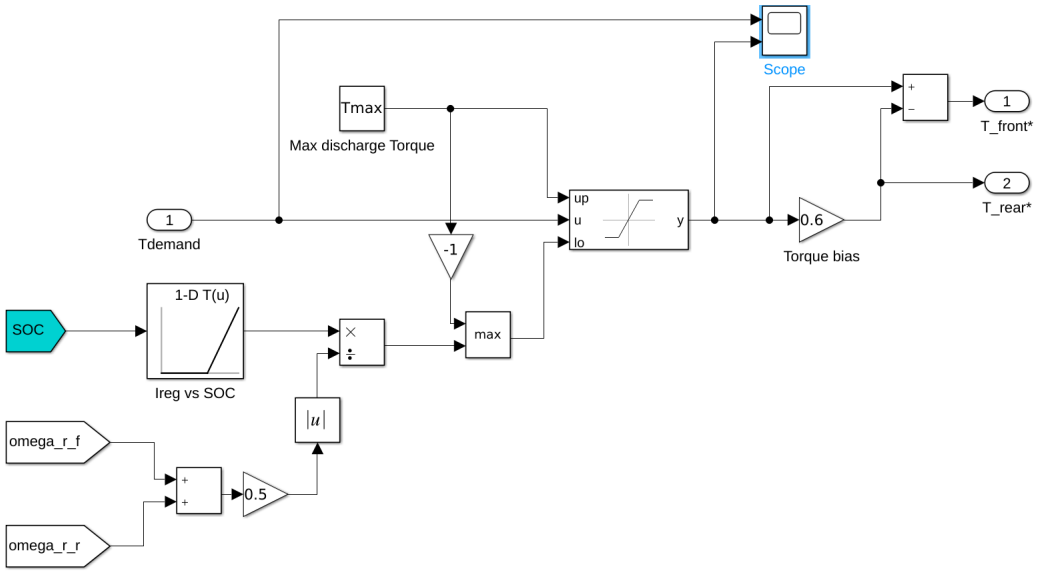

Figure 4-1: Torque limit and split between front-rear

Rear mechanical connection The rear wheel is coupled to the motor and the crank is coupled via a chain and a freewheel which are included in the simulation. This allows only positive speeds to drive the rear sprockets as shown in Figure 4-3.

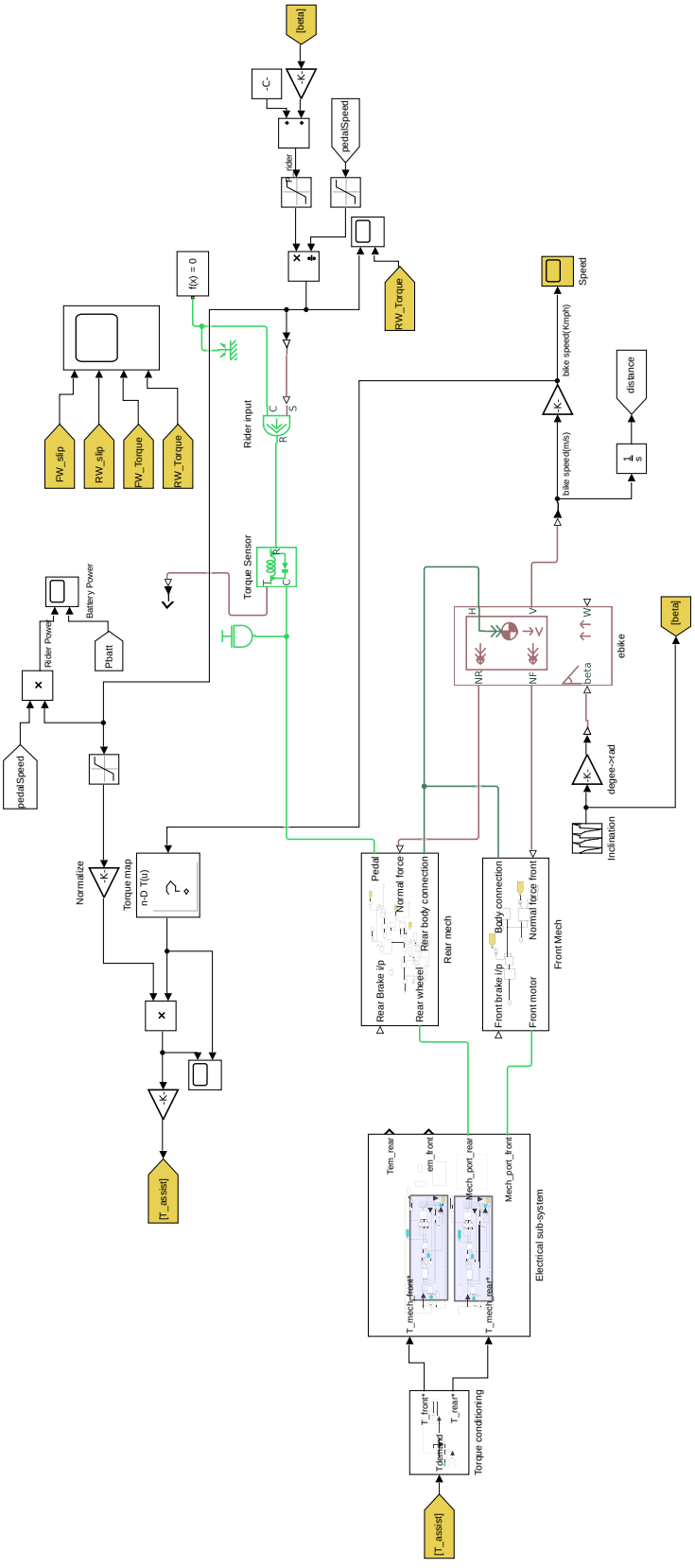

Figure 4-2: e-bike simulink model

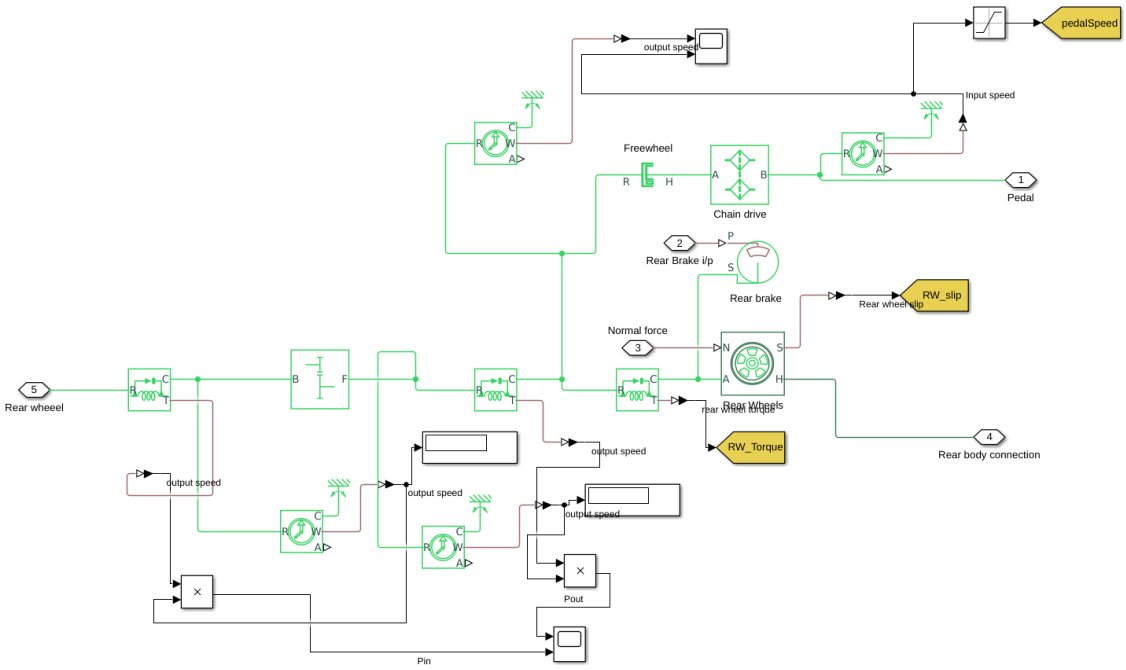

Figure 4-3: Rear mechanical coupling

4.2 Motor Control

We implement an indirect vector control for the motors as shown in Figure 4-4; for the rear motor. Vector control separates the total current into two orthogonal components (d and q-axis). For an SPM, i_q is responsible for torque production and i_d is responsible for flux. They can be independently controlled as desired in the synchronous reference frame. Field weakening is implemented by estimating the back emf at the current speed with knowledge of the motor parameters and the required i_d current is supplied.

4.2.1 Field Weakening

As we would like to reach higher speeds without necessarily doing any changes to the motor. We test the effectiveness of Field weakening. Once, the motor reaches its max speed of 25 Kmph at i_q = $10A$, we inject i_d = $-15A$, this keeps the motor and power electronics at their maximum rated operating current as shown in Figure 4-5

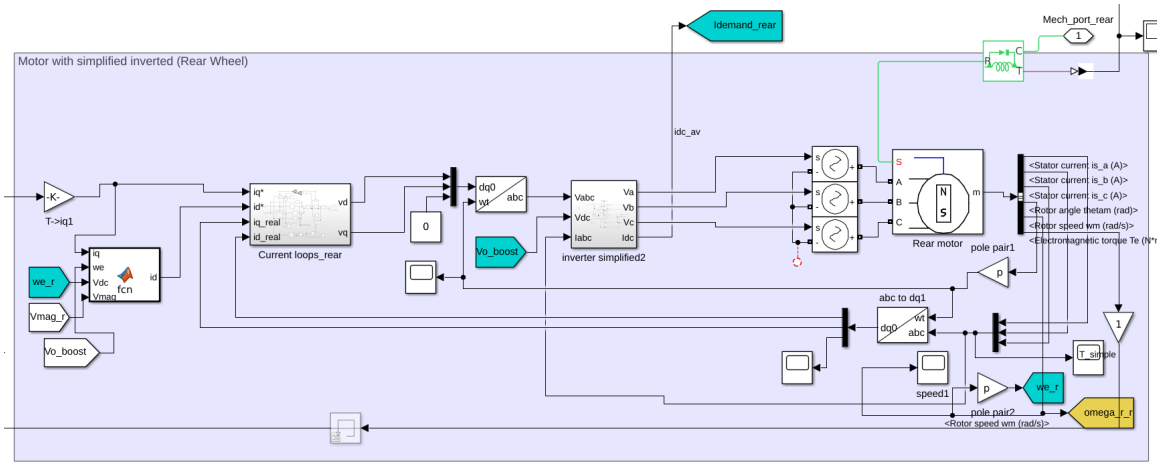

Figure 4-4: Indirect vector control scheme

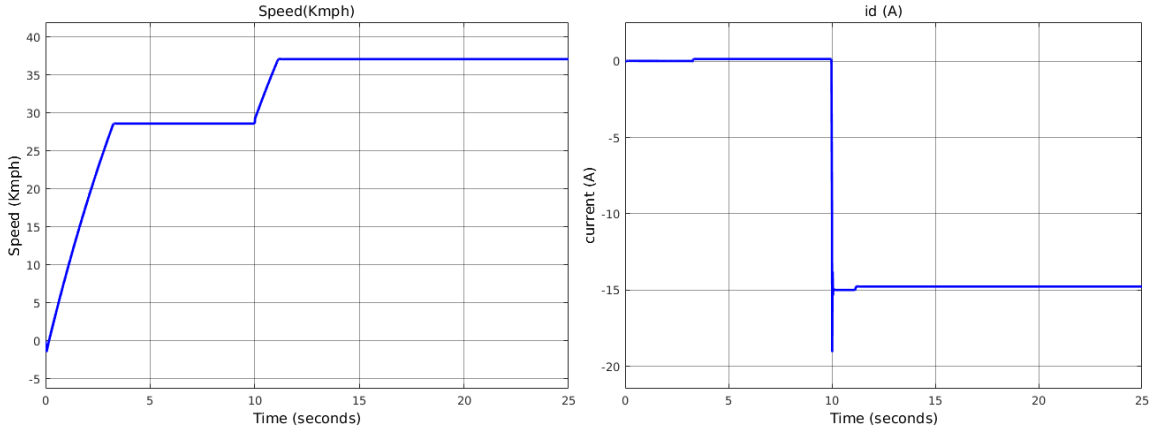

Figure 4-5: Field Weakening of SPM motor to its effectiveness to increase speed

With a d-axis current injection of -15 A, the increase in speed is from 28 Kmph to 37 Kmph. Field weaking is used if needed to reach the high-speed region.

4.2.2 Over Speeds

There is a high possibility that the bike can travel faster such that the back EMF would be greater than the DC link as the rider can power beyond this speed limit. This is simulated and presented in Figure 4-6.

The PI controller of the current loop saturates the output voltage to an achievable value by the PWM ($0.707 \cdot V_{dc}$). The difference is feedback to reduce the reference accordingly to prevent integral windup. This causes the controller to reduce i_q. The

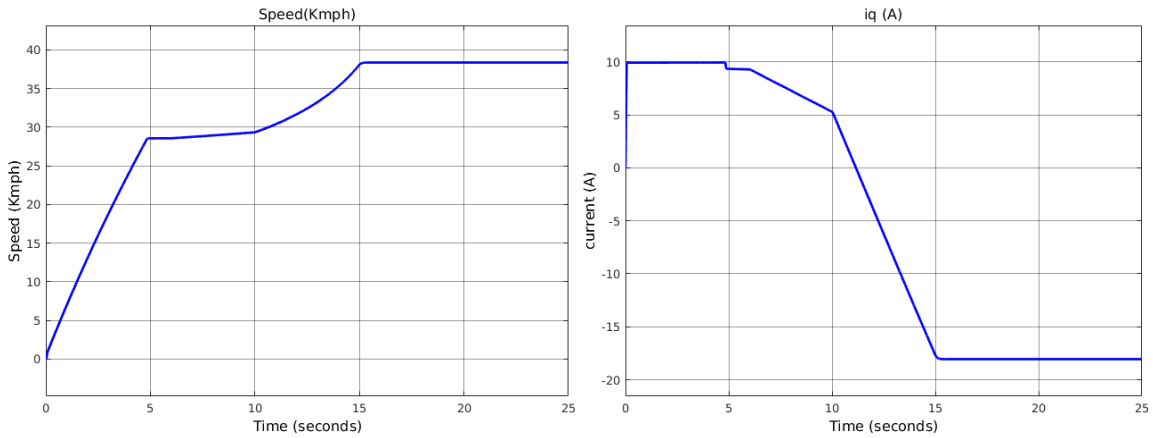

Figure 4-6: Effect of rotor speed higher than rated value and its effect on the motor currents

value depends on the speed of the motor. It can be seen that at 38 Kmph, i_q reduces to -20 A, the resultant of d and q-axis currents become greater than the limits and can cause over-current protection in the converter.

This phenomenon should be reduced by selecting the motors accordingly and the condition can be avoided by adding a switch in series to the DC link to disconnect the Battery with the motor terminals during this condition as used in the gear motor-2 2b.

As vector control requires good knowledge of motor parameters, an identification scheme, as a part of the Motorware library from TI was used. The basic working of the identification scheme is provide in [31].

The parameters are listed in Table 4.2.

Parameters	**Front Motor**	**Rear motor**
Pole Pairs	8	10
Winding resistance (ohm)	0.11386393	0.0906878784
d-axis inductance (μH)	167.174658	179.82084
q-axis inductance (μH)	167.174658	179.82084
Back emf constant (V/Hz)	0.0619320646	0.11047858
Torque constant (Nm/A)	0.1183	0.2637

Table 4.2: e-bike motor parameters obtained from by motor identification

4.3 ABS

As explained previously, ABS can be very useful by preventing locking up of the brakes. Preventing excessive wheel slip helps in increasing the amount of frictional force that is useful for traction. This helps in both reducing braking distances and more importantly keeping the rider in control of the bike during lateral dynamics (which is not consider for simulations). Though there are numerous ways to achieve the function, the logic used in commercial e-bike system of Bosch is tested.

4.3.1 Simulation Of Scalar ABS (Rear Wheel Lockup)

The same bicycle model is used and the various road- tyre relationships from Figure 3-6 are used. The model used is shown in Figure 4-7. The parameters used for simulation are shown in Table 4.3.

Time (sec)	**0- 1.0**	**1.0-1.2**	**1.2-2.0**	**2.0-4.0**	**4.0-4.5**	**4.5- 5.0**	**5.0-6.0**
Rear Braking torque (Nm)	0	130		0	130		
Front Braking torque (Nm)	0	120		0	120		
surface	dry asphalt		wet asphalt		ice		snow

Table 4.3: Surface change during rear wheel lockup

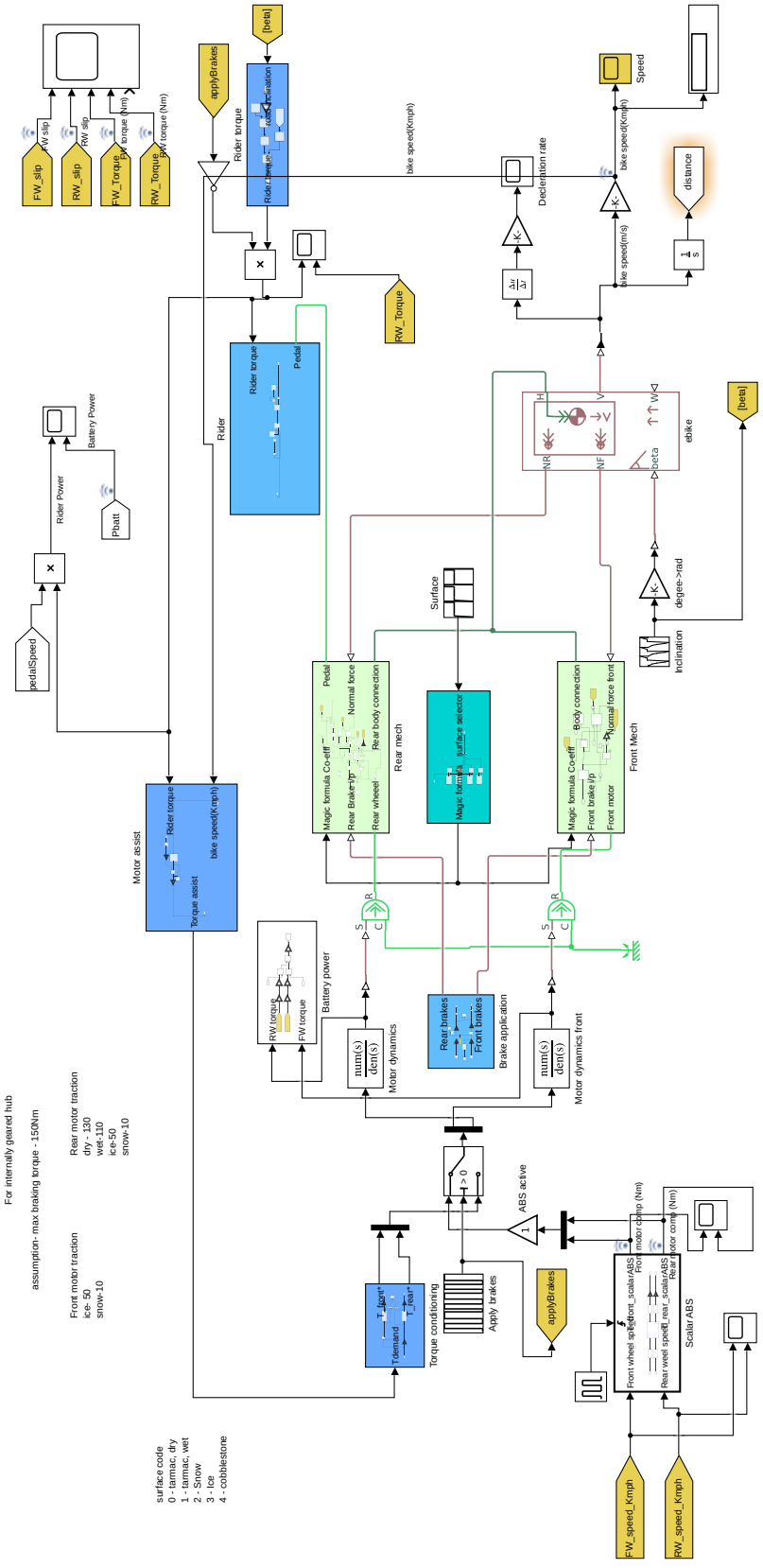

Figure 4-7: Simulation of Scalar ABS

The results are shown in Appendix B-4. We see that the the performance of the bike improves as it is able to come to a stop faster. The wheel with the greater velocity is used as reference and the locked wheel is driven with the motor within 1 kmph of this reference. This is implemented using the C-function 'Scalar ABS' in Figure 4-7. Wheel slip is well controlled as long both wheels do not lockup. Due to the high center of gravity of the system, considerable weight transfer to the front takes places during braking given by (3.12) which prevents the lock-up of front wheels under most surface conditions provided that the other wheel does not lockup.

4.3.2 Simulation Of Scalar ABS (Front Wheel Lockup)

The model used is shown in Figure 4-7. The parameters used for simulation are shown in Table 4.4.

Time (sec)	**0- 0.2**	**0.2-1.0**	**1.0-2.5**	**2.5-4.0**	**4.0-5.5**	**5.5- 6.0**
Rear Braking torque (Nm)	0		50	0	50	
Front Braking torque (Nm)	0		80	0	80	
surface	dry asphalt	ice				snow

Table 4.4: Surface change during front wheel lockup

The results are shown in Appendix B-5. We see that the the performance of the bike improves as it is able to come to a stop faster. Due to the load transfer, the front wheel lockup does not take places on asphalt where grip is high which was experienced in practice. These simulations were carried out with the motor parameters of the actual motors as seen in Table 4.2 used for the prototype and their constrains of torques. Under very poor grip conditions like snow, the motors cannot compensate for the braking torque and hence, cannot prevent lockups. This is seen at $t = 5$ *sec* in Appendix B-5. Suitable motor sizing should be done to achieve the desired performance.

4.4 Traction Control system (TCS)

Traction control systems like ABS, prevents the un-necessary slip of wheels aiding in traction. Like ABS, there are a number of control methodologies for TCS as described in [32], [33]. Maximum transmittable torque estimate (MTTE) algorithm is an interesting algorithm as it is Model following control (MFC). It does not require the information of vehicle speed or surface conditions to be know as it controls the relative accelerations of the wheels and the vehicle to limit slip. It was proposed by Dr. Hori and his research team [5]. (3.6-3.11) form the basis of the control. Defining the relaxation factor (α) as (4.1).

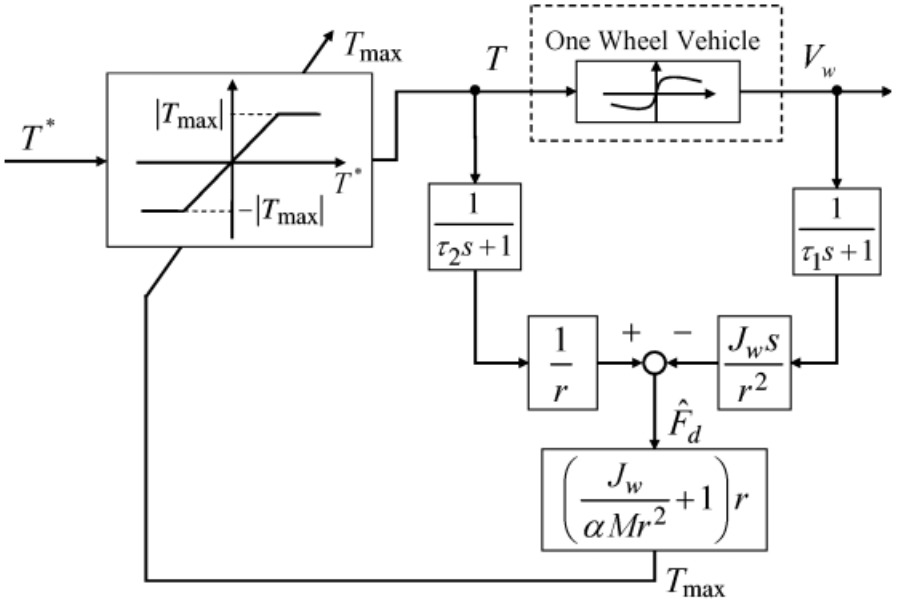

Figure 4-8: Block diagram of MTTE for a single driven wheel from [5]

$$\alpha = \frac{\dot{V}_{f,r}}{\dot{V}} \tag{4.1}$$

where, $V_{f,r}$ are the front and rear wheel linear velocities, V is vehicle velocity.

(3.6-3.11) results in the maximum torque estimates as (4.2a,b).

$$T_{r_{max}} = rF_{d_r}\left(\frac{J_{wr}}{\alpha\ Mass\ r^2} + 1\right) + \frac{J_{wr}}{\alpha\ Mass\ r^2}(F_{d_f} - F_{dr}) \tag{4.2a}$$

$$T_{f_{max}} = rF_{d_f}\left(\frac{J_{wf}}{\alpha\ Mass\ r^2} + 1\right) + \frac{J_{wf}}{\alpha\ Mass\ r^2}(F_{d_r} - F_{dr}) \tag{4.2b}$$

F_{dr} is the driving resistance required to be overcome to accelerate the vehicle. Though there are various estimation methods for each case [34], [35], we consider the simplest model given by (4.3).

$$\begin{aligned} F_{dr} &= F_{drag} + F_{rolling\ resistance} + F_{inclination} \\ &= \frac{1}{2}\delta C_d\ A\ V^2 + C_r N + N sin(\theta) \end{aligned} \tag{4.3}$$

where,

δ is the density of air,

C_d is the co-efficient of drag

A is the frontal area of the bike,

C_r is the co-efficient of rolling resistance,

N is the normal force on the tyres,

θ is the angle of inclination of the bike.

The equivalent system with MTTE is shown in Figure 4-8.

From (4.2a,b), we see that T_{max} was will be less than the driving force when $\alpha > 1$. Thus, we keep $\alpha < 1$. F_{dr} acts as a disturbance to the system and can be estimated and feed-forward to improve dynamics performance. This will be tested later. From (4.2a,b), at start, $T_{max} = 0$ which prevents any torque to be applied. Therefore, the requested torque is over-evaluated by differentiating the torque command as seen in Figure 4-9.

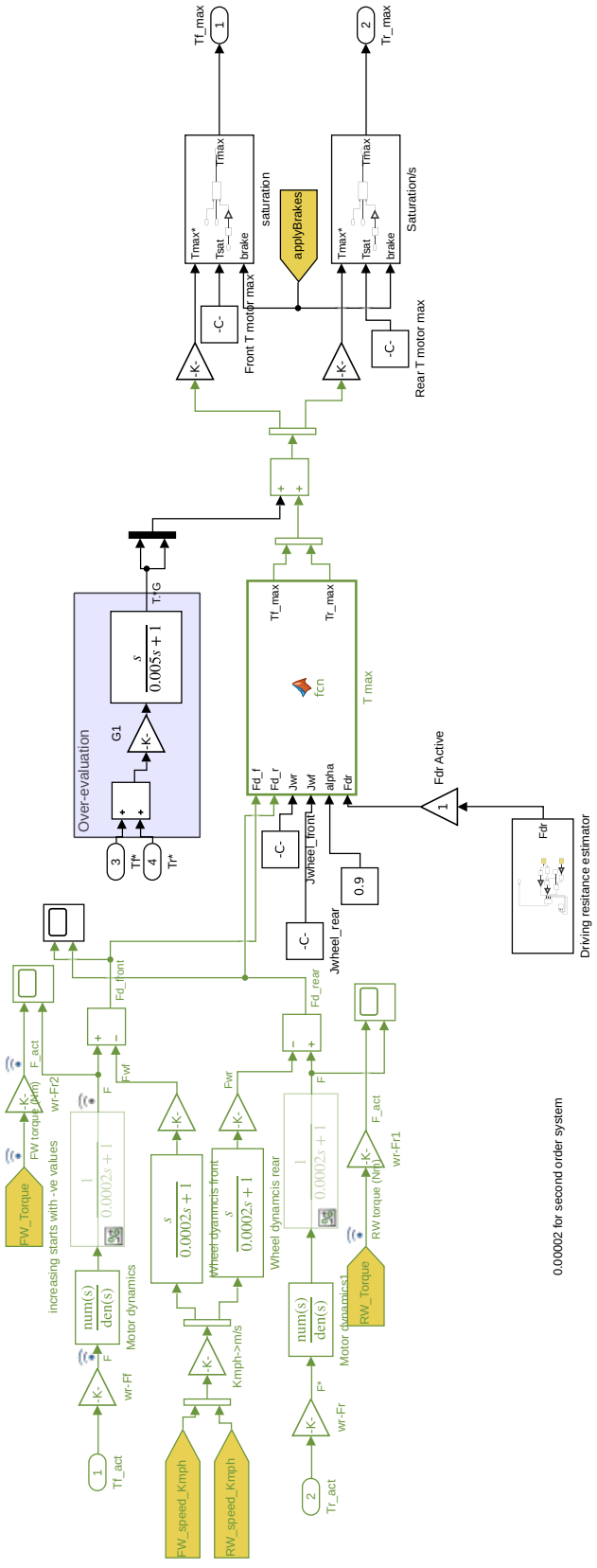

Figure 4-9: Simulink block of MTTE

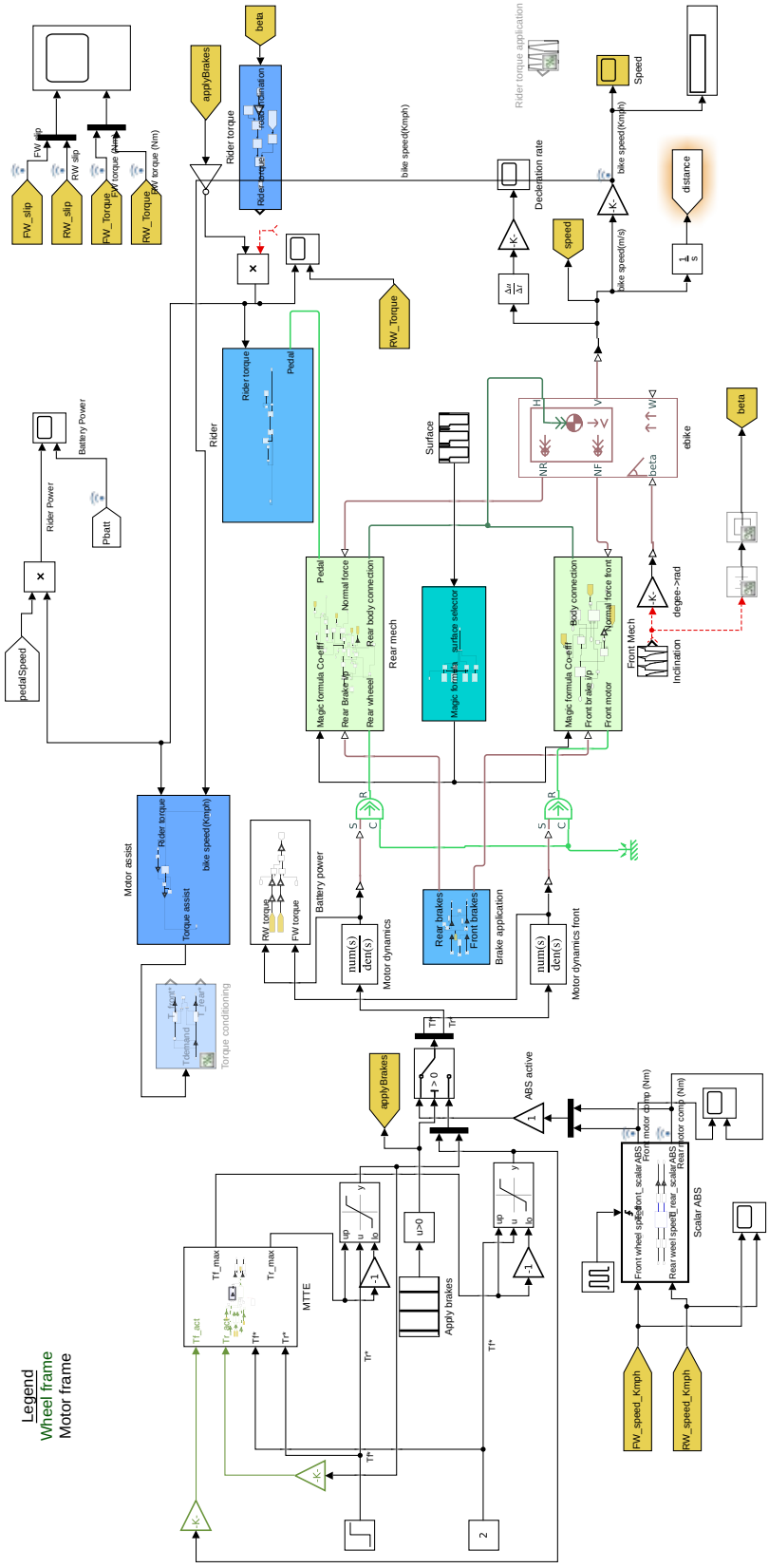

Figure 4-10: Simulink model of MTTE

4.4.1 MTTE and ABS

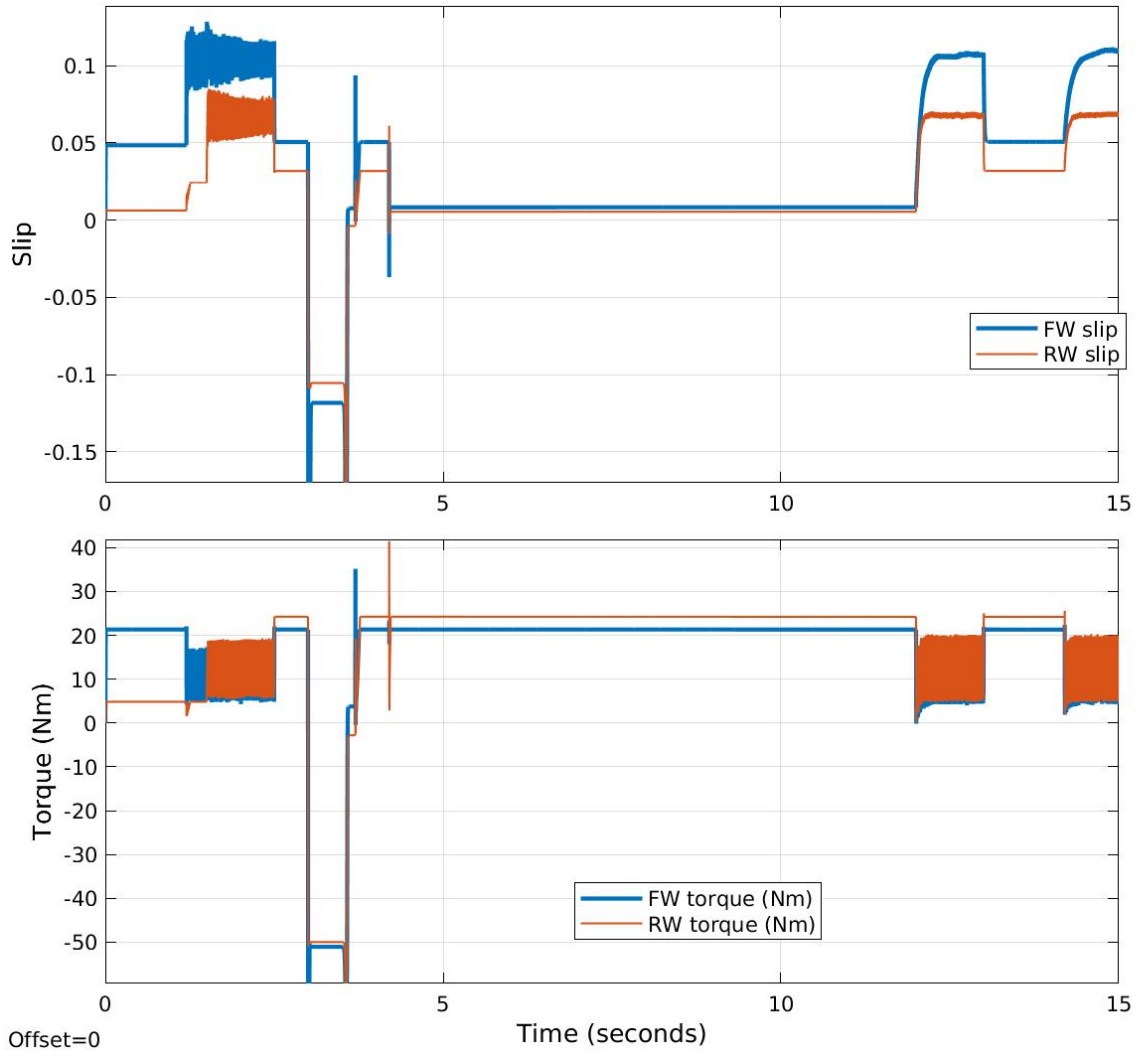

Figure 4-11: Front and rear wheel torques and slips with MTTE and ABS combined under varying surface conditions

The dynamics of the motor and road-tyre interaction is taken into consideration, while the effect of tyre compliance will be investigated later. Brakes are applied from 3.0-3.7 sec while the surface change in indicated in Table 4.5. No rider torque is applied and it is consider that rider torque is a part of the applied torque which simplifies the control for evaluation. MTTE is simulated at low speed and high speeds upto 30 Kmph. the performance is satisfactory. The control is also able to switch to the scalar ABS and rework without any problems. The simulation parameters are -

Fixed step of 1ms with automatic solver. The results of the simulation is shown in Figure 4-11.

Time (sec)	**0-1.2**	**1.2-2.5**	**2.5-3.0**	**3.0-3.7**	**3.7-4.2**	**4.2-12**	**12-13**
surface	snow	ice	snow			dry tarmac	ice
Rear Braking torque (Nm)	0			50	0		
Front Braking torque (Nm)	0			70	0		

Table 4.5: Surface change during MTTE and ABS

The design of the low pass filters are vital to proper operation. The LPF of the Wheel torque should model the actual torque response of the vehicle while the LPF of the Wheel speed can be tuned based on the sensitivity of the torque regulation required. From Figure 4-11 is it seen that under all conditions, the wheel slip in contained to keep traction. It is seen TCS performance increases such that the tyre slips under TCS operation is relatively stable at higher vehicle speeds (t=12-15 sec) compared to at lower speed (t= 1-4 sec).

4.4.2 Effect Of Incorrect Parameters

Since MTTE is a MFC, the performance of it depends on the accuracy of the estimated parameters. These parameters may not always be accurate. Thus, we see the effect of incorrect parameters on the control. These parameters that chage are.

- $\hat{J_{wheel}} = 2\ J_{wheel}$.
- $\hat{T_f}$ = 1.3 T_f.
- No F_{dr} estimation.
- $\hat{Mass}$ = 1.2 $mass$.

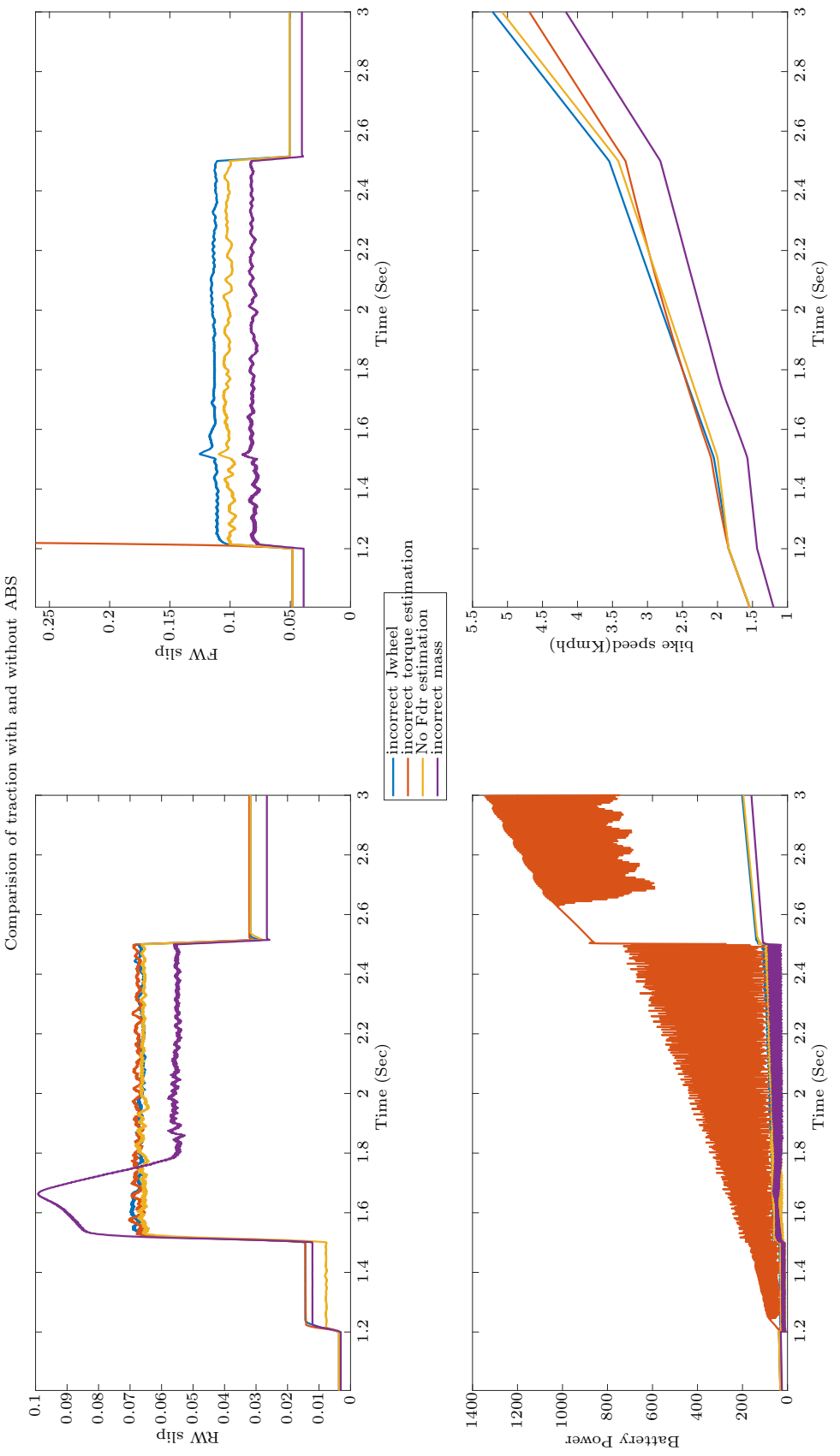

Figure 4-12: Effect of incorrect parameters with MTTE

The effect of these are indicated in Figure 4-12 whose data is filtered for better visualization. It can be seen that the rear wheel slip is negligibly effected by incorrect front wheel parameters but effected by vehicle parameters like mass and Driving force estimation. F_{dr} estimation improves slip slightly indicating that approximate estimation is sufficient. Incorrect J_{wheel} does not cause too much issue, in this case, it aids by helping the bike accelerate faster. The most significant effect is from incorrect torque estimation. This results in large slips and large battery power. This requirement of accurate estimation of torque is the reason the MTTE is not suitable for ABS applications as the braking torque is not measured. However, the most impact is due to the incorrect mass estimation which severely limits slips as seen from the speed graphs.

4.4.3 MTTE with disturbance observer

As demonstrated, the performance of MTTE is effected by the accuracy of the model's parameters. This can be a problem as these parameters are subjected to changes. Thus, we test the use of a closed loop disturbance observer as proposed in [6]. The disturbance observer tracks the changes in the physical parameters of the bike to produce estimated $\hat{F_{d_f}}$ which was previous generated using (3.6-3.11) and was dependent on the accuracy of the parameters. This is shown for a single wheel in Figure 4-13. The controller C(s) can be designed to have low bandwidth as the parameter changes are not very fast. The simulink model for the both wheels with disturbance observer is shown in Figure 4-14. The test for the incorrect parameters are performed as in the previous case with the addition of incorrect wheel speed. The results are presented in Figure 4-15. It is seen that there is a significant improvement in performance with the observer in all cases. However, incorrect torque estimation still produces the same results as in the previous case showing the importance of accurate torque estimation. This estimation can be obtained as vector control algorithm gives us the motor torques and the torque sensor provides the information of the rider torque. The effect on the performance considering the tyre compliance was simulated. The control was robust enough to provide unchanged performance.

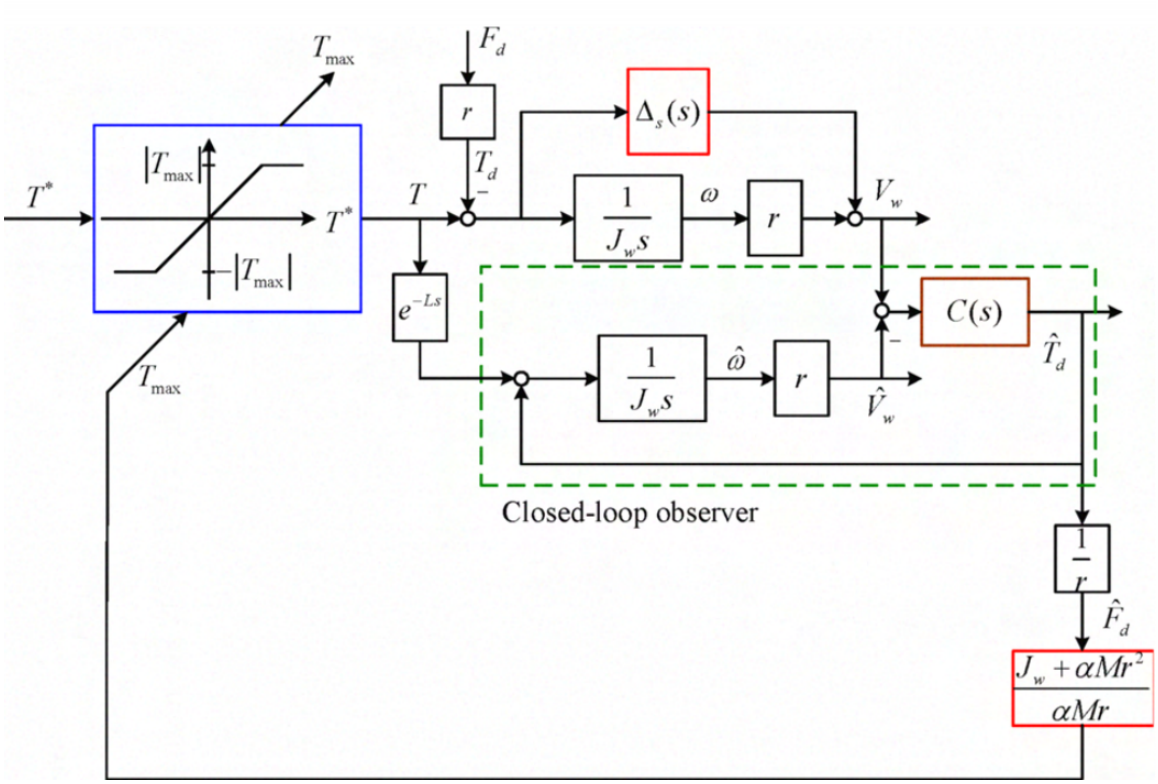

Figure 4-13: Block diagram of MTTE with disturbance observer for a single wheel from [6]

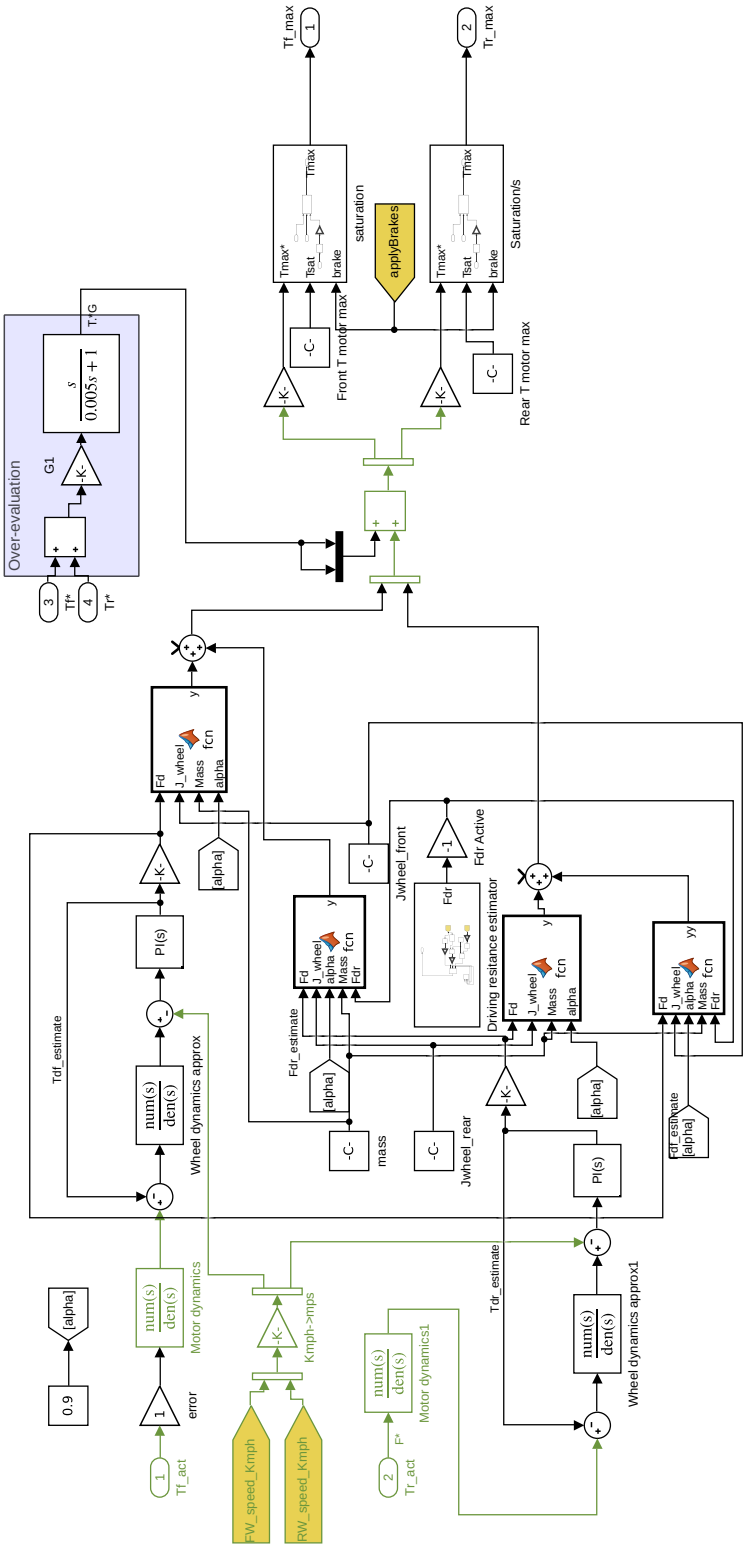

Figure 4-14: Simulink block of MTTE with disturbance observer

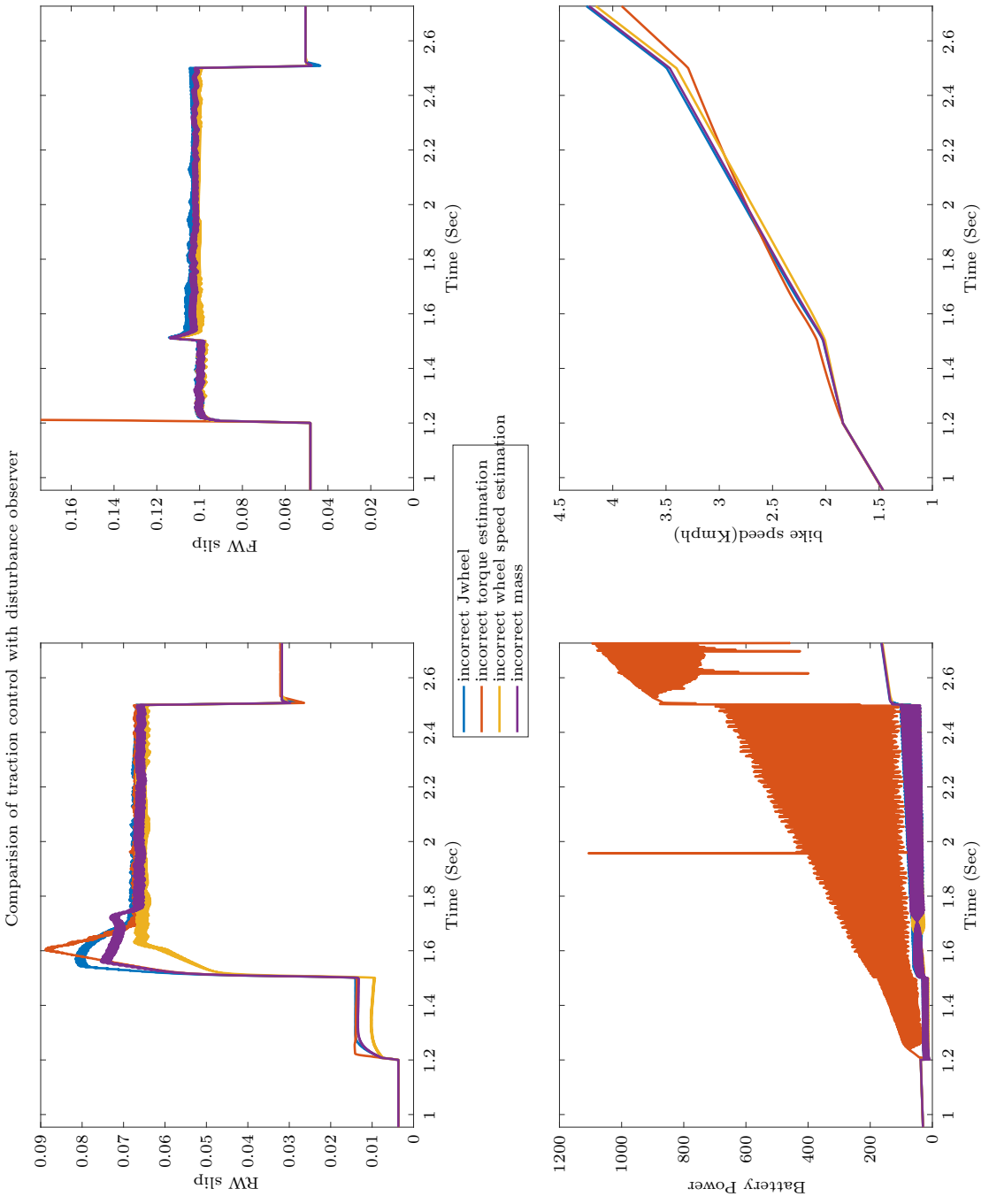

Figure 4-15: Effect of incorrect parameters with MTTE with disturbance observer

4.5 Summary

The longitudinal dynamic simulation of the entire e-bike model was performed with variations in inclinations, speeds and rider torque with the aim to compare the direct drive and internally geared motor. The result of these are presented in Table 5.1. The proposal of ABS to drive the wheels when a lock-up is sensed was simulated and the results supported the theory. It was seen that during these conditions, the power demanded was within the range the battery could supply. The ABS functionality was not achieved for all possible surface conditions like snow as the traction force was very small. This was due to the limits of motor torque, but it provided a pointer to motor sizing that should be consider for to ensure ABS operation for the target surfaces. The drawback of the method is the requirement that both wheels do not lock-up simultaneously.

Traction control using MTTE was presented and simulated for a range of surface conditions. The selection of filters was briefed and driving resistance estimator presented. The theory of MTTE was validated as the slips of both the wheels were well contained. The torque demand was seen to have very high frequency ripple but these variations did not effect the slip too much, specially at higher vehicle speeds. The effect of incorrect parameters to the model was tested and the major parameters that effect the performance were found to be incorrect vehicle mass and wheel torque estimation. The latter was the reason, the same theory could not be applied to be used during ABS as the braking torque was not measured. To overcome these issues, a modification of the theory to introduce a closed loop disturbance observer was tested. The immunity towards incorrect parameters was greatly improved. The same was tested incorporating tyre compliance and the performance remained unchanged.

Chapter 5

System Design

With the understanding of our e-bike and simulation tools at our disposal, we analyze the best sub-systems for our application. They include all the electrical sub-systems including batteries, controller, motors and other auxiliary components line the accelerometer and datalogger.

5.1 Motor Selection

For the selection of hub-motors, we evaluate the performance of direct drive and internally geared motor. Each one have their advantages that might make one suitable over the other. To get some knowledge about their relative performances, we use a general simulation model of the bicycle given in [4].

The major parameters that determine the machine size are.

- Torque.
- Electric Loading (A).
- Magnetic loading (B).
- Copper current density (J).

Since the values of A and J for the motors are not directly available, they are chosen in such a way as indicated in Appendix A to obtain realist sizes of machines

available for use. These are indicated in the table 5.1 along with the reference for each type.

5.1.1 Longitudinal Dynamics

Bike parameters In order to have accurate simulation results, we estimate the losses arising due to aerodynamic drag and rolling resistance. The mass, rider position, etc contribute in this regard. The tool to obtain these loss parameters for a typical MTB used was [36] given by Figure 5-1.

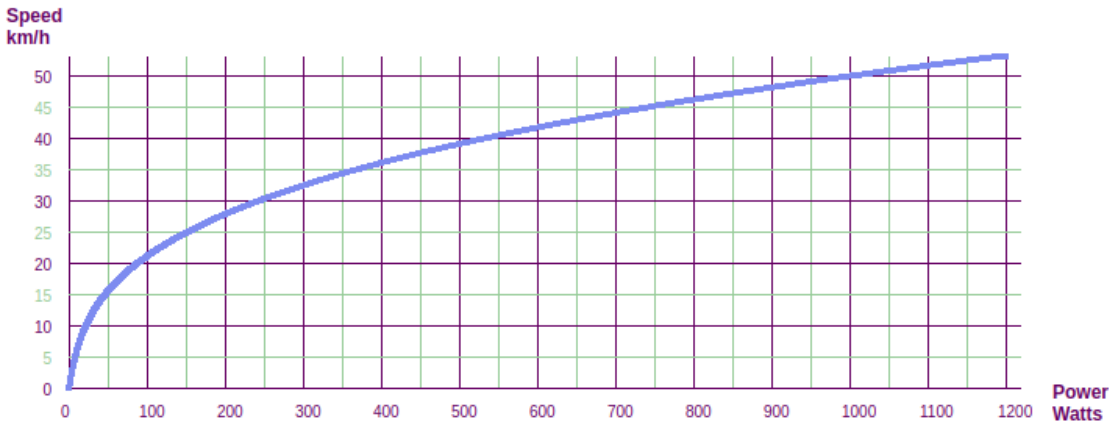

Figure 5-1: Rider Power vs Speed for our e-bike with estimated physical parameters

We use simulink to analyze the longitudinal dynamics of the e-bike. The electrical sub-system containing the motor, battery and the control logic are modeled. Simscape is used to model the mechanical components of the e-bike. They are interfaced with each other and tested for various conditions of inclination, which determines the rider torque. Both acceleration and braking are simulated to cover the areas of operation. The common parameters and results for each motor from simulations are in Table 5.1.

Motor Comparision Important simulation results are presented in Figure 5-2a, 5-2b and 5-3.

Parameter	Direct-drive	Geared
Rated Power (W)	400	400
Active axial length (mm)	70	50
Current density (J) (A/m2)	$2x10^6$	$0.7x10^6$
Electric loading (A)(KA/m)	$6x10^6$	$1.8x10^6$
Internal Diameter (mm)	88.6174	37.6937
External Diameter (mm)	139.9816	80.0525
Mass of stator (Kg)	3.7838	1.3212
Mass of rotor (Kg)	2.2894	1.3139
Moment of rotor (kg m2)	0.011	0.0016
Total mass of e-bike (Kg)	122	115
Trated (Nm)	16.836	1.536
Gear ratio	1	11 @ 97% efficiency
Wr rated (rad/sec)	23.75	261
Consumption(whr/km)	**6.303**	**6.397**
Consumption (whr)	**0.02974**	**0.02952**
Distance covered (m)	47.18	46.09
Actual model reference	Nine Continent Rear Hub	Bafang FM320.250

Table 5.1: Analytical comparison of hub-motors and respective results

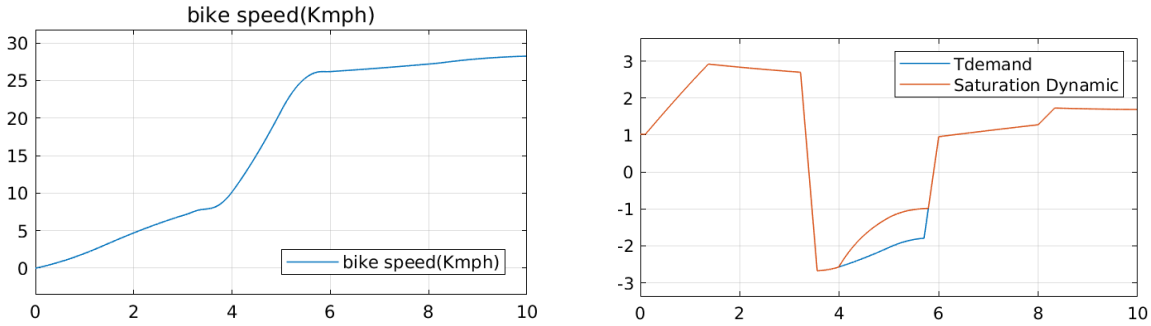

(a) e-bike speed

(b) Torque demand and Torque obtained with regen constraint for internally geared motor

Figure 5-2: Bike speed and Torque demand

Results verification To test the validity of the results, we compare our simulation results with existing tools for e-bike component sizing from [7]. The same parameters of the bike and motors are used. The results here indicate insignificant differences in both the motor types. Though the direct drive motor is more efficient, the loads are

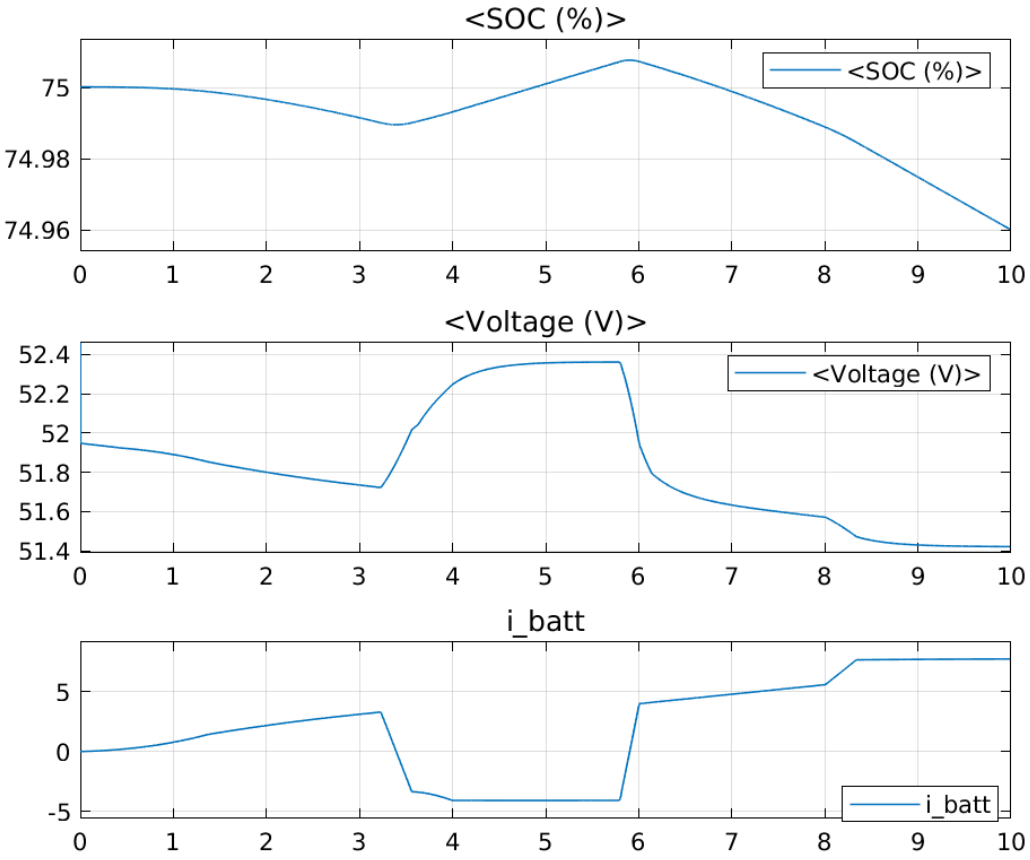

Figure 5-3: Front top to bottom: SOC, Battery voltage, Battery current simulation of e-bike. It can be the logic to limit current while recharging works and it limited to 5A

higher due to greater weight of the system. This is in agreement with our simulations.

We see that even with differences in the physical parameters of the two motors, the relative difference in performance between them is less than 1%.

5.1.2 Lateral dynamics

The importance and effect of lateral dynamics is highlighted in previous chapters. We use this understanding to compare the differences with each motor type.

Steering dynamics

Hub type	**bike hub**	**geared motor**	**direct drive**
$J_{steer}(Nm^2)$	0.0007	0.0056	0.0227
J_{steer} $wheel + tyre(Nm^2)$	0.19	0.19	0.19
J_{steer} $total(Nm^2)$	0.1907	0.1956	0.2127

Table 5.2: Effect of hub inertia on steering from (3.13)

low speed dynamics We see that the direct-drive motor has the greatest inertia which would effect the dynamic performance the most. However, it is about 10% of the inertia of a regular hub though the wheel is four times as heavy as the mass of the wheel away from the hub predominates.

Hub type	**direct drive**	**geared motor**
J_{rotor}	0.0057	0.0007204
Rotor J*ω @ 30 Kmph	0.1251	0.1749
Wheel J*ω @ 30 Kmph	1.3236	1.3236
Total J*ω @ 30 Kmph	1.4487	1.4995

Table 5.3: Gyroscopic effect of motor on steering from (3.14)

High speed dynamics As the wheel speed increases, the gyroscopic effect is greater. This effect is more pronounced for the internally geared motor as it spins at higher speed compared to the direct drive.

We see that the direct drive motor effects riding dynamics at low speeds and the geared motor at high speeds. Thus, this trade-off has to be considered while selecting the motor.

Effect of Yaw From (3.15) the increase in the moment requires greater roll reducing the maneuverability, more so for the geared hub.

Effect of Roll From (3.18) This moment aids in the roll of the bike helping the rider to enter and exit rolls faster. This effect unlike the other gyroscopic effects is beneficial to the maneuverability.

5.2 Motor controller

We would like to have an accurate control over the torque to have good performance of the Traction control system. Thus, vector control is chosen. Vector control is a well understood concept and there are a number of possible solutions for implementation. The requirements for this implementation were-

- Max DC Voltage - 52 V
- Max current - 30 A
- Ease of implementation of user desired control logic
- Interfacing with other sensors via various serial communication protocols

With these requirements, the TI LAUNCHXL-f280049C was choosen [37]. TI BOOSTXL-DRV8320RS power stage was used for the inverter system [38]. All safety functions like over current, over voltage, switch failure protection and sensing are implemented in the DRV8320RS which communicates with f280049 m/c via SPI.

5.3 Battery

The battery used is a production version from an existing e-bike. It is a 36V, 11.4 Ah capacity battery pack with serial interface via CAN, but was not employed for the project.

5.4 Inertial measurement unit (IMU)

An IMU is required to know the physical orientations of the bike in terms of roll, pitch, etc. These parameters help in achieving the optimum control of the bike under

various conditions as explained later. The sparkfun 9DoF sensor board [39] employing a LSM9DS1 IMU is used. It consists of 3-axis accelerometers, 3-axis gyroscope and a 3-axis magnetometer. The communication can be done via SPI or i^2c according the datasheet[40].

An IMU is a combination of accelerometers and gyroscopes to know the orientation of a body. Such a device can provide the information and is used in inertial navigation of ships and aircrafts. However, these are very expensive, thus, the MEMS sensors are used for low-cost applications. MEMS IMU are not as accurate and suffer for noise. Since most dynamics are obtained by integrating IMU outputs, the results are very susceptible to noise and drifts. From [41] and [42] we get (5.1-5.4).

$$a_x = \ddot{x} + 2V_y\omega_z + b_x + g\sin(\theta) + w_{acc_x} \tag{5.1}$$

$$a_y = \ddot{y} + 2V_x\omega_z + b_y + g\sin(\phi) + w_{acc_y} \tag{5.2}$$

$$a_z = \ddot{z} + g\cos(\theta) + b_z + w_{acc_z} \tag{5.3}$$

$$g_{x,y,z} = \omega_{x,y,z_{true}} + b_r + v_{gyro} \tag{5.4}$$

Where $a_{x,y,z}$ are the measured acceleration, $\ddot{x},\ \ddot{y}\ and\ \ddot{z}$ is the true acceleration in the vehicles coordinate system, $b_{x,y,z}$ is the bias of the sensors, $\omega_{acc_{x,y,z}}$ is white noise and ω_z is the yaw-rate, ω_y is the roll-rate, ω_x is the pitch rate. $g_{x,y,z}$ is the measured angular-rate $\omega_{x,y,z}$ is the true angular-rate, and b_r is the bias, and v_{gyro} is zero mean white noise.

From the above set of equations, it is clear that the accelerometers do not measure the linear accelerations but also the gravitational accelerations due to yaw, pitch and roll. These components along with the noise have to removed to obtain the true accelerations. The gyroscopes measure only rotational speeds but have to be integrated to obtain orientation. Since, the acclerometer measures the Euler angles $(\theta,\ \phi,\ \beta)$ which are the results of gyro integration, both these data can be used to complement each other. This is called sensor fusion and the most commonly used method is with Kalman filter. However, Kalman filters demand huge memory and

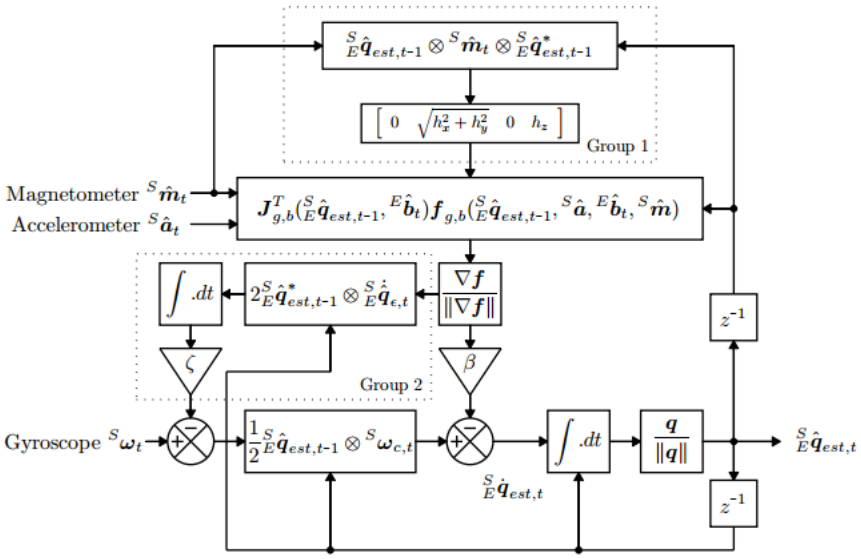

Figure 5-4: Block diagram of Madgwick AHRS algorithm

computation power in embedded systems. Thus, an alternative approach using the complementary filter is selected [43]. The filter employs the references to correct the errors from other sensor systems and ensures convergence. An IMU can provide orientation w.r.t its body co-ordinates. However, as the body moves, its position on the earth changes which is required as the output from this system provide the vehicle speed is known. Tracking this is difficult as we require a reference for the position of the body. To track the body, sensor fusion employs GPS data for localization [41]. Other senors like a magnetometer that can provide localization but have problems with interference with stray magnetic fields. Such a combination of accelerometers, gyroscopes and magnetometers is known as AHRS (Attitude and Heading Reference Systems) or MARG (Magnetic, Angular Rate, and Gravity) sensor array. In this application, the latter was used because of its lower cost. The AHRS algorithm proposed by Madgwick[44] was used. The algorithm employs the complementary filter proposed by Mahony [43]. The algorithm works at sampling rates as low as 100 Hz.

5.5 DataLogger

To analyze the data from the e-bike, openLog from Sparkfun was used[45]. It contains an onboard Atmega processor that communicates via UART with the host and writes a micro-SD card via SPI. It can log upto speed of 600,000 bps with support to memory upto 32GB. The openlog logs binary data and thus does not differentiate between floating numbers, text, integers, etc. All data is stored in a text file which requires post processing. Each floating point number in the TI C2000 family (which is the controller selected) is saved as a 32 bit binary number according to IEEE754. While the characters are transmitted as their ASCII equivalent. This combination of mixed data types is addressed by defining suitable limiters for each set of datatypes represented in blue in Figure 5-5. The general format of data transmission is as followed.

Float Data 1, 2, 3.....	0xFFFFFFFF	Character1,2.....	0x2c2c2c2c
Float Data 1, 2, 3.....	0xFFFFFFFF	Character1,2.....	0x2c2c2c2c

Figure 5-5: Data transmission packet format from controller to Openlog

The delimiters are choosen so as to provide dependable points to separate the data streams. The float equivalent of 0xFFFFFFF is NaN which is not a valid float number transmitted by the controller. These delimiters are used to separate the float data from character data and saved as a csv file using python.

The rate of data logging is 50 Hz. The baud rate of transmission if 230,400 bps choosen such that the entire data transmission buffer is completed before the next one starts.

5.6 Torque Sensor

The torque sensors as described in Chapter 2 measures the torque. The first torque sensor used was from NCTE. It was a left crank torque sensor. It required a 12 V supply to operate with a current of 20-30 mA. This information was not available in

the data sheet and a 12V cell was used which was unable to drive the sensor causing it to malfunction which destroyed the sensor. The next sensor employed was the sempu torque sensor [46] . This differs from NCTE as it measures the force on the spocket instead of the torque enabling sensing of forces from both sides of the pedals.

5.7 System Topology

The general topology of the electrical systems and the peripherals are indicated in Figure 5-6. It consists of integration of all sub-systems used in the prototype. Though the aim is to evaluate an S-pedelec, due to constrains in time, the decision to use a prototype of a pedelec was taken.

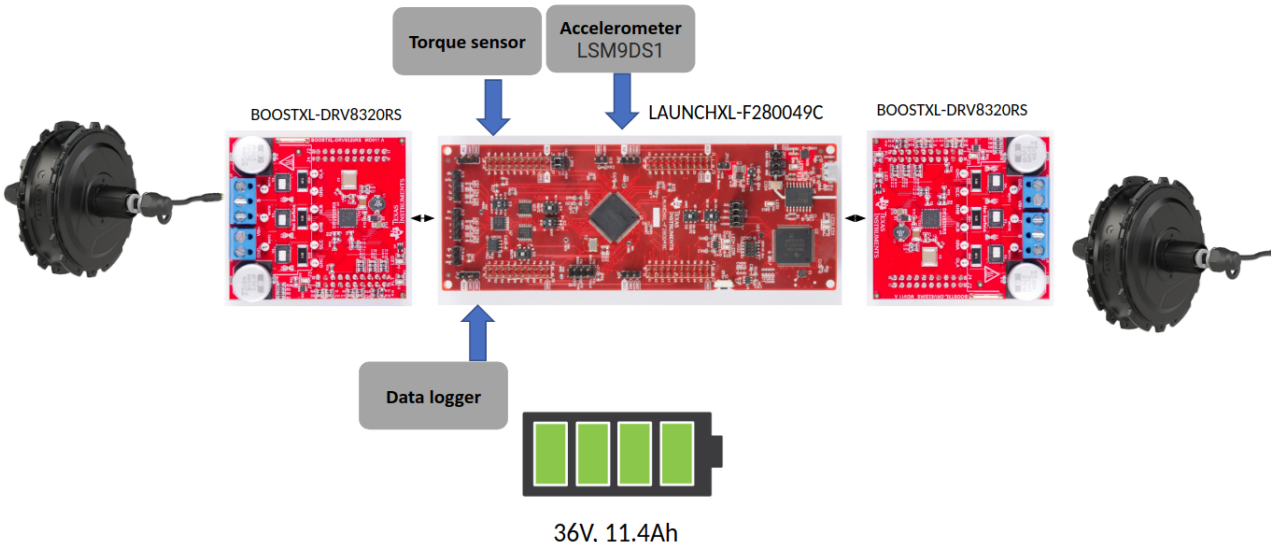

Figure 5-6: System topology of e-bike

5.8 Summary

The table 5.4 shows the effect different motors due to wheel inertia for various motions.

In reality, these effects are coupled and depending on the dynamics have a compounded effect on the maneuverability of the bike.

Also, the difference in the efficiencies between the two are not significant. Hence,

Table 5.4: Gyroscopic effect of motors on bike dynamics

Parameters	**direct drive**	**geared motor**
Low speed steering	- -	-
High speed steering	-	- -
Constant Yaw	-	- -
Constant Roll	+	++

the basis of choosing the motors would be primarily based on riding dynamics and ABS functioning requirements as explained.

Due the short time for the implementation, motors and battery for an s-pedelec system could not be procured and instead the decision to use existing motors which form a part of Bianchi's current range was taken. The final motors selected were-

- Front motor - Bafang FMG320.250V, [47]
- Rear motor - Bafang, [48]

Both motors come with internal freewheels which were removed to have the provision of regeneration.

Chapter 6

Implementation

The Chapter describes the sequence and the process of the embedded implementation of the functions described in the previous chapters on a prototype. The prototype is described and the control algorithm for it is presented. Results of the tests are analyzed.

6.1 Testing Of Vector Control

A test bed for dual control of the motors as shown in Figure 6-1 was employed. It consisted of four rollers connected through a common shaft. The normal load on the motors could be changed with the addition/ removal of weights. The set-up was rated for 25 Kmph. The motors were mounted as shown and tested in torque and speed control mode and the switching between the two modes. The motors were loaded as they would to test their thermal performance and ensure operation. This ensured that the thermal limits of the Power electronic stage was not reached. The results are shown in Appendix B-1, B-2, B-3. Front motor was used in speed control and the rear in torque control to split the torque between the two. Due to the set-up, the tyres lose contact and begin to slip causing the fluctuation in speed.

Figure 6-1: Test setup of dual motor control

6.2 E-bike control algorithm

Due to number of functions to be performed, and the priority given to motor control, the remaining functions are implemented by the use of flags. The general control flow of the working is indicated in the flowchart Figure 6-2

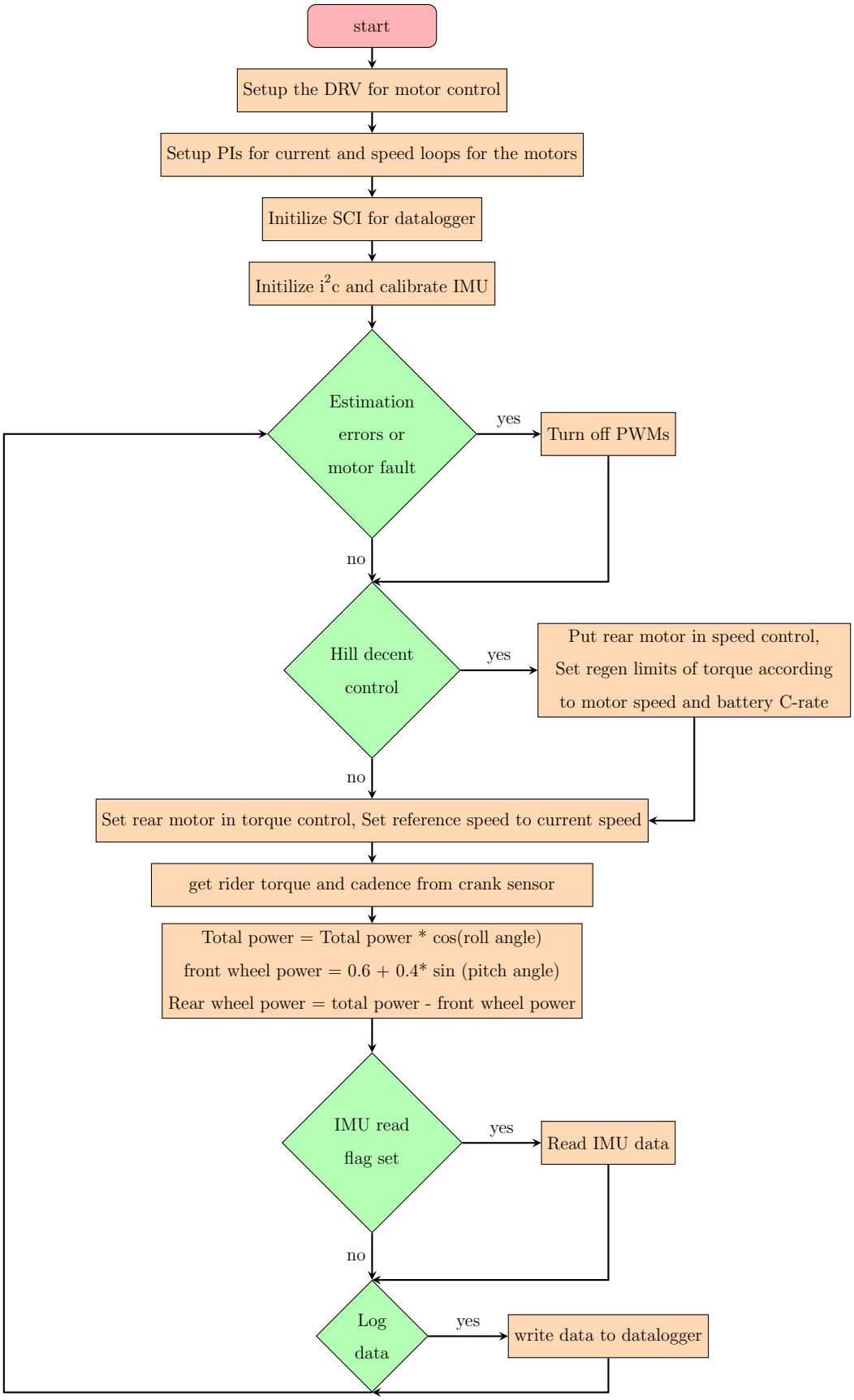

Figure 6-2: Flow chart of control

Embedded programming was done in Code Composer studio (CCS), based on Eclipse IDE. All functions were implemented in C and distributed in C-files. GIT was used for version control. A screenshot of an instant of the IDE is shown in Figure 6-3.

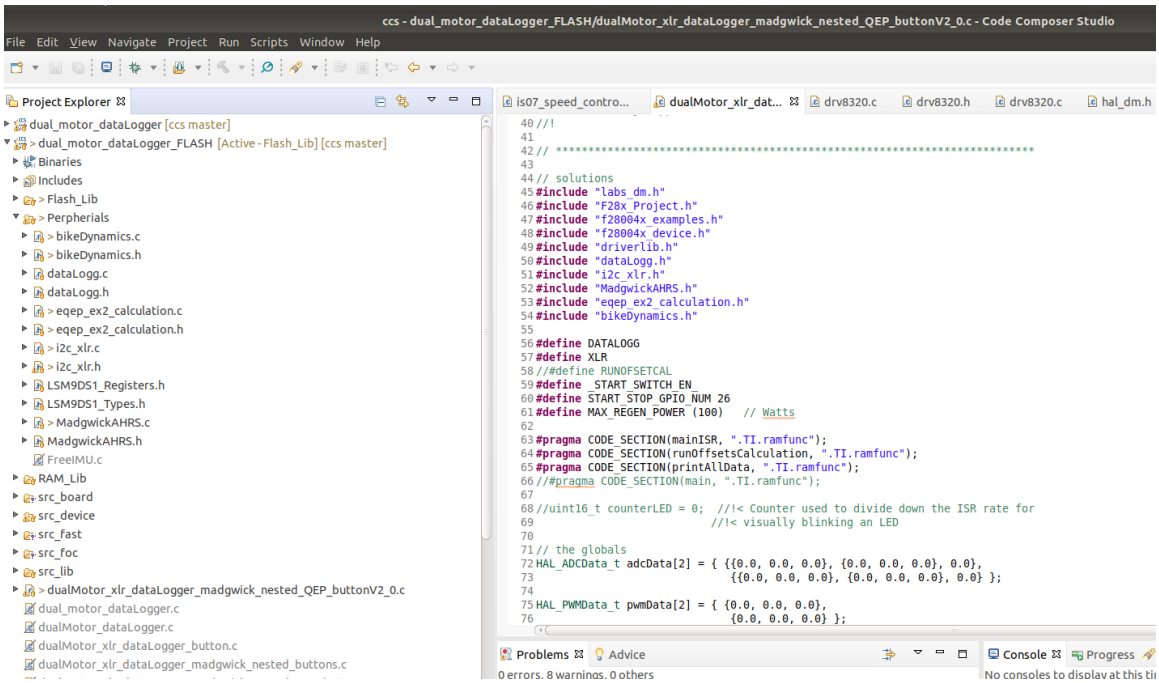

Figure 6-3: One instant of the CCS IDE

6.3 Field test

The prototype bike is shown in Figure 6-4. The frame used for the prototype was of a commuter bike as it could house both the motors. The control and Power electronics were housed in a 3D printed case shown in Figure 6-4b. The bike was tested within the campus for the various functions. The duration of run was 5 min. A button was used to power off the motors in case of emergency. The assist was 50 % to verify the system behavior. The data was stored in a micro-SD card and extracted using a python script to yield the CSV file. Some parameters are shown in Appendix B-7.

Due to the constraint of time and the limited variation in terrains in the campus, not all the functionalities could be tested. The results of the different functions are

(a) Prototype bike

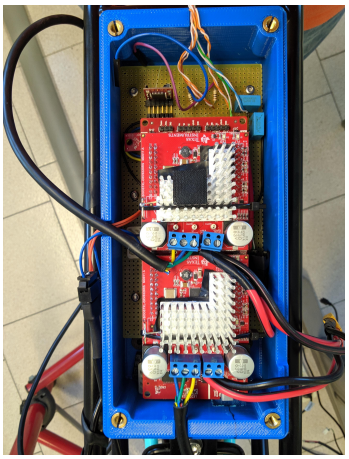

(b) Controller

Figure 6-4: Prototype and Controller electronics

presented.

6.3.1 ABS

The logic mentioned in 4.3.1 was used. With the bike ridden on tarmac, as noticed in simulations, no amount braking torque was able to lockup the front wheels and only the rear wheels lockup was achieved. The activation of the motors was done using a button on the handle bar. The rear wheel lockup was not completely eliminated but the duration of the lock was reduced compared to the attempts that preceded it in Figure 6-5. On closer inspection, the positive torque demanded does not occur throughout the lockup phase of the rear wheels indicating that it could be due to the relative lower processing rate of 10ms.

The concept is validated but a robust implementation could throw better light on the performance.

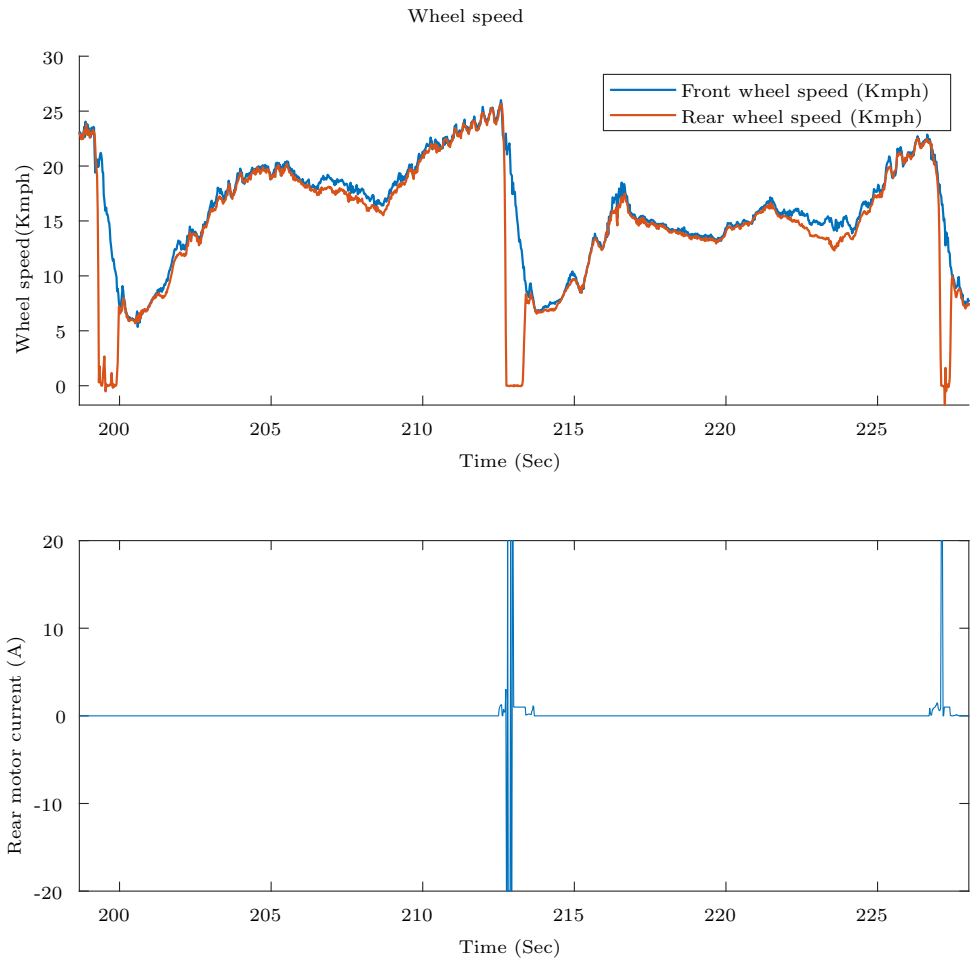

Figure 6-5: ABS effect on prototype. The difference in the front and rear wheel is seen and a noticeable reduction in lockup of rear wheel is achieved.

6.3.2 Battery Current estimation

It is required to limit the battery current during regen depending on the SOC to prevent damage to cells. This needs accurate battery current measurement which can be done using a low side current shunt. However, since we control the PWMs to the motors, we can use the knowledge of the duty cycles in each leg to estimate the battery current eliminating the need for an additional sensor. From the ePWM module of [37].

$$BatteryCurrent = \frac{\sum_{n=a,b,c}[TBPRD - CMPA_n] \cdot I_n}{TBPRD} \tag{6.1}$$

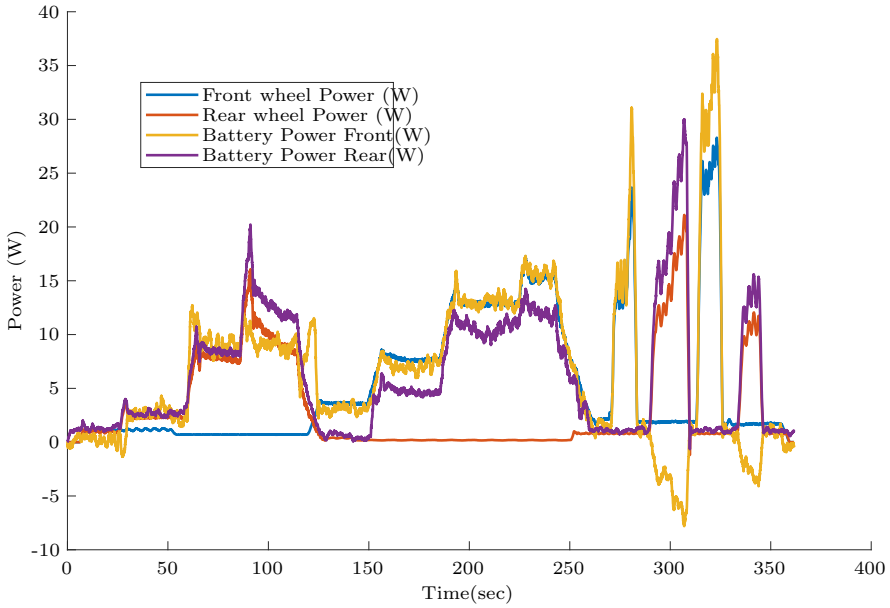

Figure 6-6: Comparison of calculated Battery and actual motor powers

The respective powers follow each other quite well expect when the actual power is zero. This concept requires further validation by comparison with a physical current sensor to judge its feasibility.

6.3.3 Decent Control

This function is used to hold the speed of the bike during descents. It is done by putting the rear wheels in speed control and applying only -ve torques to prevent assist from any means except due to pedaling. The lower limit to the output of the speed PI is set such that the battery current is limited. This is done indirectly

$$I_{bat}limit = \frac{\frac{P_{max}}{2\pi\omega_e}}{K_t} \tag{6.2}$$

When the function is active using a button on the handle bar indicated by '0', the motor does not provide any assist while providing only braking torque. The influence of this on the range and holding speed are yet to assessed as the campus lacked any significant descents. In case of accurate battery current estimation/ measurement,

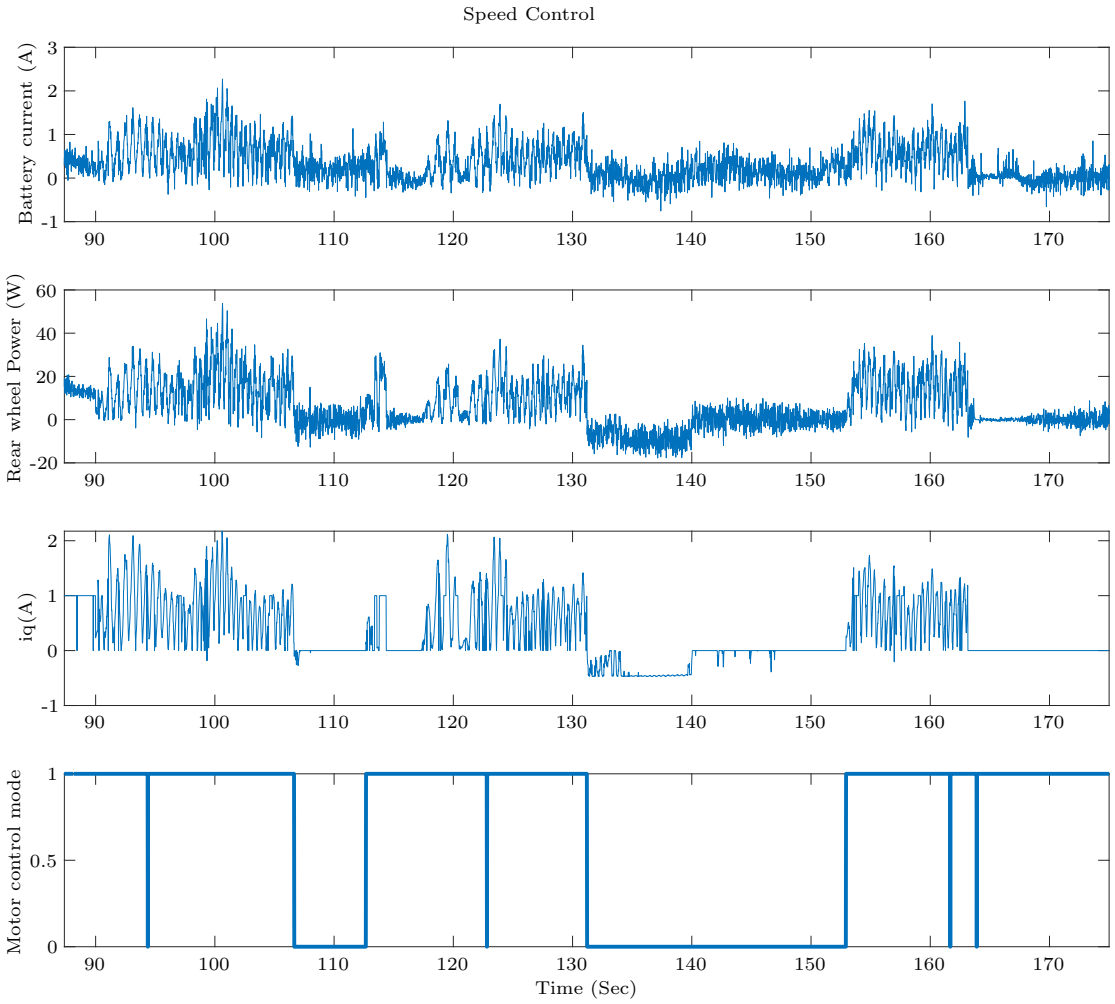

Figure 6-7: operation during speed control. From top to bottom: Battery current; Rear wheel power; q-axis current demanded by the control algorithm; rear motor control mode indicated by '0'

the speed PI can be modified to generate battery current as the output of the speed PI giving better control over battery current.

6.3.4 Higher Power assists

To test the performance of the bike, the assist level was increased to 400 %. This resulted in the trip zones of the PWM modules activating, which switched off the PWM to the motors. This issue was not fixed due to time and thus, the performance of the system could not be accessed.

6.4 Summary

The procedure and test setup to check the motor control and verify its operation was presented. The prototype was highlighted and the flow of the e-bike control was provided. Brief tests with the prototype on campus were performed with the aim test the functionalities as tested in the simulations. The general results were positive as the bike behaved as it should. The ABS function was tested, thought, there is scope for improvement, the theory was validated. However, more complete tests for higher power assists were not performed and the range of such a system, the influence of regen braking were not tested extensively.

The idea to eliminate the use of a sensor to measure battery current was proposed and its effect demonstrated. Though, it works to a certain extent, this required further validation.

Power Electronics And Control. The vector control for the motor was vital for the implementation. Therefore, it was decided to use an off the shelf solution to speed up the implementation. Though, a number of options were considered, TI's instaspin solution provided the flexibility needed. The heat sinks for the power electronics were sized to allow proper operation and grounded to reduce EMI.

Other Peripherials. The IMU sensor fusion was very important; as only using the accelerometer gave incorrect values of orientation when the body was in motion, to an extent that those values were not useful in any way. The implementation was using Madgwick's open source algorithm. Though theoretically possible, the vehicle speed was unable to be obtained with the AHRS algorithm. It was observed that the maximum lean angle was around 20°, where the rider stops pedeling altogether. Therefore, the use of the IMU to reduced torque assist with lean was not justified. Atleast, not with the geometry of the prototype bike.

The datalogging from the openlog took a lot of testing to get to the right selection of separators to filter out floating numbers and characters. This was due to the fact that floating point numbers could take any value which could be a valid ASCII

character making separation using just one character in-feasible.

Due to the number of sensors interfaced, majority of the m/c modules were used. A detailed pin analysis had to be performed to ensure that all communication channels and sensors were usable simultaneously.

Though ABS function was tested, the traction control using MTTE could not be simulated. But the simulations performed considering the constrains give us a good idea about its performance.

Chapter 7

Conclusion And Future Works

The previous chapters talk about the parameters considered and describes the details of the design and implementation of the e-bike drive train. A number of design goals were set which required in-depth inspection in inter-disciplinary areas ranging from bike dynamics to electrical systems and architecture to control methodologies. The implementation required good understanding of the hardware and the interface between each other to select the best solution for the prototype. Considerable amount of time was spent on embedded programming in C and understating the micro-controller, every peripheral used and their limitations.

7.1 Conclusions

- The of advantage dual motors is the fast and individual control of torque on each wheel. Vector control helps in achieving accurate torque and good dynamic response.

- Use of a 48 V battery over 36 V battery with a boost converter is preferred as the it simplifies the design and reduces looses but the motor's speed is reduced at low SOCs which may be desirable.

- LFP cells are preferred for the battery pack as they allow for a wider range of speeds for regenerative braking. However, the expense of weight is to be

considered for bike handling.

- The choice between an internally geared motor with lower weight and a direct drive motor with higher efficiency is insignificant in terms of range as the geared hub is less efficient compensating for its reduced weight. The decision between the two depends on how each effects the dynamics of the bike. Specially the front wheels, where a motor with lower inertia, i.e direct drive would be preferable.

- The sensor-less vector control algorithm employed for the motors highlighted some problems due the fact that motor speeds was measured using currents which required the presence of PWM signals. This data was lost when a fault occurred which resulted in jerks.

- The operation of motors during higher vehicle speeds should be considered as the motors spin with the same speeds as the wheels. At low SOC or higher speeds the back-emf of the motor would be high requiring the need for Field weakening or disconnecting the battery terminals from the inverter.

- The IMU AHRS algorithm provided accurate orientation of the bike but the linear speeds from the same was not obtained. This was not problem for the TCS but was for ABS.

- Due to no knowledge of the e-bike speed, the ABS logic used involved comparing the two wheel speeds with each other and providing additional torque when one would begin to slip. This required atleast one wheel to keep traction.

- The ABS logic was tested practically and the results were positive, but higher control rates would improve performance. The ABS worked for most surface conditions except very low friction surfaces like snow due to limits in motor torque. This requirement of desired performance for various conditions is a parameter that can be used for machine sizing.

- The MTTE algorithm for traction control was briefed and simulated for a number of road conditions. The performance was good but suffered when the pa-

rameters were incorrect.

- To overcome the problems associated with incorrect parameters, the closed loop observed was introduced and a significant improvement in performance was noticed. However, due to constraint in time, this was not tested on the prototype.

- A prototype was built with off the shelf components to test the various functions of the bike. The prototype was a pedelec and not an S-pedelec due to limited time available for the procurement of the components. All functions expect TCS were tested and partly verified.

- The performance of the e-bike at high assist levels were not conducted due to issues with the gate driver that underwent protection at high assist levels due to activation of trip zones. Due to limited time and variations in terrains, the dynamic handling of the bike could not be evaluated.

- Smaller wheels can be considered as it results in greater wheel speed for the same vehicle speed. This results is reducing of motor torque which reduces size and weight. Roll-over of the front wheels is also improved as it is driven.

7.2 Future Work

A number of improvements and additional work can be carried out in the future.

- The general control structure of the e-bike was tested with positive results. However, its performance at high power assist levels should be validated and obtain accurate estimation of range and the effect of regen braking.

- The dynamic performance of the e-bike is to validated in the right environments as the aim of the bike to be used for recreational purpose.

- A better ABS system using non-linear control techniques as mentioned in [32] should be explored for better performance.

- The TCS system using MTTE is to be tested and validated on the bike. This may required modeling additional dynamics from the chain drive which was omitted in the simulations.

- An alternative algorithm for the IMU can be considered that can yield vehicle speed which will be useful for ABS. Additionally, if GPS is employed, accurate positioning of the bike can be obtained that can provide the rider greater details of the usage of the bike.

- An S-pedelec prototype implementation can be done which would primarily require the selection of a front hub motor to reach such speeds which was not found during the time of research.

- The dynamic handling of the bike is to be tested to ensure it is pleasant to ride.

Appendix A

Motor Sizing

The two motors have different electrical and mechanical characteristics of mass, inertia, etc which are useful parameters for analysis. As the aim is to use existing design and not design new motor types, thus, we consider Surface PM (SPM) hub motors. The general sizing equations are provided-

$$A = H = \frac{JS_{all_s lots} * K_{fill}}{\pi D} \tag{A.1}$$

$$D = \sqrt{\frac{2\ Torque}{H\ B\ Kw_1\ \pi\ Lz}} \tag{A.2}$$

$$S_{all_{slots}} = K_{factor}\frac{\pi}{4}(D^2 - D_{bi}^2); K_{factor} = 0.6 \tag{A.3}$$

$$D_{bi} = \sqrt{D^2 - \frac{4S_{all_s lots}}{K\pi}} \tag{A.4}$$

$$\tau_p = \frac{\pi D}{2p} \tag{A.5}$$

$$\tau_s = \frac{\pi D}{Z} \tag{A.6}$$

$$W_t = \frac{B_{peak}\tau_s}{B_t} \tag{A.7}$$

$$W_{bi} = \frac{1}{2}\frac{B_{peak}\tau_p}{B_{bi}} \tag{A.8}$$

$$D_{in} = D_{bi} - 2W_{bi} \tag{A.9}$$

$$D_{airgap} = D + 2\ g;\ D_{ext} = D_{airgap} + 2 * L_m; \tag{A.10}$$

$$L_{ew} = 2.5\frac{D}{p};\ L_{tot} = L_z + L_{ew}; \tag{A.11}$$

$$N_{ph} = \frac{H\ \pi\ D}{2\ m\ I} \tag{A.12}$$

$$R_s = 2\ N_{ph}\ \rho\ \frac{L_{tot}}{S_{cu} * K_{fill}} \tag{A.13}$$

$$E_1 = 2\pi\frac{fs}{p}\ K_{w1}\ N_{ph}\ B\ D\ L_z \tag{A.14}$$

$$\lambda_{pm} = \frac{E_1\sqrt{2}}{\omega_e} \tag{A.15}$$

$$L_d = \sqrt{\frac{(\frac{V_{dc}\ 0.707}{\omega_e})^2 - \lambda_{pm}^2}{I\sqrt{2}}}; \tag{A.16}$$

Mass computation

$$m_{cu} = 8960 * S_{cu_all} * K_{fill} * L_z * 1.4; \tag{A.17}$$

$$m_{iron} = 7500(\frac{pi\ (D^2 - D_{in}^2)}{4} - S_{cu_all})Lz; \tag{A.18}$$

$$m_{stator_mech} = 0.1; m_{stator} = m_{cu} + m_{iron} + m_{stator_mech}; \tag{A.19}$$

$$m_{cu} = 8960 * S_{cu_all} * K_{fill} * L_z * 1.4; \tag{A.20}$$

$$m_{PM} = 7600 L_m\ K_a\ \pi D_{airgap}\ L_z \tag{A.21}$$

$$m_{jacket_horizontal} = 2800\pi(\frac{D_{ext}}{2} + w_{jacket})^2 - (\frac{D_{ext}}{2})^2\ 2\ L_z); w_{jacket} = 1e-3; \tag{A.22}$$

$$m_{jacket_vertical} = 2800\ 2\ \pi\ \frac{D_{ext}^2}{4})\ 1.1\ w_{jacket} \tag{A.23}$$

$$m_{jacket} = m_{jacket_horizontal} + m_{jacket_vertical} \tag{A.24}$$

$$m_{rotor} = m_{PM} + m_{jacket}; \tag{A.25}$$

$$J_{rotor} = m_{PM}\ (\frac{D_{airgap}}{2}^2 + (\frac{D_{airgap} + 2\ Lm}{2})^2) + m_{jacket}\ (\frac{D_{ext}}{2}^2 + (\frac{D_{ext}}{2} - w_{jacket})^2); \tag{A.26}$$

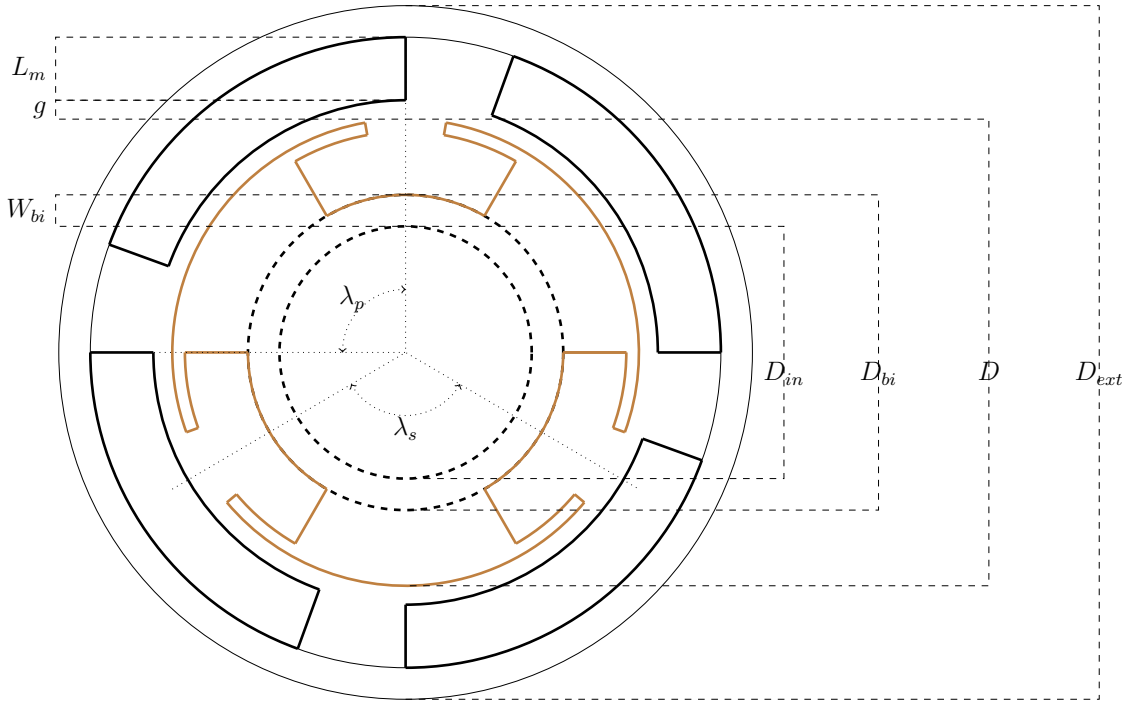

Figure A-1: Hub motor dimensions

Appendix B

Figures

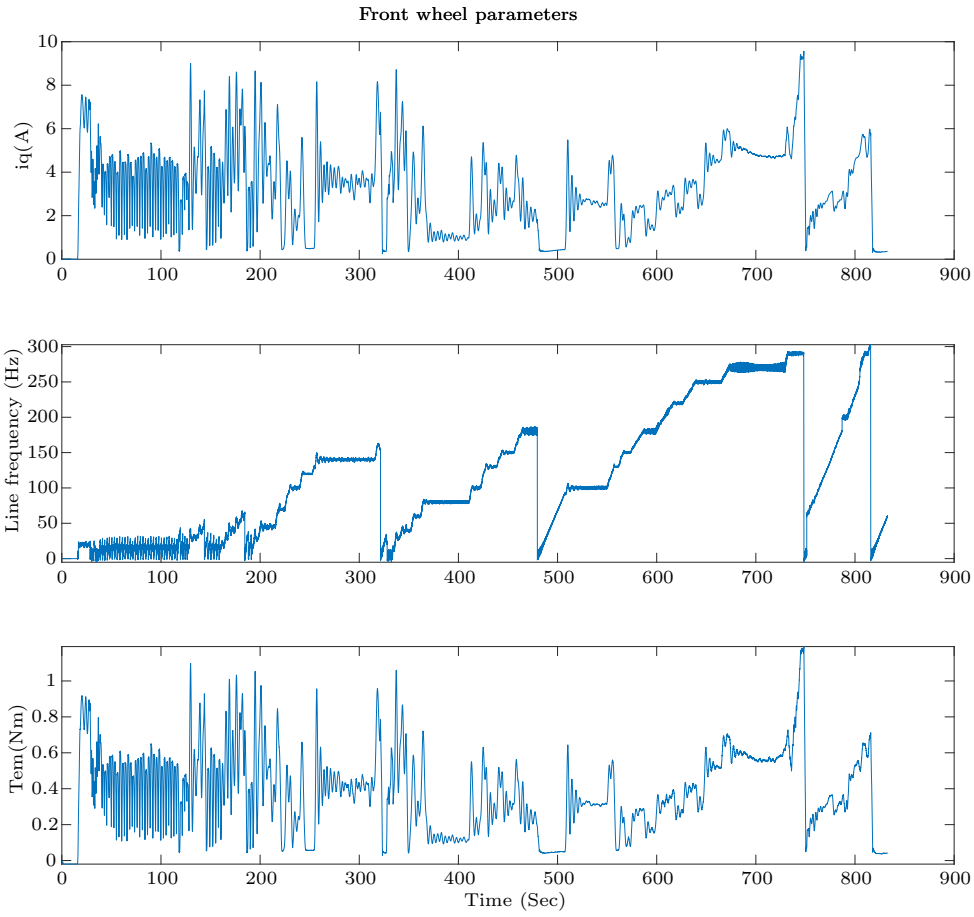

Figure B-1: Front motor parameters

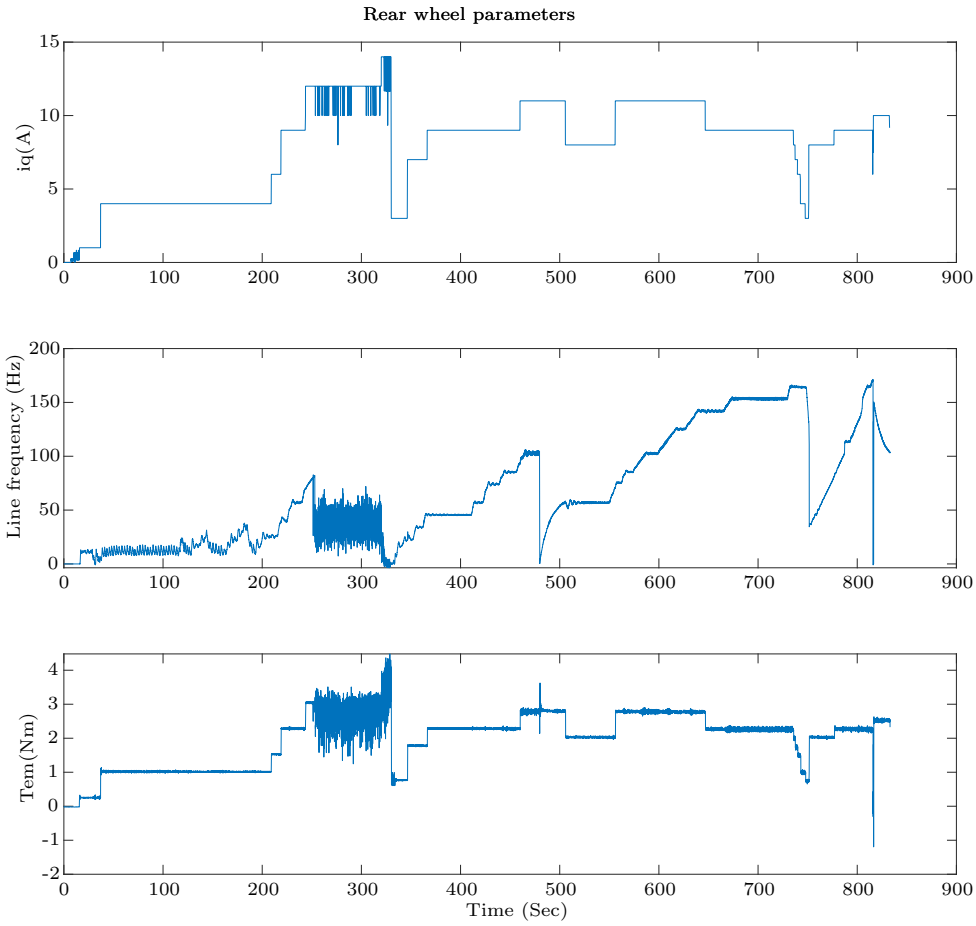

Figure B-2: Rear motor parameters

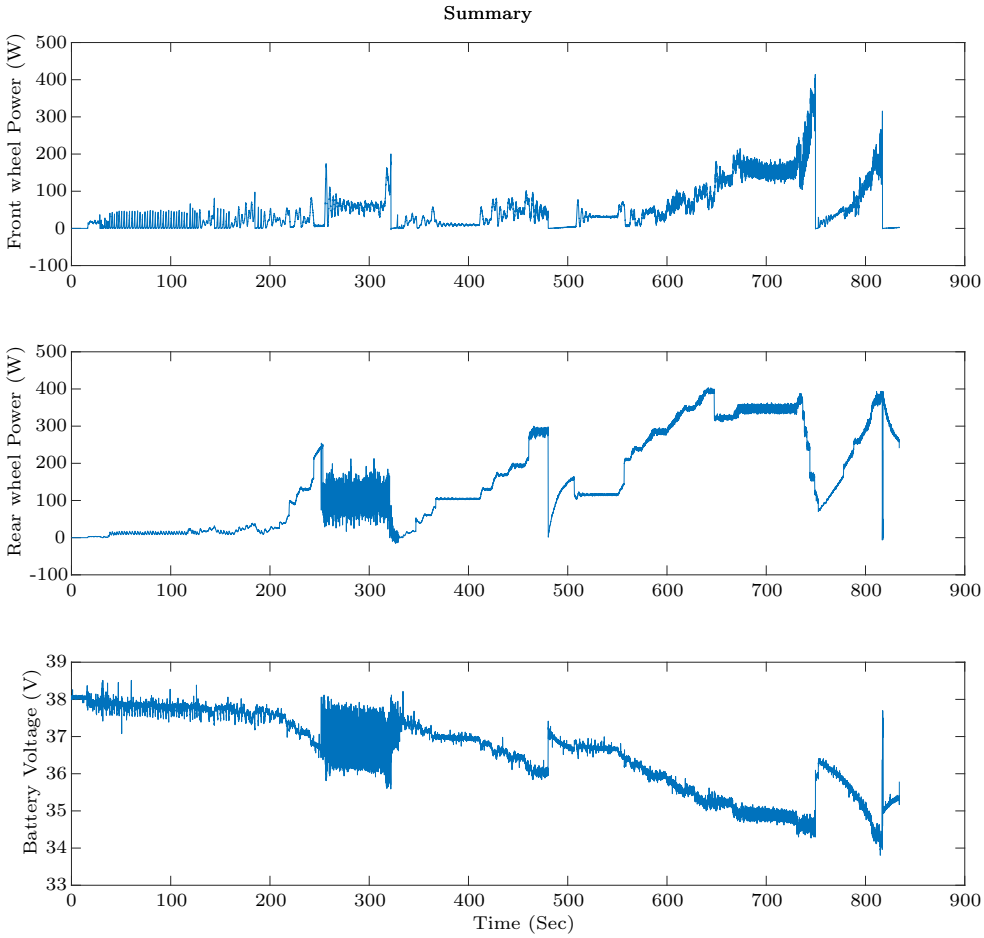

Figure B-3: Summary

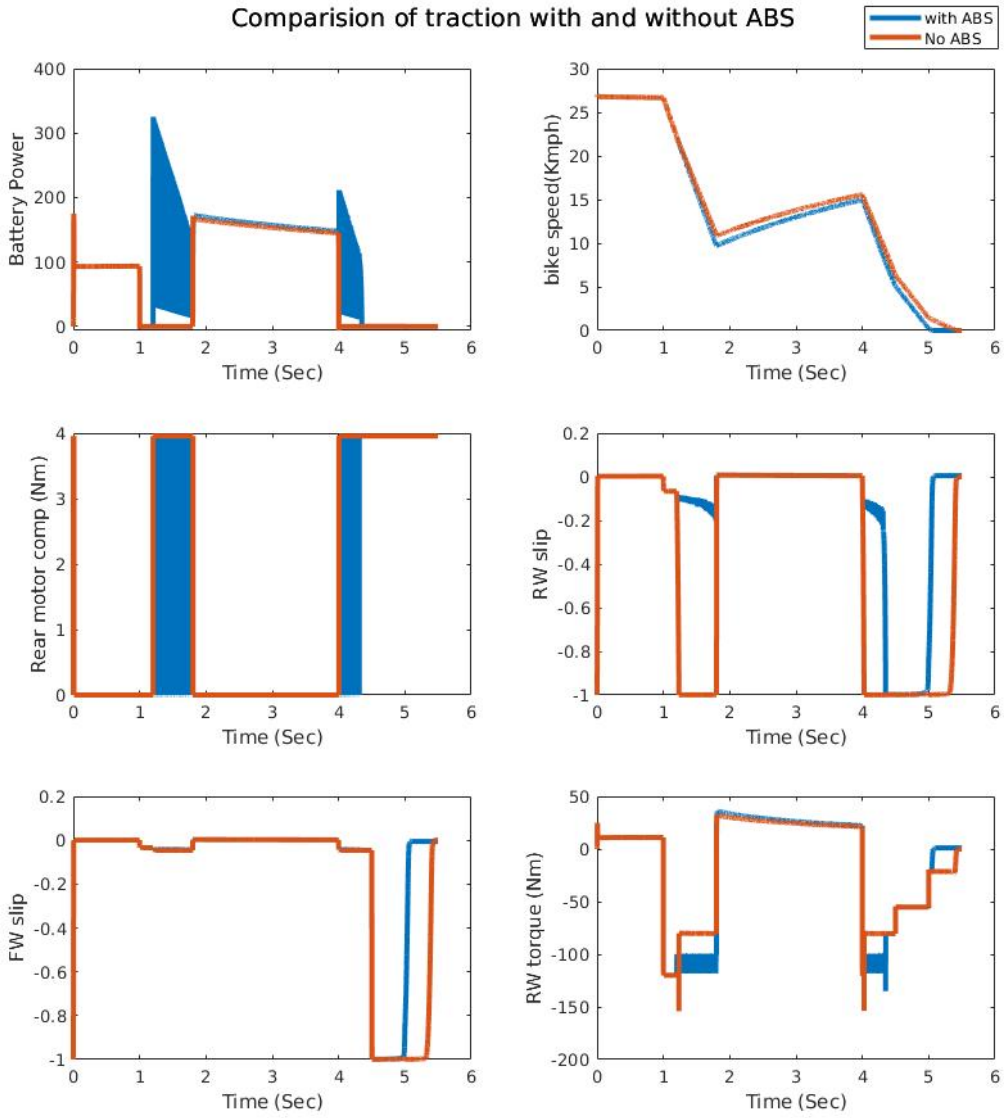

Figure B-4: Effect of ABS- rear lock up

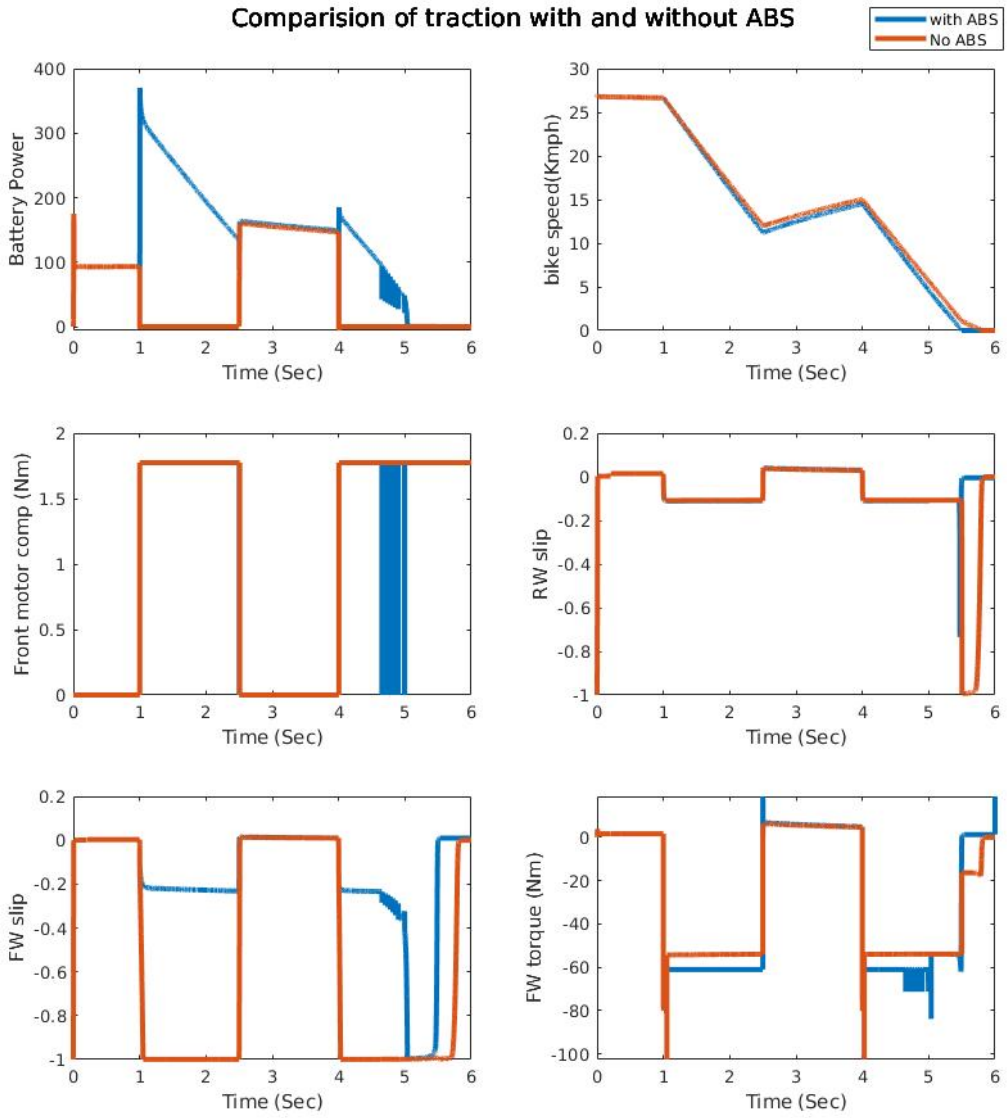

Figure B-5: Effect of ABS- Front lockup

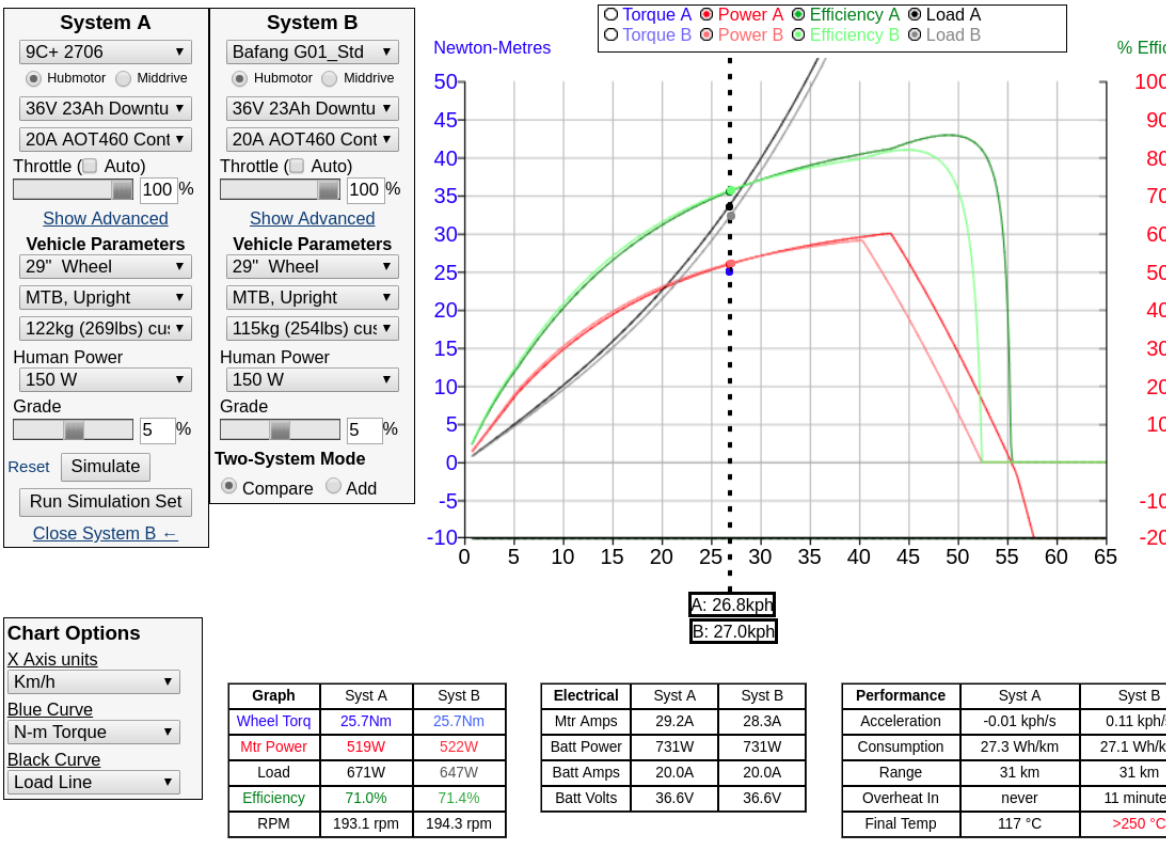

Graph	Syst A	Syst B
Wheel Torq	25.7Nm	25.7Nm
Mtr Power	519W	522W
Load	671W	647W
Efficiency	71.0%	71.4%
RPM	193.1 rpm	194.3 rpm

Electrical	Syst A	Syst B
Mtr Amps	29.2A	28.3A
Batt Power	731W	731W
Batt Amps	20.0A	20.0A
Batt Volts	36.6V	36.6V

Performance	Syst A	Syst B
Acceleration	-0.01 kph/s	0.11 kph/
Consumption	27.3 Wh/km	27.1 Wh/k
Range	31 km	31 km
Overheat In	never	11 minute
Final Temp	117 °C	>250 °C

Figure B-6: Motor comparison from [7]

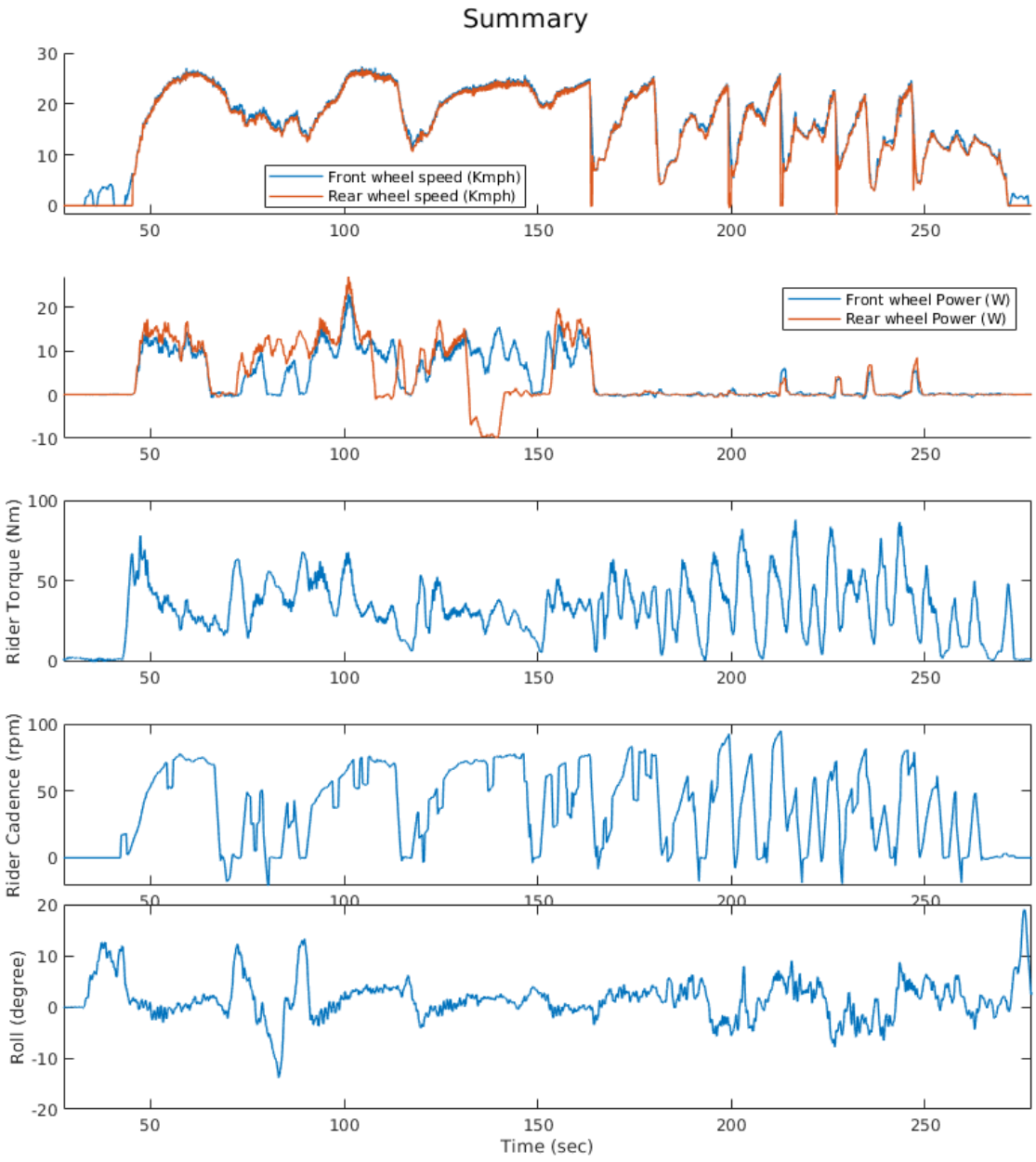

Figure B-7: From top to bottom: Front and rear linear wheel speeds; Front and reat power, rear power is greater than front wheel power; Rider torque at the cranks; Rider cadence; roll angle during the test run

Bibliography

[1] CIVITAS. Smart choices for cities, cycling in the city. *CIVITAS WIKI consortium*, page 28, 11 2016.

[2] Filip Wilczyński, Politechnika Gdańska, Patryk Strankowski, Jaroslaw Guzinski, Marcin Morawiec, Arkadiusz Lewicki, and Grzegorz Kostro. Five-phase induction motor drive operation during stator phase fault. 2017.

[3] V. Cossalter. *Motorcycle Dynamics*. Vittore Cossalter, 2006.

[4] K. J. Astrom, R. E. Klein, and A. Lennartsson. Bicycle dynamics and control: adapted bicycles for education and research. *IEEE Control Systems Magazine*, 25(4):26–47, Aug 2005.

[5] D. Yin, S. Oh, and Y. Hori. A novel traction control for ev based on maximum transmissible torque estimation. *IEEE Transactions on Industrial Electronics*, 56(6):2086–2094, June 2009.

[6] J. Hu, D. Yin, Y. Hori, and F. Hu. A new mtte methodology for electric vehicle traction control. In *2009 International Conference on Electrical Machines and Systems*, pages 1–6, Nov 2009.

[7] www.ebikes.ca. Motor simulator. `https://www.ebikes.ca/tools/simulator.html?motor=M2706&hp=150&motor_b=MG01_STD&hp_b=150&bopen=true&mass=122&mass_b=115&grade_b=5&grade=5&wheel_b=29i&wheel=29i`. [Comparision of motors].

[8] M. van den Bossche, T. (University of Antwerp) Macario R. Maes. J. (Ecorys), Vanelslander, and V. (University of Lisbon) Reis. Study on urban logistics. *The integrated perspective*, 12 2017.

[9] EUROPEAN BICYCLE MARKET. Industry and market profile. Technical report, Confederation of the European Bicycle Industry, 2017.

[10] Zane McDonald Jacob Mason, Lew Fulton. A global high shift cycling scenario:. *By the Institute for Transportation and Development Policy and the University of California, Davis*, 11 2015.

[11] Jorge León Emilio González, Dolores Herrero. Assessment of environmental impact, economic and societal competitiveness. *Promoting electrical bikes and scooters for delivery of goods and passenger transport in urban areas*, 12 2015.

[12] EN 15194:2017. Cycles - electrically power assisted cycles - epac bicycles. Technical report, CEN, 2017.

[13] Alexandre Santacreu. Cycling safety. *International transport forum, rountable 168*, 01 2018.

[14] Marco Dozza, Giulio Francesco Bianchi Piccinini, and Julia Werneke. Using naturalistic data to assess e-cyclist behavior. 2016.

[15] IEC 62133:2012. Secondary cells and batteries containing alkaline or other non-acid electrolytes - safety requirements for portable sealed secondary lithium cells, and for batteries made from them, for use in portable applications - part 2: Lithium systems. Technical report, IEC, 2012.

[16] Y. Li, L. Wang, C. Liao, Wu Lingfei, Li Junfeng, and Guo Yanjie. Effects of temperature on dynamic characteristics of li-ion batteries in electric vehicle applications. In *2014 IEEE Conference and Expo Transportation Electrification Asia-Pacific (ITEC Asia-Pacific)*, pages 1–6, Aug 2014.

[17] Peter Keil and Andreas Jossen. Aging of lithium-ion batteries in electric vehicles: Impact of regenerative braking. 05 2015.

[18] *KMZ60 Application Note*.

[19] Gustav Persson Oskar Persson. Torque sensor for automotive application, May 2015. An investigation of torque sensing techniques for drivetrain integration.

[20] Bj¨orn Helander. Integrated torque sensor for e-bike motors, 2016.

[21] *FAG Torque Sensor Inner Bearing*.

[22] *DRV832XX EVM Sensored Software User's Guide*.

[23] F. Caricchi, F. G. Capponi, F. Crescimbini, and L. Solero. Sinusoidal brushless drive with low-cost linear hall effect position sensors. In *2001 IEEE 32nd Annual Power Electronics Specialists Conference (IEEE Cat. No.01CH37230)*, volume 2, pages 799–804 vol.2, June 2001.

[24] H. Kong, J. Liu, and G. Cui. Study on field-weakening theory of brushless dc motor based on phase advance method. In *2010 International Conference on Measuring Technology and Mechatronics Automation*, volume 3, pages 583–586, March 2010.

[25] *The SineWave Grinfineon Motor Controller*.

[26] *The Phaserunner Motor Controller V2*.

[27] *Automotive Stability Enhancement Systems*, nov 2017.

[28] Carmelina Abagnale, Massimo Cardone, Paolo Iodice, S. Strano, M. Terzo, and Giovanni Francesco Vorraro. Derivation and validation of a mathematical model for a novel electric bicycle. In *WCE-2015 2015*, 2015.

[29] H.B. Pacejka. Tire and vehicle dynamics. *Tire and Vehicle Dynamics*, 01 2012.

[30] www.cyclingpowerlab.com. cyclingpowerlab. `https://www.cyclingpowerlab.com/CyclingAerodynamics.aspx`. [parameters related to aerodynamics].

[31] Manabu Kosaka and Hiroshi Uda. Parameters identification for interior permanent magnet synchronous motor driven by sensorless control. *Journal of Low Frequency Noise, Vibration and Active Control*, 28(4):269–283, 2009.

[32] S. De Pinto, C. Chatzikomis, A. Sorniotti, and G. Mantriota. Comparison of traction controllers for electric vehicles with on-board drivetrains. *IEEE Transactions on Vehicular Technology*, 66(8):6715–6727, Aug 2017.

[33] V. Ivanov, D. Savitski, and B. Shyrokau. A survey of traction control and antilock braking systems of full electric vehicles with individually controlled electric motors. *IEEE Transactions on Vehicular Technology*, 64(9):3878–3896, Sep. 2015.

[34] Brian Wiegand. Estimation of the rolling resistance of tires. 04 2016.

[35] Jun yi Cao, Bing gang Cao, and Zhong Liu. Driving resistance estimation based on unknown input observer. 2006.

[36] www.Kreuzotter.de. Bike power calculator. `http://kreuzotter.de/english/espeed.htm`, 2008. [Bike power with rider parameters].

[37] *A Technical Introduction to the TMS320F28004x Microcontroller.*

[38] *BOOSTXL-DRV8320RS EVM User's Guide.*

[39] www.sparkfun.com. 9DoF Sensor Stick Hookup Guide. `https://learn.sparkfun.com/tutorials/9dof-sensor-stick-hookup-guide`, 2008. [AHRS device for e-bike].

[40] *iNEMO inertial module:3D accelerometer, 3D gyroscope, 3D magnetometer.*

[41] G. Dissanayake, S. Sukkarieh, E. Nebot, and H. Durrant-Whyte. The aiding of a low-cost strapdown inertial measurement unit using vehicle model constraints for land vehicle applications. *IEEE Transactions on Robotics and Automation*, 17(5):731–747, Oct 2001.

[42] CHRISTIAN JONSSON. Velocity estimation in land vehicle applications, May 2015. An investigation of torque sensing techniques for drivetrain integration.

[43] R. Mahony, T. Hamel, and J. Pflimlin. Nonlinear complementary filters on the special orthogonal group. *IEEE Transactions on Automatic Control*, 53(5):1203–1218, June 2008.

[44] S Madgwick. An efficient orientation filter for inertial and inertial/magnetic sensor arrays. Technical report, x-io and University of Bristol (UK), 2010.

[45] www.sparkfun.com. OpenLog Hookup Guide. `https://learn.sparkfun.com/tutorials/openlog-hookup-guide`, 2008. [Datalogger for e-bike].

[46] *Sempu Sensor Manual 2018.pdf*.

[47] www.bafang e.com. FM G320.250. `https://www.bafang-e.com/oem-area/components/component/motor/fm-g320250v/`. [bafang FM 320.250V].

[48] www.bafang e.com. RM G020.250.DC. `https://www.bafang-e.com/oem-area/components/component/motor/rm-g020250dc/`. [bafang RM G020.250.DC].